THESIS FOR THE DEGREE OF DOCTOR OF PHILOSOPHY

UV-C Photonic-Crystal Surface-Emitting Lasers

Doğukan Apaydın



CHALMERS

Photonics Laboratory
Department of Microtechnology and Nanoscience (MC2)
Chalmers University of Technology
Göteborg, Sweden, 2026

UV-C Photonic-Crystal Surface-Emitting Lasers
Doğukan Apaydın

©Doğukan Apaydın, 2026

ISBN 978-91-8103-483-7
Doktorsavhandlingar vid Chalmers tekniska högskola
Ny serie nr 5940
ISSN 0346-718X

Photonics Laboratory
Department of Microtechnology and Nanoscience (MC2)
Chalmers University of Technology
SE–412 96 Göteborg
Sweden
Telephone: +46 (0)31–772 10 00

Printed in Sweden by
Reproservice
Chalmers Tekniska Högskola
Göteborg, Sweden, 2026

UV-C Photonic-Crystal Surface-Emitting Lasers

Doğukan Apaydın
Photonics Laboratory
Department of Microtechnology and Nanoscience (MC2)
Chalmers University of Technology

Abstract

Semiconductor lasers are compact, coherent light sources that have enabled or transformed a wide range of applications since their invention in the 1960s. They have rapidly matured at visible and infrared wavelengths; however, their progress at ultraviolet-C (UV-C, λ_0<280 nm) wavelengths has been considerably slower. To date, continuous-wave electrically driven UV-C edge-emitting lasers have been reported, but vertical-cavity surface-emitting lasers have only been demonstrated under optical pumping. Photonic-crystal surface-emitting lasers (PCSELs), on the other hand, are a new type of semiconductor laser and have recently attracted attention for their unique optical properties. They combine watt-level single-mode output powers and circularly symmetric beams with low divergence angles below 1°. PCSELs have demonstrated strong performance at visible and infrared wavelengths, but were not realized in the UV-C before this work.

In this thesis, we demonstrate the first UV-C PCSELs operating at room temperature under pulsed optical pumping. We investigate the influence of photonic crystal design parameters, including hole filling factor, lattice constant, etch depth, and lateral photonic crystal size, on lasing characteristics and address the challenges in achieving lasing under electrical injection. Our results indicate that the lasing threshold of PCSELs decreases with increasing device size. Therefore, a larger size is beneficial for low-threshold operation. However, for large sizes (>100 μm), current injection across the device area is challenging due to the poor electrical conductivity of Al-rich AlGaN, which may prevent lasing. To reduce the current spreading distance and improve current uniformity, we introduce a ring-shaped photonic crystal design, where a central circular region is etched to accommodate an additional n-contact. These findings help better understand III-nitride-based UV-C PCSELs and open a pathway toward future electrically driven devices.

Keywords: PCSEL, photonic crystal, AlGaN, III-nitride, UV-C, deep-UV, zero group velocity

Publications

This thesis is based on the work contained in the following papers:

[A] **D. Apaydın**, H. Andersson, L. Uhlig, S. Graupeter, J. Ciers, G. Cardinali, E. Strandberg, T. Wernicke, M. Kneissl, U. T. Schwarz, P. Tassin and Å. Haglund, "Deep-UV photonic crystal surface-emitting lasers", *Laser & Photonics Reviews*, vol. 20, no. 6, p. e00271, 2026.

[B] **D. Apaydın**, L. Persson, M. Riedel, S. Graupeter, J. Ciers, T. Wernicke, M. Kneissl, U. T. Schwarz and Å. Haglund, "Influence of photonic crystal size and lattice constant on the lasing performance of UV-C PCSELs", , *ACS Photonics*, accepted for publication, 2026.

[C] **D. Apaydın**, L. Persson, M. Riedel, S. Graupeter, J. Ciers, T. Wernicke, M. Kneissl, U. T. Schwarz and Å. Haglund, "Ring-shaped UV-C photonic-crystal surface-emitting lasers", submitted.

Related publications, not included in the thesis:

[D] **D. Apaydın**, "Propelling the PCSEL into the deep-UV", *Compound Semiconductor Magazine*, vol. 32, no. 5, 2026.

[E] M. Riedel, L. Persson, **D. Apaydın**, Å, Haglund, U. T. Schwarz, "Modeling photonic-crystal surface-emitting lasers with guided mode expansion: finite-size effects and higher order modes", *Optics Express*, accepted, 2026.

Related conference contributions, not included in the thesis:

[F] **D. Apaydın**, J. Ciers, H. Andersson, S. Graupeter, G. Cardinali, T. Wernicke, M. Kneissl, P. Tassin and Å. Haglund "Optically

pumped UVC photonic crystal surface-emitting laser", *International Workshop on Ultraviolet Materials and Devices (IWUMD)*, Metz, France, ID We-B4.3, 2023.

[G] **D. Apaydın**, L. Uhlig, J. Ciers, H. Andersson, S. Graupeter, G. Cardinali, T. Wernicke, M. Kneissl, P. Tassin, U. T. Schwarz, and Å. Haglund "UVC photonic crystal surface-emitting lasers with low-divergent far-fields", *International Conference on Nitride Semiconductors (ICNS)*, Fukuoka, Japan, ID OD5-5, 2023.

[H] **D. Apaydın**, L. Uhlig, J. Ciers, H. Andersson, S. Graupeter, G. Cardinali, T. Wernicke, M. Kneissl, P. Tassin, U. T. Schwarz, and Å. Haglund "Photonic crystal surface-emitting lasers with deep-ultraviolet emission", *SPIE Photonics West*, San Francisco, USA, 2024.

[I] **D. Apaydın**, H. Andersson, L. Uhlig, J. Ciers, S. Graupeter, G. Cardinali, T. Wernicke, M. Kneissl, P. Tassin, U. T. Schwarz, and Å. Haglund "III-nitride-based photonic crystal surface-emitting lasers with UVC emission", *Compound Semiconductor Week (CSW)*, Lund, Sweden, 2024.

[J] **D. Apaydın**, L. Uhlig, H. Andersson, S. Graupeter, L. Persson, J. Ciers, G. Cardinali, T. Wernicke, M. Kneissl, P. Tassin, U. T. Schwarz, and Å. Haglund "Impact of photonic crystal size and lattice period on the performance of UVC photonic crystal surface-emitting lasers", *International Workshop on Nitride Semiconductors (IWN)*, Honolulu, USA, 2024.

[K] **D. Apaydın**, L. Persson, M. Riedel, S. Graupeter, L. Uhlig, J. Ciers, T. Wernicke, M. Kneissl, U. T. Schwarz, and Å. Haglund "Understanding losses and mode selection in finite-sized ultraviolet-C photonic-crystal surface-emitting lasers", *International Conference on Nitride Semiconductors (ICNS)*, Malmö, Sweden, ID OD-Mon-6, 2025.

[L] **D. Apaydın**, L. Persson, M. Riedel, S. Graupeter, L. Uhlig, J. Ciers, T. Wernicke, M. Kneissl, U. T. Schwarz, and Å. Haglund "How to design ultraviolet-C photonic crystal surface-emitting lasers for single-mode emission, low threshold and narrow far-field", *International Workshop on Ultra-Wide Bandgap Materials and Devices (IWUMD)*, Wrocław, Poland, ID Tu2-1-4, 2025.

[M] **D. Apaydın**, L. Persson, M. Riedel, S. Graupeter, L. Uhlig, J. Ciers, T. Wernicke, M. Kneissl, U. T. Schwarz, and Å. Haglund "How to obtain low thresholds and high-quality far-fields in optically pumped deep-UV PCSELs", *International Workshop on PCSELs*, Glasgow, Scotland, poster, 2025.

Contents

Abstract **iii**

Publications **v**

Acknowledgement **xi**

Acronyms **xiii**

1 Introduction **1**
1.1 Ultraviolet Light 1
1.2 Ultraviolet Light Sources 3
1.3 Outline 7

2 General Properties of III-nitride Materials **9**
2.1 Crystal structure 9
2.2 Optical properties 11
2.3 Electrical properties and doping 15

3 Photonic-Crystal Surface-Emitting Lasers **19**
3.1 PCSEL History 19
3.2 PCSEL Fundamentals 21
3.2.1 Vertical mode profile 21
3.2.2 Photonic crystals and photonic band structure . . 24
3.2.3 Coupling mechanisms 28

4 Optically Pumped UV-C Photonic-Crystal Surface-Emitting Lasers **33**
4.1 Regrowth-free Approach 33
4.1.1 Fabrication 34
4.1.2 Optical confinement 35

4.2 Optically Pumped UV-C PCSEL Characterization 36
4.3 Proof of Lasing 39
4.3.1 Input vs. output intensity 39
4.3.2 Photonic band structure and spectrum 40
4.3.3 Near-field and far-field emission patterns 43
4.4 Influence of Photonic Crystal Design Parameters 45
4.4.1 Effect of etch depth and lattice constant 46
4.4.2 Effect of filling factor 48

5 Towards Electrically-Driven UV-C Photonic-Crystal Surface-Emitting Lasers 53
5.1 Challenges for Electrically Driven UV-C PCSELs 53
5.2 Etch-Induced Damage to p-Side Conductivity 55
5.2.1 Device structure and fabrication 56
5.2.2 Characterization 58
5.3 Lateral Current Spreading on n-Side 61
5.3.1 Ring-shaped geometry to reduce current spreading distance 61
5.3.2 Device structure and fabrication 62
5.3.3 Characterization 63

6 Summary and Outlook 65

7 Summary of Papers 67

Included papers A–C 93

Acknowledgement

I would like to express my deepest gratitude to my supervisor, Prof. Åsa Haglund. Her guidance and support have helped me throughout my PhD. I have learned a lot from her, not only scientifically as a researcher but also as a person. I am grateful to my co-supervisor, Dr. Joachim Ciers, for his support and precise, to-the-point feedback, which has had a significant effect on my work. I would also like to thank my examiner, Prof. Victor Torres Company, for following my progress during my PhD.

My warmest thanks go to Prof. Ulrich Theodor Schwarz for sharing his knowledge and for his kindness. I am also thankful to Prof. Michael Kneissl and Dr. Tim Wernicke for their collaboration and their detailed comments and feedback on my work.

I would like to thank Estrella, who shared her experience and helped me get through many challenges in the cleanroom, and Lars, from whom I learned a lot. My knowledge of PCSELs would not be at this level without him. Many thanks go to my office mates Andreas, Phuc and Lou for making the office environment so nice and for the conversations that made the days more fun. I thank Cesur; I really enjoyed our talks in Turkish. I also thank Erik, Sharma, Cleophace, Artem, Mikolaj and Ryan for creating a friendly and supportive environment in the group. And I thank Katya for our nice conversations.

My special thanks go to Sarina for growing the epitaxial material I used. Much of this thesis is literally built on her hard work. I also thank Giulia, I really enjoyed talking with her while she was with us. I would like to thank Lukas for his contributions during his visit. His time with us was short, but the influence was much bigger. I would also like to thank Prof. Philippe Tassin and Hjalmar Andersson for discussions on PCSELs.

I thank Prof. Peter Andrekson and Prof. Magnus Karlsson for making the lab a great place to work. I would also like to thank Gunnel for her administrative support, and all current and former members of the

Photonics Laboratory for contributing to the lab environment and helping build a strong lab culture. My appreciation extends to the cleanroom staff for their efforts in keeping the cleanroom running smoothly.

Finally, I am deeply grateful to my father, Süreyya Apaydın and my mother, Gülay Apaydın, for everything they have done for me, for their unconditional love and continuous support.

No words are enough to express my gratitude to my wife, Funda. Her support and presence helped me overcome every challenge I faced. Knowing she was with me made this journey possible.

And to my son, Metehan, who has brought light and meaning to my life, and to my daughter, Doğa, who is not yet here with us but already makes me happy when I imagine our growing family, thank you.

Doğukan Apaydın
Göteborg, Sweden
September 2026

Acronyms

1D	one-dimensional
2D	two-dimensional
AFM	atomic force microscope
DBR	distributed Bragg reflector
CW	continuous wave
DFB	distributed-feedback
DGA	double-growth-annealing
DPD	distributed polarization doping
EEL	edge-emitting laser
EQE	external quantum efficiency
FF	filling factor
FWHM	full width at half maximum
HSQ	hydrogen silsesquioxane
LED	light-emitting diode
PC	photonic crystal
PCSEL	photonic-crystal surface-emitting laser
PWE	plane-wave expansion
QCSE	quantum-confined Stark effect
QW	quantum well
SEM	scanning electron microscope
TE	transverse electric
TM	transverse magnetic
UV	ultraviolet
UVA	ultraviolet-A
UVB	ultraviolet-B
UVC	ultraviolet-C
VCSEL	vertical-cavity surface-emitting laser

Chapter 1

Introduction

1.1 Ultraviolet Light

Light is much more than what our eyes can see. Although our perception is limited to visible light, we experience other wavelengths in our daily lives as well. The electromagnetic spectrum spans wavelengths from gamma rays with extremely short wavelengths to radio waves with wavelengths extending to kilometers and beyond (Figure 1.1). Ultraviolet (UV) wavelengths lie just beyond the visible region and carry higher energy than visible light. They range from 100 nm to 400 nm and are usually divided into three regions: UV-A (320–400 nm), UV-B (280–320 nm), and UV-C (100–280 nm), with the 100–200 nm region generally called the vacuum UV.

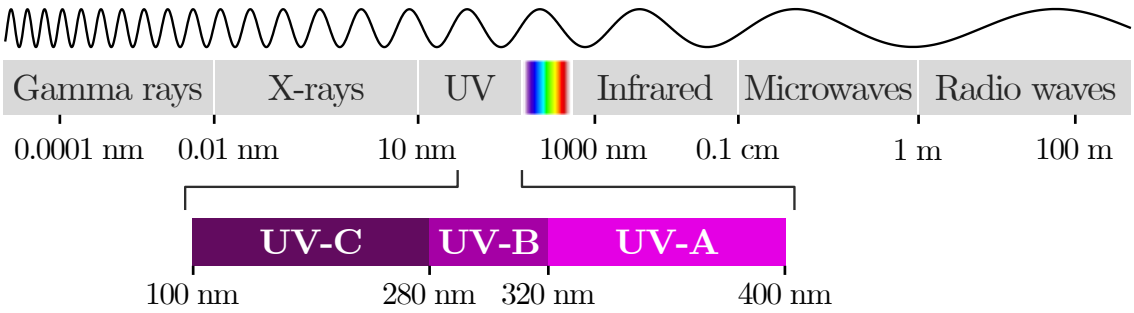


Figure 1.1: The electromagnetic spectrum from gamma rays to radio waves with a zoomed-in view of the UV region (100–400 nm) showing UV-A (320–400 nm), UV-B (280–320 nm) and UV-C (100–280 nm).

For many people, UV light is a term they first hear in warnings about dangerous solar radiation and in the efforts they make to protect themselves from its effects. The Sun emits radiation across all three regions [1]. Most of the UV-A radiation passes through the atmosphere, whereas a substantial portion of the UV-B is filtered out and all the UV-C is absorbed by the ozone layer. We use sunscreens, UV-filtering coatings and protective eyewear, and all this effort is to further reduce the relatively small portion of UV radiation that reaches the Earth's surface. This is because the energy of UV light is high enough to damage cellular DNA and can be harmful to humans [2]. On the other hand, the same high energy (around 265 nm and below) is also very effective at killing viruses and bacteria [3]. UV light also has uses in many modern technologies, including lithography and polymer curing, as well as medical skin treatment and gas sensing (Figure 1.2).

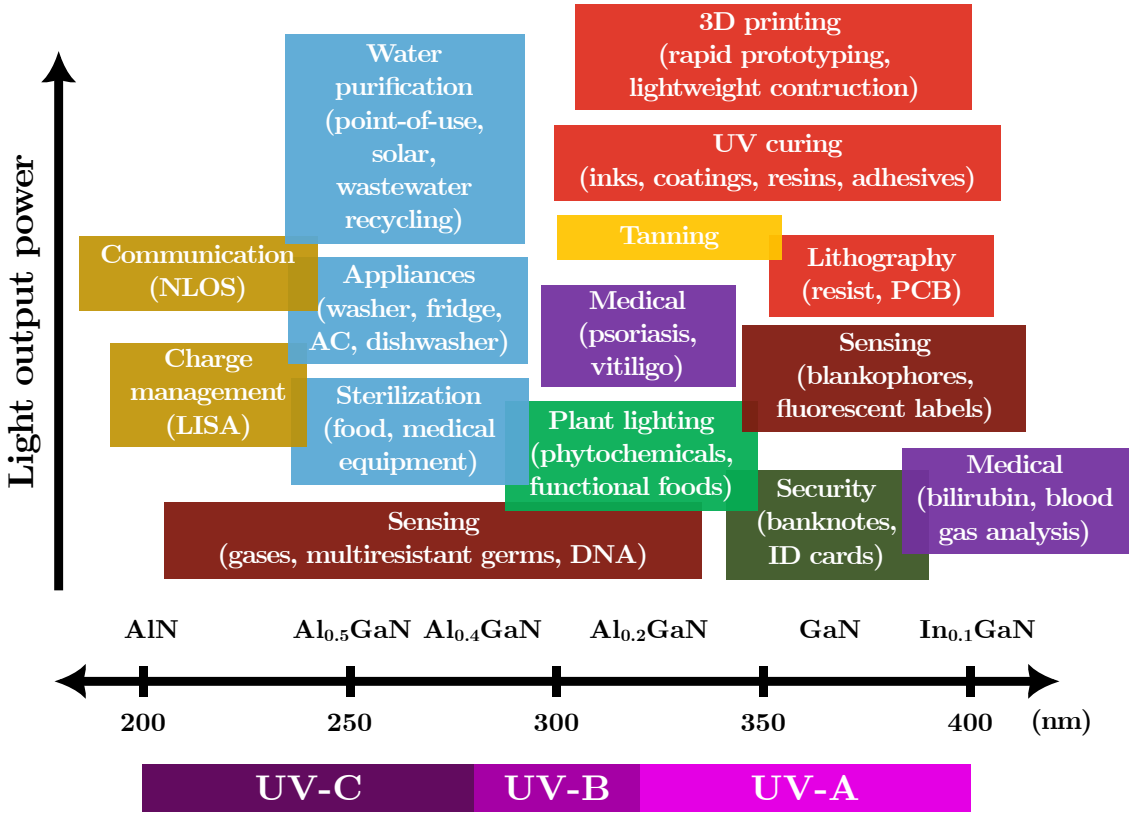


Figure 1.2: Overview of common UV applications with required wavelength ranges and relative powers [4].

1.2 Ultraviolet Light Sources

For a long time, mercury lamps were the primary light source in many UV applications, especially for killing germs [5]. They were cheap and reliable, and no other UV light source could compete with them. However, they pose environmental and health risks due to the mercury they contain, which is a toxic heavy metal [6]. This concern motivated researchers to develop a mercury-free UV light source that could replace them.

In recent years, III-nitride-based UV light-emitting diodes (LEDs) have emerged as a more compact, efficient and safer alternative to traditional mercury lamps [7]. They consist of alloys of Al, Ga, In and N, and in the early stages of development of III-nitrides, achieving sufficient p-type conductivity was a major challenge and remained so for a long time [8]. It was finally solved by Japanese scientists in the late 1980s [9], which eventually led to blue LEDs [10]. This breakthrough was awarded a Nobel Prize in Physics in 2014. Since then, researchers have pushed the emission wavelength toward shorter wavelengths by increasing the Al concentration and have successfully demonstrated UV devices [11,12], despite much lower p- and n-type conductivities [13] and external quantum efficiencies (EQE) [14, 15]. The emission wavelengths of UV LEDs have currently reached down to 210 nm [16], which is the direct band-to-band transition in AlN.

UV LEDs have offered a potential solution for applications that do not require high power, a highly focused beam or a narrow linewidth [17]. Some applications, however, such as photolithography [18, 19], surgical procedures [20], or micro-machining [21, 22], require lasers to achieve high resolution and precision. The situation for UV lasers is similar to UV LEDs. The UV laser market has long been dominated by a limited number of sources such as frequency-converted diode-pumped solid-state lasers and excimer lasers. Depending on the application and the target wavelength, different gain materials are used for these lasers (Figure 1.3). However, these lasers are expensive, bulky and exhibit low wall-plug efficiency. Therefore, they are not an optimal solution to an application that would benefit from a compact UV laser. III-nitride-based semiconductor lasers offer a promising alternative.

Although UV semiconductor lasers have not yet matured enough to replace conventional lasers, they are following a similar development path to that of UV LEDs. GaN-based edge-emitting lasers (EELs) at UV-A wavelengths above 370 nm progressed relatively quickly compared to UV-

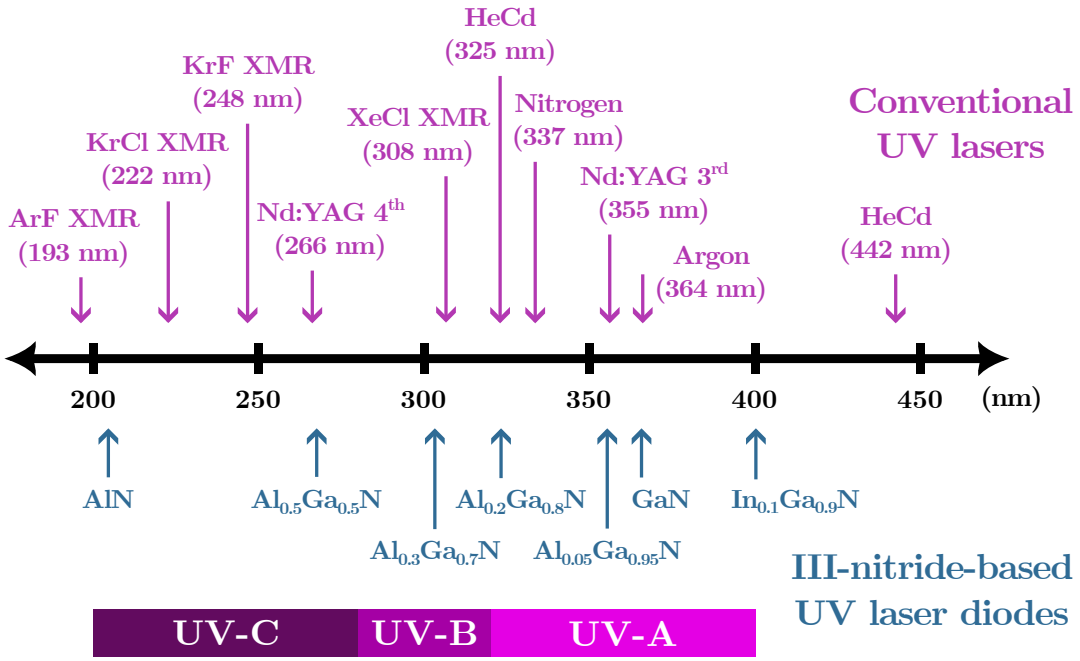


Figure 1.3: Different types of conventional excimer and frequency-converted solid-state lasers used at UV wavelengths along with the III-nitride composition required for the same target wavelength for semiconductor lasers [23].

B and UV-C, and have now reached watt-class output powers [24, 25]. The main reasons are high conductivity, lower dislocation density, lower optical losses and higher EQE compared to UV-B and UV-C laser diodes [26]. GaN-based EELs are readily available on the market [27].

In the UV-B region, after demonstrating lasing under pulsed current injection in 2020 [28], Meijo University has achieved another milestone by demonstrating lasing under continuous-wave (CW) operation at room temperature [29]. Recently, another group from Michigan University has demonstrated pulsed UV-B lasing from an EEL grown by molecular beam epitaxy [30]. These represent a significant progress in UV lasers, given that the EQE in the UV-B is lower than in UV-A and UV-C [15].

In the UV-C region, Nagoya University demonstrated the first electrically driven semiconductor-based EEL in 2019 [31]. This device was grown on bulk single-crystal AlN and operated at room temperature under pulsed current injection. Using an AlN substrate, which provides a lower dislocation density for Al-rich compositions compared to foreign substrates, such as sapphire [32], reduced threading dislocation density and enabled lasing. Another important approach that enabled UV-C lasing was the use of a distributed polarization-doped (DPD) p-side, where

the material composition gradually changes across the layer, leading to a polarization field that generates free carriers [33], instead of an impurity-doped layer with Mg. Although Mg doping is effective in GaN, it yields much lower conductivity in Al-rich III-nitrides due to the high ionization energy at room temperature [34,35]. After the initial pulsed demonstration, Nagoya University achieved CW lasing at 5°C with heat sinking by optimizing the epitaxial growth conditions to reduce point defects, which are known to cause non-radiative recombination, and by adjusting the layer thicknesses and compositions to increase the quantum well confinement factor [36]. Later, they demonstrated CW lasing at room temperature by reducing the stress and dislocation formation caused by steep mesa sidewalls through a slanted mesa profile and placing the contacts close to the mesa to decrease lateral series resistance [37]. Building on these, ULTEC inc, a Japanese startup founded by the same group, has announced the first commercially available UV-C laser diodes [38].

In the case of vertical-cavity surface-emitting lasers (VCSELs), lasing has been demonstrated in UV-A under CW current injection at room temperature [39] but demonstrations in UV-B and UV-C so far have been limited to pulsed optical pumping [40–42]. We have seen electrical injection only in UV-A and UV-B resonant-cavity LEDs [43,44], which can be considered an intermediate step between LEDs and VCSELs. One of the biggest challenges in UV VCSELs is achieving high-reflectivity mirrors (>99%) in the III-nitride material system while at the same time having good electrical conductivity and transverse electrical confinement with low optical losses. Current solutions for the mirrors are epitaxially grown distributed Bragg reflectors (DBRs) [45, 46], porous DBRs [47, 48] and dielectric DBRs [49,50]. Alternatively, hybrid devices, which incorporate two types of DBRs, generally a dielectric DBR combined with a porous or an epitaxial DBR, have also been implemented [51, 52]. In epitaxially grown DBRs, a large number of pairs is needed to achieve a high reflectivity due to the low refractive index contrast. This low contrast also narrows the stopband, making it difficult to align the peak wavelength of the reflectivity spectrum with the resonance wavelength. Some groups have addressed this issue by performing in-situ reflectance measurements during DBR growth to control the position of the stopband [53]. On the other hand, porous DBRs have a higher refractive index contrast, but they are more difficult to fabricate and controlling the uniformity of the porosity is challenging [54]. Optical performance may also be affected by scattering [55]. Dielectric DBRs are promising due to their high refrac-

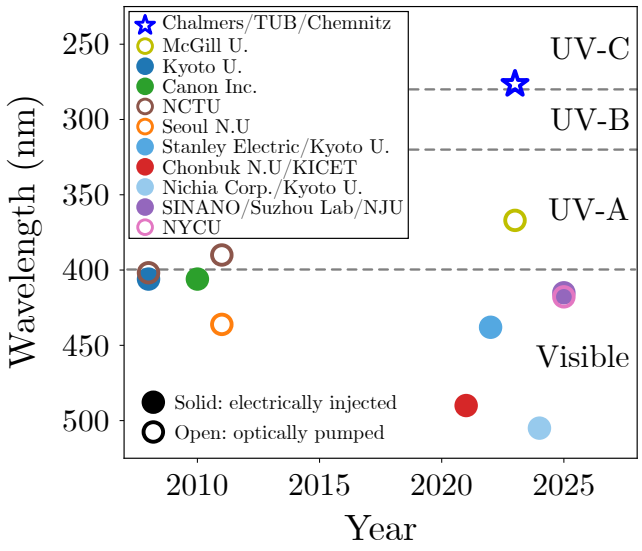


Figure 1.4: Emission wavelengths of III-nitride-based PCSELs reported by different groups [63–73]. To avoid crowding, only the earliest demonstration for each group or collaboration is displayed when multiple similar reports are available. The shape indicates reporting group (circles: other groups, stars: our group); the marker fill indicates the pumping method (solid: electrical injection, open: optical pumping).

tive index contrast. However, substrate removal is necessary to access both sides and deposit the layers. Additionally, the presence of dielectric materials on both sides complicates current injection, especially for Al-rich AlGaN devices, and the low thermal conductivity of these materials can pose problems for heat management [56, 57].

As these UV laser technologies continue to advance, another type of semiconductor laser, the photonic-crystal surface-emitting laser (PCSEL), is attracting attention [58–61]. PCSELs are a relatively new type of semiconductor laser that can deliver higher powers while maintaining single-mode operation and a circularly symmetric beam with a low divergence angle ($<1°$) [62]. PCSELs emit from the surface, like VCSELs, but their epitaxial stack is analogous to that of a conventional distributed-feedback (DFB) laser. A simple stack comprises a planar waveguide and a layer with an alternating refractive index that perturbs the guided mode. DFB lasers have a one-dimensional (1D) grating for in-plane feedback, whereas PCSELs have a two-dimensional (2D) photonic crystal for both in-plane feedback and vertical outcoupling.

The PCSEL concept has been applied to different material systems and has enabled lasing in multiple wavelength ranges, including visi-

ble [69, 71, 73–76] and infrared [77–83]. To date, only a limited number of reports have demonstrated III-nitride devices using 2D photonic crystals for lasing, with a few at UV wavelengths and the majority at blue wavelengths (Figure 1.4). Demonstrations at UV wavelengths are comparatively rare, mostly due to inherent limitations of Al-rich III-nitride materials such as low electrical conductivity, low material gain and low refractive index. On top of that, the photonic crystal feature size scales with the operating wavelength, requiring smaller features for shorter wavelengths. This makes the fabrication more challenging and the device more sensitive to fabrication imperfections. Before this thesis work, one report has shown lasing at 367 nm by using a nanowire-based 2D photonic crystal [84]. Recently, our group at Chalmers University of Technology demonstrated the first UV-C PCSELs with low-divergence far fields and 2D lasing under optical pumping at room temperature [Paper A].

1.3 Outline

This thesis aims to provide a general overview of PCSELs, detail the first demonstrations in the UV-C regime, and discuss the challenges in future electrically driven PCSELs. **Chapter 2** covers a brief introduction to the III-nitride material system. **Chapter 3** provides a general introduction to PCSELs and explains their operating principles. **Chapter 4** introduces the first optically pumped UV-C PCSEL demonstrations using hexagonal and square lattices of circular holes. **Chapter 5** addresses the challenges in electrically driven devices, focusing on the regrowth-free fabrication method used in our optically pumped devices and introduces a novel device concept based on a ring-shaped photonic crystal, which has the potential to reduce current spreading length and improve current uniformity. Finally, **Chapter 6** summarizes the thesis and outlines the future trajectory of UV-C PCSEL development using the regrowth-free method.

Chapter 2

General Properties of III-nitride Materials

2.1 Crystal structure

III-nitride materials are binary compounds formed by group-III elements (Al, Ga, In) with the group-V element nitrogen (N), and their ternary and quaternary alloys [13]. These materials exhibit three crystalline forms: wurtzite, zincblende and rock salt. The rock salt crystal forms only under extreme pressures and is not possible to grow epitaxially. Experimental transition pressures into the rock salt phase are on the order of several tens of gigapascals [85–87]. The zincblende form is metastable under normal pressure and temperature but can be stabilized by epitaxial growth on certain planes of cubic substrates, such as (011) in Si or GaAs. It consists of two interlacing face-centered cubic sublattices, one for the group-III elements and one for the group-V element. Among the three crystal structures, wurtzite is the only thermodynamically stable phase at normal conditions and consists of two interlacing hexagonal close-packed sublattices. Although wurtzite and zincblende appear similar, the stacking of close-packed planes in zincblende has a 60° rotation around the [111] axis relative to the [0001] axis in wurtzite, also known as the c-axis (Figure 2.1). The focus of this thesis is on wurtzite III-nitrides, as they are the most common form.

Wurtzite crystals are defined by three structural parameters: two lattice constants, a (basal plane side length), c (unit cell height) and u, a dimensionless structural parameter that represents the ratio of the bond length in the c-axis to the lattice constant c. Wurtzite III-nitrides lack

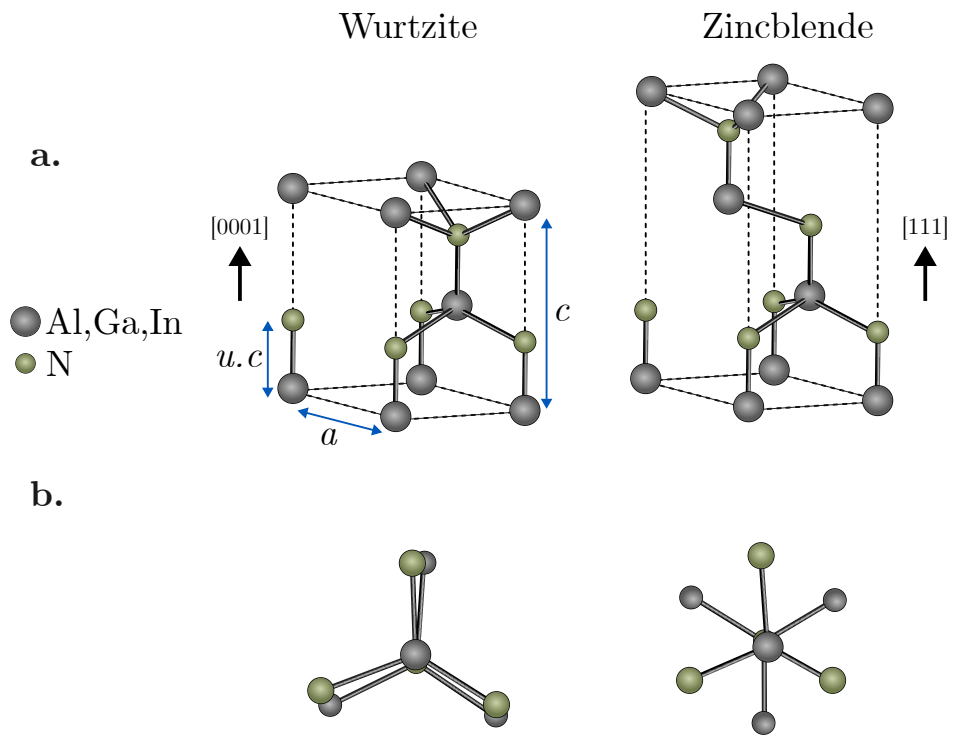


Figure 2.1: **(a)** Schematic showing the atomic sites for wurtzite and zincblende crystals. **(b)** View along the [0001] direction in wurtzite and [111] direction in zincblende.

inversion symmetry, meaning that the [0001] and [000$\bar{1}$] directions are different, leading to a polarity in the crystal (Figure 2.2). The bonding asymmetry in the crystal leads to a built-in spontaneous polarization (P_{sp}) along the c-axis. AlN has the highest spontaneous polarization among the III-nitrides (AlN: -0.081 C/m^2, GaN: -0.029 C/m^2, InN: -0.032 C/m^2) due to its highly ionic Al–N bond, which causes a deviation of the structural parameter u from the ideal wurtzite value [88]. When the crystal is strained, it induces an additional piezoelectric polarization (P_{pz}), and the total polarization is the sum of these two polarization vectors.

The built-in polarization creates an internal electric field and the magnitude of the electric field is different for different crystallographic orientations, which leads to polar, semipolar and nonpolar planes. The plane perpendicular to the c-axis, known as the c-plane (0001), is the primary polar orientation in III-nitrides (Figure 2.3), as the polarization vector is normal to this plane. In contrast, in the m-plane (1$\bar{1}$00) and a-plane (11$\bar{2}$0), the polarization vector lies within the plane and has

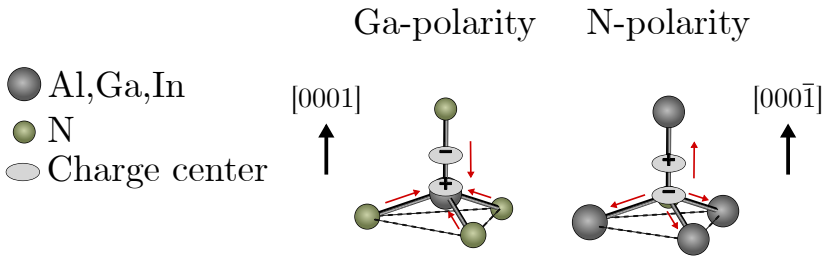


Figure 2.2: Schematic showing the Ga- and N-polar crystals along the [0001] and [000$\bar{1}$] directions. The red arrows indicate the polarization directions.

no component normal to the surface. Therefore, these crystallographic planes are considered nonpolar. In other crystallographic planes, the polarization vector is tilted relative to the c-axis; therefore, it has both in-plane and normal components. These are called semipolar planes.

2.2 Optical properties

III-nitrides are direct band gap materials that have continuously varying band gap energies that range from 0.7 eV for InN to 3.4 eV for GaN and 6.1 eV for AlN at room temperature. With this wide range, they span from UV-C wavelengths (∼210 nm) to infrared (∼1500–1700 nm). The band gap of different compositions of ternary alloys of AlGaN, InGaN and AlInN can be calculated using

$$E_g(x) = x\,E_{g,A} + (1-x)\,E_{g,B} - b\,x(1-x) \tag{2.1}$$

where $E_g(x)$ is the band gap of the corresponding ternary alloy, $E_{g,A}$ and $E_{g,B}$ are the band gaps of the corresponding binaries. b is the bowing

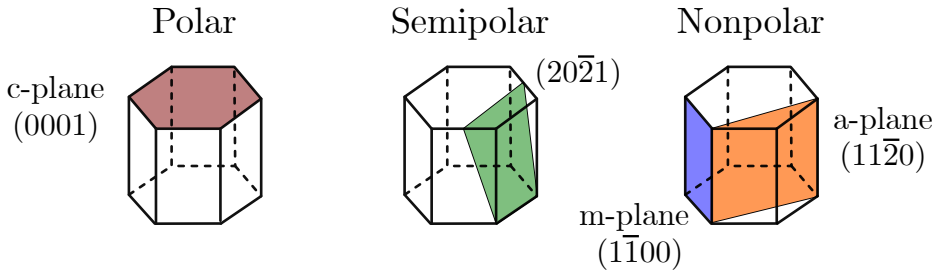


Figure 2.3: Crystallographic planes in wurtzite III-nitrides showing the polar, semipolar and nonpolar orientations.

parameter and is 0.7 eV, 1.4 eV and 2.5 eV for AlGaN, InGaN and AlInN, respectively [89]. Figure 2.4 shows the band gap energies, corresponding emission wavelengths and lattice constants (basal plane side length, a) of wurtzite AlN, GaN, InN and their alloys for different compositions.

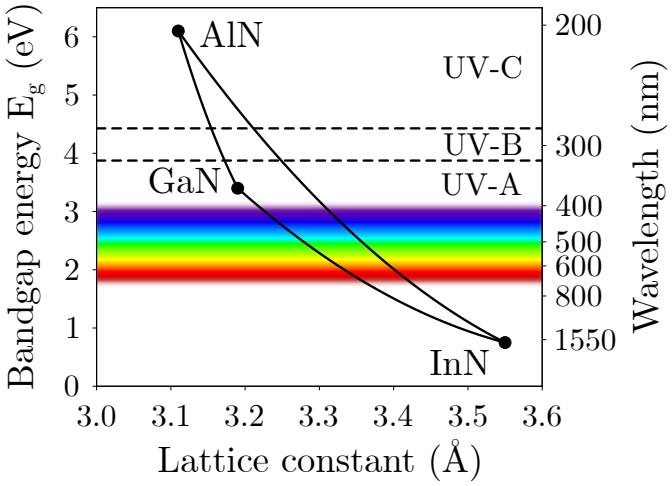


Figure 2.4: Band gap energies, corresponding emission wavelengths and lattice constants (basal plane side length) of wurtzite AlN, GaN, InN and their alloys for different compositions. The data is taken from [89].

The band structure of III-nitrides is influenced by strain, which shifts the bands and changes band gap energies [90]. This is particularly important because III-nitrides are usually grown on foreign substrates, such as sapphire and SiC, introducing strain caused by lattice mismatch. Strain also develops because of lattice mismatch within the epitaxial structure. Additional strain can also be introduced during wafer cooling after growth, due to differences in the thermal expansion coefficients of the substrate and the epitaxial layers [91]. These combined sources of strain modify the band gap; for example, the band gap of GaN grown on sapphire is 17 meV higher than that of free-standing GaN as a result of compressive strain [92]. The band gap, and therefore the emission wavelength, is also affected by temperature, red-shifting with increasing temperature. From 7 K to 295 K, the band gap of AlGaN shifts by approximately 0.065 eV, independent of composition [93]. For higher temperatures up to 800 K, the shift can be as high as 0.35–0.37 eV for different Al compositions [94].

In addition, the hexagonal anisotropy in wurtzite also has an influence on the band structure and causes splitting of the top three valence

bands due to crystal field and spin-orbit coupling [4]: heavy-hole, light-hole, and crystal-field split-off, also referred to as A, B, and C bands, when ordered in energy in GaN (Figure 2.5). In AlN, due to a large negative crystal field, the bands shift and the order becomes crystal-field split-off, heavy-hole and light-hole for A, B, and C, respectively. In GaN, the transition from the conduction band to the A band emits light polarized perpendicular to the c-axis, i.e., in the c-plane, yielding transverse-electric (TE) polarization. In contrast, the transition from the conduction band to the B or C band can emit light with polarizations both perpendicular and parallel to the c-axis, giving rise to both TE and transverse-magnetic (TM) polarized emission. The ratio of TM to TE emission increases with increasing Al composition [95]. In a device grown on the c-plane, extracting TM emission is more difficult because TM waves are trapped in the layers by total internal reflection and propagate laterally, thereby reducing light extraction efficiency. Transitions from the conduction band to the subbands also have different matrix elements [96], resulting in different optical gains for different transitions.

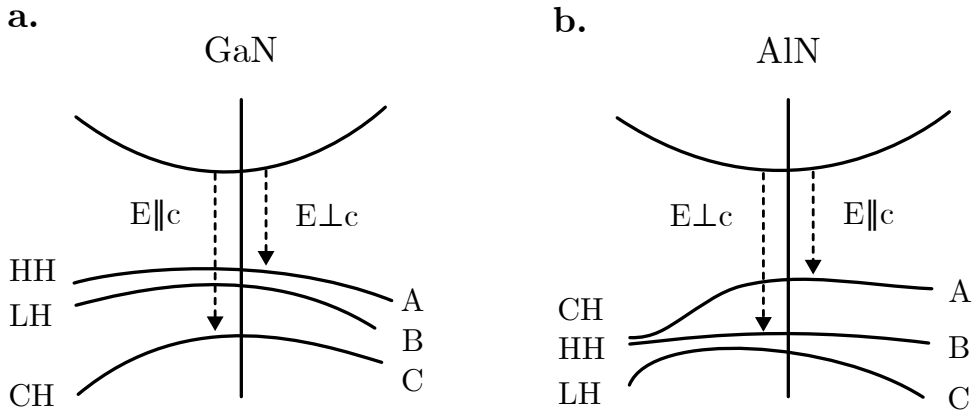


Figure 2.5: Schematic of the valence band splitting in wurtzite **a.** GaN and **b.** AlN.

The curvature of these bands influences the material gain and differential gain in III-nitrides. The bands are relatively flat, for instance, compared to those of GaAs, leading to higher effective electron and hole masses [97]. This, in turn, leads to a higher density of states, which increases the theoretical maximum material gain, but also increases the carrier density required to reach transparency and lowers the differential gain [98]. This limitation is compounded by the polarization field caused by the lack of inversion symmetry. At the device level, the gain is fur-

ther degraded by low dopant activation efficiencies, which lead to reduced carrier injection efficiency and therefore fewer carriers, low electron-hole wavefunction overlap in the quantum wells (QWs) due to the polarization field and poor crystal quality with high defect density. In the c-plane in QWs and heterostructures, the internal electric field induced by spontaneous polarization and/or piezoelectric polarization increases the carrier lifetime, separates the electron and the hole wavefunctions and decreases the band gap energy, causing a redshift in the absorption and emission wavelengths. This is known as the quantum-confined Stark effect (QCSE) [99,100]. The electric field reduces the electron-hole wavefunction overlap, thereby lowering the radiative recombination rate. Figure 2.6 illustrates a GaN quantum well between two AlGaN layers along the c-axis, showing the tilting of the electron and hole energy levels, the decrease in the band gap energy and the wavefunction overlap. At high current or pump power densities, the internal field is reduced and the QCSE is screened; thus, the emission blue-shifts toward the zero-field transition energy [101, 102]. At the operating conditions of semiconductor lasers, typically on the order of kA/cm^2 current densities, the QCSE becomes negligible. Heavy doping levels around 10^{19} cm^{-3} also result in the screening of the effect due to the electric field induced by the free carriers [103].

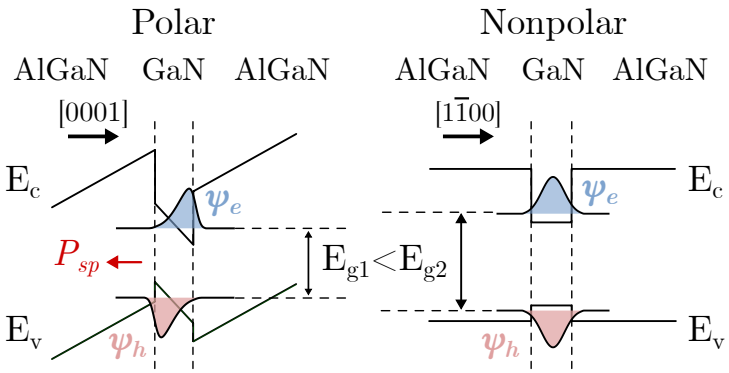


Figure 2.6: Schematic of the energy band diagrams of GaN/AlGaN QWs for polar and nonpolar orientations.

A way to mitigate the effect of the QCSE on the wavefunction overlap is to use thin QWs [104], which are typically less than 3 nm in III-nitride devices. Thick QWs provide higher confinement factors but suffer from low matrix elements [98]. However, recent research shows that thick QWs can also be beneficial for high optical gain and low threshold [105, 106].

In thick QWs, the QCSE is screened by the carriers in the fundamental state, which enhances the wavefunction overlap of the excited states, thus enabling higher optical gains.

The effects of the built-in electric field can also be reduced by growing epitaxial layers on nonpolar or semipolar crystallographic planes [107]. Although this approach increases the optical matrix element, epitaxial growth is complex and crystals grown on nonpolar and semipolar planes often have higher defect densities compared to those grown on the c-plane [108]. In addition, the available substrate sizes for non-polar and semipolar orientations are limited, which substantially increases costs and reduces yield. Due to these practical reasons, as well as the availability of substrates and well-established buffer layers, most III-nitride devices are grown on the c-plane.

2.3 Electrical properties and doping

The electrical properties of III-nitrides make them ideal for applications that require high power and high speeds. This is mostly due to their large band gaps, which yield high breakdown voltages; the relatively high electron mobility of GaN, which enables fast switching and high-frequency operations; and their thermal properties, which allow for stable device performance at high temperatures and power levels. However, the free carrier concentration is generally lower than that of other III-V semiconductors at room temperature, especially for p-type, due to the large band gap and the deep acceptor levels. This makes efficient doping challenging for III-nitrides, particularly for Al-rich compositions [13].

Early GaN crystals had unintentional n-doping that could reach a concentration of 10^{17}–10^{19} cm^{-3}, most likely due to donor impurities such as oxygen and silicon that are incorporated during growth [34, 109]. This issue was later resolved by improving the growth conditions. Now, with intentional Si doping, the most common donor type in GaN, a doping concentration of $\sim 10^{19}$ cm^{-3} can be achieved [110]. At higher Si doping concentrations, the thickness of the layer that can be grown without degrading the quality of the material or introducing a crack is limited because of the strain introduced by heavy Si doping [111].

For p-type doping, the most commonly used acceptor in GaN is Mg. Achieving p-type conductivity requires activation of Mg by breaking the Mg-H bond that is formed during the growth because of the H_2 carrier gas. Excess hydrogen is then removed by a high-temperature annealing

step. A hole concentration of $\sim 10^{18}$ cm^{-3} can be achieved at room temperature in GaN grown by metal-organic chemical vapor deposition [112]. Because the activation energy of Mg in GaN is approximately 150–200 meV, less than 1% of the acceptors are ionized at room temperature. This low activation efficiency issue becomes more pronounced for AlGaN alloys, especially with high Al compositions. The activation energy increases with increasing Al composition, reaching about 500–600 meV for AlN. Since the acceptor energy level is so deep, only an extremely low fraction (10^{-9}) of acceptors are ionized at room temperature [113]. The resistivity of p-doped AlN is on the order of mega-ohms, which is essentially insulating. Although the ionized carrier concentration is higher in Al-rich AlGaN alloys compared to AlN, it is still very low. To increase the hole concentration, researchers have recently adopted DPD to eliminate the limitations of impurity doping [31]. With a 50-nm-thick distributed-polarization-doped layer of $Al_xGa_{1-x}N$ with a graded Al composition from x = 1.00 to x = 0.70, a free carrier concentration larger than 10^{18} cm^{-3} can be achieved [114]. This approach has significantly improved the p-type conductivity in devices based on Al-rich AlGaN alloys and enabled lasing at UV-C wavelengths [31].

When it comes to n-doping of Al-rich AlGaN alloys, although it is relatively easier for low Al compositions, it becomes more difficult for Al compositions higher than ∼80% [115]. For AlGaN alloys up to 80% Al composition, Si is a shallow donor with an activation energy of ∼15 meV [34], which increases rapidly for higher compositions and becomes a deep-level donor. For MOCVD-grown AlGaN, the electron concentration can exceed 10^{19} cm^{-3} [116]. The main limiting factor for this Al-composition range is the self-compensating defect formed by group-III-vacancy complexes with Si, which reduces net donor concentration. For higher Al contents, the electrical properties degrade (i.e, lower electron concentration, lower mobility, lower conductivity) due to the increasing donor activation energy, degradation in material quality, DX center formation that acts as a compensation center and self-compensating effects.

On the InN side, the low growth temperature and the large lattice mismatch with available substrates make it difficult to obtain high-quality single-crystal material. To date, reported InN materials often show very high unintentional n-doping that can reach 10^{21} cm^{-3} [117]. This is mainly because in InN the Fermi stabilization energy (E_{FS}) lies above the conductive band edge and when the Fermi level is below the Fermi

stabilization energy ($E_F < E_{FS}$), donor-like native defects form [118]. As these defects form, the Fermi level moves toward the Fermi stabilization level, which leads to very high unintentional n-type carrier concentrations and limits the maximum intentional doping levels that can be achieved. Pinning the Fermi level in the conduction band also prevents achieving p-type conductivity. Although some reports claim p-type doping [119], reproducible and reliable p-doped InN planar films still remain challenging.

Chapter 3

Photonic-Crystal Surface-Emitting Lasers

3.1 PCSEL History

PCSELs combine the unique properties of other types of semiconductor lasers, such as the large gain area of EELs and the circularly symmetric beam profile of VCSELs. A comparative overview of these lasers is shown in Figure 3.1. The PCSEL concept was first introduced by two different groups in 1999 [120, 121]. Meier et al. used an organic gain medium and achieved lasing using a 2D photonic crystal. However, their device operated at the X-point in the band structure, where coupling occurs only in 1D and therefore a 2D standing field cannot form. Imada et al. used an InP-based device and designed the photonic crystal to operate at the Γ-point, allowing a 2D standing field and emission from the surface. Their early device relied on wafer fusion to encapsulate the photonic crystal. This approach was later replaced by epitaxial overgrowth techniques, which enabled the first blue PCSEL in the GaN material system [64]. The first blue PCSEL had a hexagonal lattice with circular holes and a threshold current density of about 67 kA/cm^2. The high threshold current density was attributed to the low photonic-crystal confinement factor and the losses associated with the SiO_2 in the holes. Later, employing a square lattice with asymmetric holes enabled watt-level output powers in the GaAs material system [122]. Adjusting the degree of the asymmetry of the holes allows controlling the radiative losses [123]. The square lattice provides greater flexibility for breaking symmetry and tailoring outcoupling, whereas the high degree of sym-

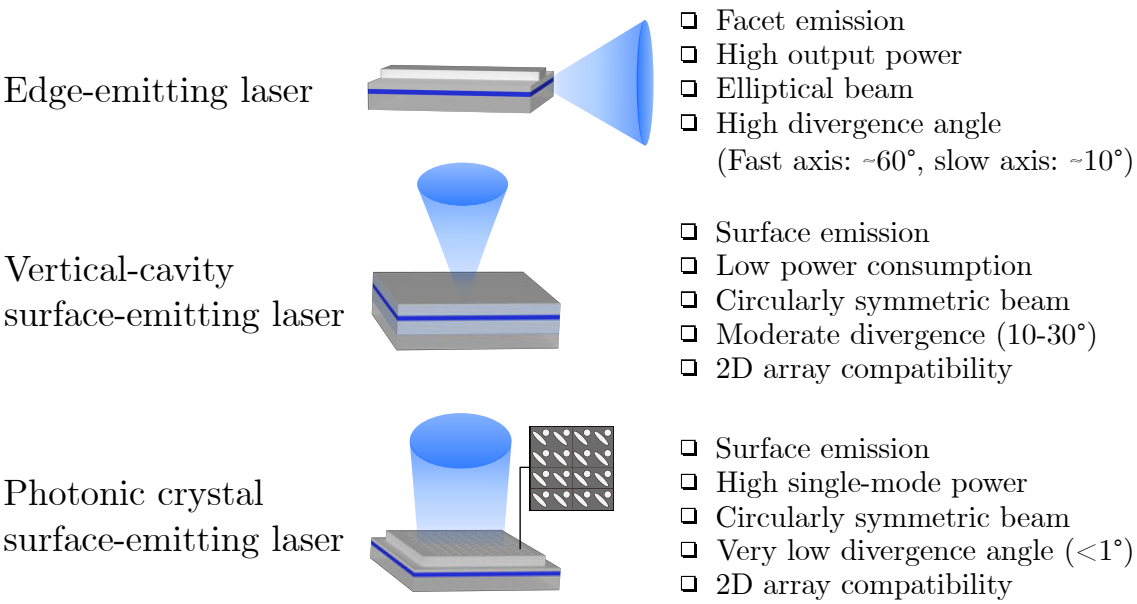


Figure 3.1: Comparison of EELs, VCSELs and PCSELs.

metry of the hexagonal lattice limits control over outcoupling [69]. In addition to these two conventional lattices, other lattice types and hole geometries have been utilized to control radiation losses and engineer the optical modes [72, 124–127]. Examples of different lattices are shown in Figure 3.2. To scale up the device area while maintaining single-mode lasing, Noda's group at Kyoto University adopted the double-lattice approach, in which higher-order modes experience destructive interference and are therefore canceled [128]. The addition of the second lattice enhances the modal discrimination and enables single-mode operation at larger sizes, leading to higher output powers. Benefiting from this, the double-lattice design has led to watt-level output power in the GaN material system at blue wavelengths [69]. With the optimized regrowth condition and waveguide design, the threshold current density was reduced to $\sim$3 kA/cm^2. Another approach to increase the device size without introducing higher-order modes is to use open-Dirac cavities, where the fundamental mode exhibits a flat field profile across the photonic crystal that suppresses spatial hole burning [129].

Without increasing the size of an individual PCSEL, it is also possible to increase the output power of PCSELs by coupling them together in a 2D array [130, 131]. Such a configuration allows the devices to benefit from the lateral losses of the neighboring devices and to increase power

more efficiently [132]. More recently, output powers have been further increased with PCSELs achieving 1.8 kW under pulsed operation by employing multiple active layers through a tunnel junction [133]. Besides scaling for higher power, more sophisticated functionality has also been explored, such as beam steering and tailored beam patterns [134–136]. This is achieved by shifting the positions of individual holes, thereby modulating the phase. In addition, PCSELs are capable of delivering a very narrow spectral linewidth due to their large area [59], with recent work reporting values as low as 1 kHz at watt-level output powers [137].

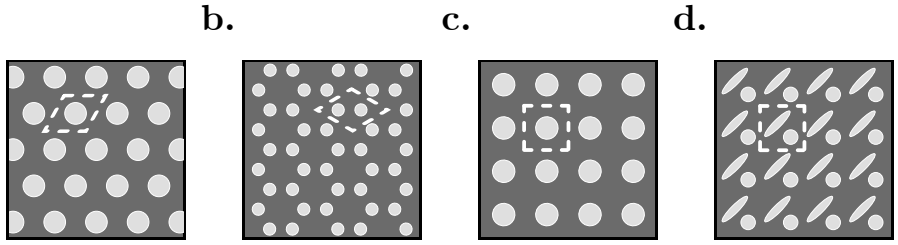


Figure 3.2: Different lattice types used in PCSELs: **a.** hexagonal, **b.**. honeycomb, **c.**, square and **d.** double-square lattice. The areas indicated by a white dashed line show the unit cell.

In PCSELs, the photonic crystal diffracts light equally in both the upward and downward directions. Therefore, in an ideal device, the wall-plug efficiency is limited to 50% if one emission direction is lost. To overcome this and increase efficiency, a DBR has been incorporated to redirect one of the emission directions [138]. In addition, PCSELs usually have a non-uniform current distribution, which results in a temperature gradient across the device. This causes a change in refractive index, which then leads to different resonant frequencies in different spatial regions of the device. By spatially correcting the lattice constant to compensate for the current-induced refractive index change, a laterally larger standing field can be maintained. This approach has enabled 3-mm-sized GaAs-based devices with a divergence angle of 0.05° and an output power of 50 W under CW operation [139].

3.2 PCSEL Fundamentals

3.2.1 Vertical mode profile

In PCSELs, unlike conventional semiconductor lasers, the optical cavity is created by a 2D photonic crystal. The photonic crystals support

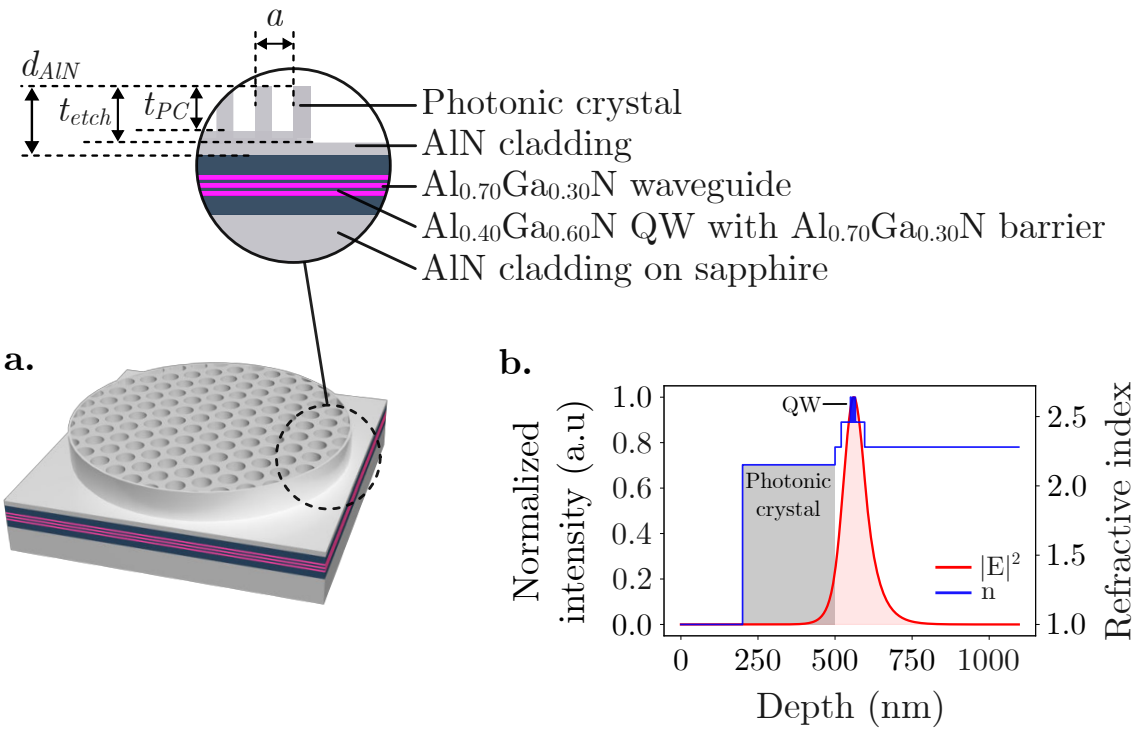


Figure 3.3: a. Schematic of the UV-C PCSEL and its epitaxial layers. **b.** Refractive-index profile overlaid with the vertical mode intensity for a PCSEL with a 300-nm-deep photonic crystal and a 10% hole filling factor.

modes with vanishing group velocities, which form a 2D standing wave. This standing wave is diffracted by the photonic crystal through Bragg diffraction and emitted from the surface. As in EELs, the waveguide and the cladding layers provide vertical confinement. A simple PCSEL structure comprises a waveguide between two cladding layers and a photonic crystal placed close to the waveguide to ensure that the optical mode has an overlap with the photonic crystal.

Figure 3.3a shows the schematic and the epitaxial layer stack of the UV-C PCSELs used in this work. From bottom to top, the layers consist of a sapphire substrate, followed by a 1730 nm bottom AlN cladding, a 76-nm-thick $Al_{0.70}Ga_{0.30}N$ waveguide core with three 2-nm-thick $Al_{0.40}Ga_{0.60}N$ QWs separated by 5-nm-thick $Al_{0.70}Ga_{0.30}N$ barriers, and a top AlN cladding. Two top cladding thicknesses (d_{AlN}) were used: 100 nm and 320 nm, with 320 nm used unless stated otherwise. The devices have hexagonal or square lattices of circular holes, with different lattice constants (a) and etch depths (t_{etch}). t_{etch} indicates the height of the photonic crystal mesa, while t_{pc} is the depth inside the holes as illustrated in Figure 3.3a.

Figure 3.3b shows the refractive index profile overlaid with the fundamental mode intensity profile along the vertical direction calculated using the Transfer Matrix Method [140]. The refractive indices used for the calculations are 2.28, 2.46 and 2.64 for AlN, $Al_{0.70}Ga_{0.30}N$ and $Al_{0.40}Ga_{0.60}N$, respectively, at a wavelength of 275 nm. The layers are terminated with 200 nm air at the top and 500 nm AlN cladding at the bottom. The photonic crystal depth (t_{PC}) is 300 nm with a hole filling factor (FF) of 10%, defined as the ratio of the air hole area to the unit cell area. The refractive index of the photonic crystal layer can be approximated as the weighted average of the refractive indices of AlN (n_{AlN}) and air (n_{air}): $n_{\mathrm{AlN}} \times (1 - FF) + n_{\mathrm{air}} \times (FF)$. Here, the lattice type is not relevant as the photonic crystal layer is modeled using an effective refractive index based on FF. The photonic crystal confinement factor, Γ_{PC} and QW confinement factor, Γ_{QW} were calculated using

$$\Gamma_{\mathrm{PC}} = \frac{\int_{\mathrm{PC}} \varepsilon(z)|E(z)|^2\,dz}{\int_{\mathrm{all}} \varepsilon(z)|E(z)|^2\,dz}, \tag{3.1}$$

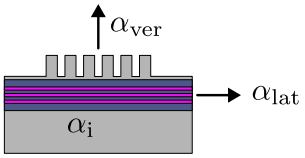
$$\Gamma_{\mathrm{QW}} = \frac{\int_{\mathrm{QW}} \varepsilon(z)|E(z)|^2\,dz}{\int_{\mathrm{all}} \varepsilon(z)|E(z)|^2\,dz}, \tag{3.2}$$

where $E(z)$ is the electric field amplitude and $\varepsilon(z)$ is the relative permittivity as a function of the vertical coordinate. Γ_{PC} and Γ_{QW} are estimated to be 5.4% and 5.8%, respectively. For a PCSEL with a thinner top AlN cladding layer (e.g., $d_{AlN} = 100$ nm) the air/surface interface could perturb the evanescent tail of the optical mode, push the mode down and reduce the confinement factors. For $d_{AlN} = 320$ nm, the layer is sufficiently thick for the optical mode to fully decay before reaching the interface, so the confinement factors are not affected by the air. These confinement factors are important for the lasing threshold of PCSELs and will be discussed later in this thesis. The threshold condition in PCSELs can be written as

$$\Gamma_{\mathrm{QW}}\, g_{\mathrm{mat}} = \alpha_{\mathrm{ver}} + \alpha_{\mathrm{lat}} + \alpha_{\mathrm{i}}. \tag{3.3}$$

Here, g_{mat} is the threshold material gain, α_{ver} represents the vertical losses, which correspond to radiation losses, α_{lat} represents the lateral losses due to finite size and α_{i} represents the internal losses caused by

scattering or optical absorption, as depicted in Figure 3.4. The radiative efficiency of a PCSEL, η_{rad}, can be defined as the ratio of the vertical radiation loss to the total loss. Γ_{QW} directly affects the modal gain, whereas Γ_{PC} influences the loss terms α_{ver} and α_{lat}. A higher Γ_{QW} increases the modal gain, therefore reduces the required material gain. A higher Γ_{PC} decreases α_{lat} as the in-plane coupling strength increases, but it also increases radiative losses α_{ver} as the mode is diffracted more strongly.



$$\eta_{\mathrm{rad}} = \frac{\alpha_{\mathrm{ver}}}{\alpha_{\mathrm{ver}} + \alpha_{\mathrm{lat}} + \alpha_{\mathrm{i}}}$$

Figure 3.4: Loss mechanisms and radiative efficiency in PCSELs.

3.2.2 Photonic crystals and photonic band structure

2D photonic crystals have periodically alternating refractive indices which create a photonic band structure [141, 142]. This is analogous to the electronic band structure created by the periodic arrangement of atoms in a lattice. The photonic band structure shows the allowed eigenmodes together with their frequencies and wave vectors and governs their propagation. To calculate the band structure of a photonic crystal, we start with Maxwell's curl equations for an isotropic and non-magnetic ((permeability identical to vacuum/free space)) medium in the absence of a source or a sink.

$$\nabla \times \mathbf{E}(\mathbf{r},t) + \mu_0 \frac{\partial \mathbf{H}(\mathbf{r},t)}{\partial t} = 0, \qquad \nabla \times \mathbf{H}(\mathbf{r},t) - \varepsilon_0 \varepsilon(\mathbf{r}) \frac{\partial \mathbf{E}(\mathbf{r},t)}{\partial t} = 0, \quad (3.4)$$

where $\varepsilon(\mathbf{r})$ is the varying relative electric permittivity as a function of position, ε_0 is the permittivity of free space and μ_0 is the permeability of free space.

Assuming fields that vary as $e^{-i\omega t}$, after eliminating the electric field and removing the time dependence, we obtain the master equation

$$\nabla \times \left(\frac{1}{\varepsilon(\mathbf{r})} \nabla \times \mathbf{H}(\mathbf{r}) \right) = \left(\frac{\omega}{c} \right)^2 \mathbf{H}(\mathbf{r}), \quad (3.5)$$

where $c = 1/\sqrt{\varepsilon_0 \mu_0}$ is the speed of light in vacuum.

Since the refractive index profile is periodic, we can use Bloch's theorem to write magnetic fields as:

$$\mathbf{H_k}(\mathbf{r}) = e^{i\mathbf{k}\cdot\mathbf{r}}\mathbf{u_k}(\mathbf{r}), \tag{3.6}$$

where $\mathbf{k}$ is the wave vector and $\mathbf{u_k}(\mathbf{r})$ is a function that describes the periodicity of the lattice.

For a 2D photonic crystal that is uniform along the z-axis, the field can be expressed as two independent polarizations: transverse electric (TE), where the magnetic field is out-of-plane and transverse magnetic (TM), where the electric field is out-of-plane. In the TE case, we can reduce the master equation to the Hermitian scalar wave equation

$$-\nabla\cdot\left(\frac{1}{\varepsilon(\mathbf{r})}\nabla H_z(\mathbf{r})\right) = \left(\frac{\omega}{c}\right)^2 H_z(\mathbf{r}). \tag{3.7}$$

Any arbitrary reciprocal lattice vector $\mathbf{G}$ can be written using the reciprocal lattice basis vectors $\mathbf{K}_1$ and $\mathbf{K}_2$ as

$$\mathbf{G} = m\mathbf{K}_1 + n\mathbf{K}_2, \qquad m, n \in \mathbb{Z}. \tag{3.8}$$

The inverse relative permittivity that describes the periodic variation can be written as a Fourier series using the reciprocal lattice vector $\mathbf{G}$ as

$$\frac{1}{\varepsilon(\mathbf{r})} = \sum_{\mathbf{G}} u_{\mathbf{G}} e^{i\mathbf{G}\cdot\mathbf{r}}, \tag{3.9}$$

and the scalar Bloch function that describes the periodicity of the lattice can be written using $\mathbf{G}$ as

$$u_{\mathbf{k}}(\mathbf{r}) = \sum_{\mathbf{G}} c_{\mathbf{G}}(\mathbf{k}) e^{i\mathbf{G}\cdot\mathbf{r}}, \tag{3.10}$$

where $u_{\mathbf{G}}$ and $c_{\mathbf{G}}(\mathbf{k})$ are the Fourier coefficients of the permittivity and the magnetic field, respectively. By substituting Eq. 3.9 and Eq. 3.10 into Eq. 3.7, it can be converted into an algebraic eigenvalue problem. The most widely adopted way to solve Eq. 3.7 is the Plane Wave Expansion (PWE) method [143].

To apply the 2D PWE method to calculate the band structure of a 3D PCSEL, which incorporates a vertical structure and a 2D photonic crystal pattern, a 2D photonic crystal can be used with effective permittivities estimated using the two conditions provided in [144],

$$FF\varepsilon_a + (1 - FF)\varepsilon_b = n_{\text{eff}}^2, \tag{3.11}$$

$$\Delta\varepsilon = \varepsilon_b - \varepsilon_a, \tag{3.12}$$

here, $\Delta\varepsilon$ denotes the effective permittivity difference multiplied by Γ_{PC}. Using $n_{\text{eff}} = 2.31$, $\Gamma_{\text{PC}} = 5.4\%$ and $FF = 10\%$, the calculated values are $\varepsilon_a = 5.1321$ for the air hole and $\varepsilon_b = 5.3588$ for AlN.

Figure 3.5a and 3.5b present a hexagonal lattice and its reciprocal lattice, respectively; and Figure 3.5c presents the TE-mode photonic band structure along the symmetry points, calculated using the 2D PWE method [145]. Figure 3.5d displays the 3D band structure as a complementary view. Figure 3.6a to Figure 3.6d illustrate the corresponding results for a square lattice, calculated with the same numerical parameters. The six-fold symmetry of the hexagonal lattice produces six band-edge modes at the Γ-point (labeled A, B_1, B_2, C, D_1, D_2, in increasing energy order), where the group velocity of light ($v_g = \mathrm{d}\omega/\mathrm{d}k$) vanishes, while the square lattice yields four band-edge modes (labeled A, B, C, D, in increasing energy order) due to its four-fold symmetry.

The out-of-plane (H_z) magnetic field distribution of these modes, calculated using the finite element solver COMSOL Multiphysics® [146], is shown in Figure 3.7. The in-plane electric fields are overlaid as an arrow plot. In the hexagonal photonic crystal, the A, B_1, B_2 and C modes have perfectly antisymmetric electric fields that undergo destructive interference and thus cancel out along the normal direction (Figure 3.7a). Therefore, in an infinite photonic crystal with circular holes, they are confined in the structure and have zero radiation losses, i.e., $\alpha_{\text{ver}} = 0$ [147]. Such modes are called non-leaky modes. In practice, however, photonic crystals have finite sizes. Their boundaries introduce field asymmetry and lead to radiation. Imperfections caused by fabrication and any non-uniformity in the structure also create local field asymmetry and contribute to radiation. In the D_1 and D_2 modes, the electric fields are not antisymmetric; therefore, they do not experience complete destructive interference and leak out. These modes are leaky modes and they exhibit higher radiation losses compared to the other band-edge modes. This increases their lasing threshold, and they therefore are generally not favored for lasing [148]. For a finite-sized photonic crystal with circular holes, α_{ver} and α_{lat} scale approximately with $1/L^2$ and $1/L^3$, respectively, where L is the size of the photonic crystal [149]. For the non-leaky band-edge modes, α_{ver} decreases as the device size

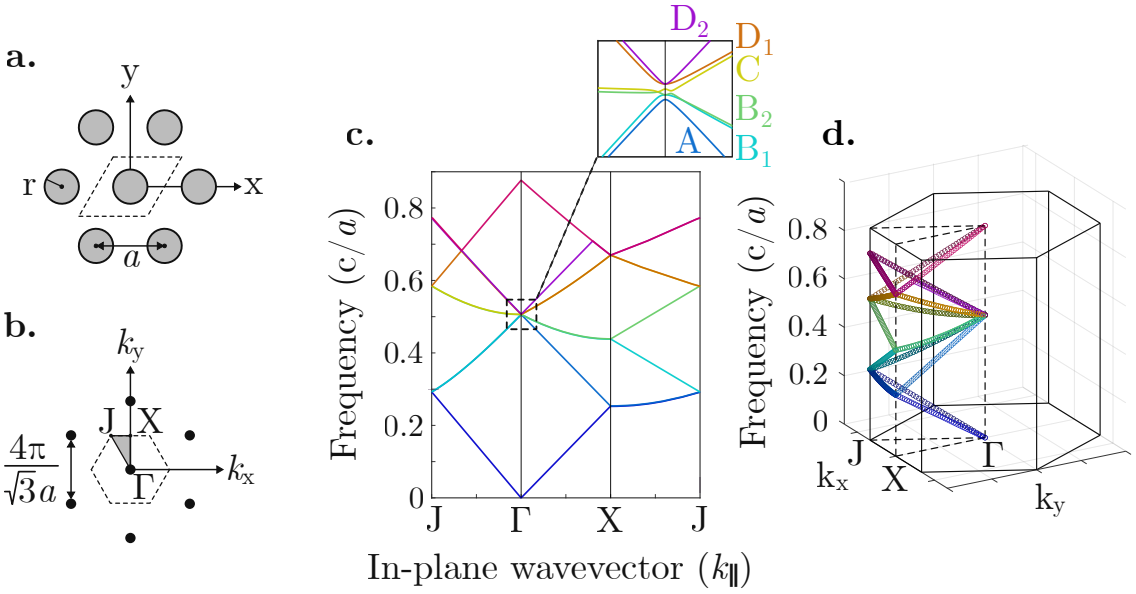


Figure 3.5: **a.** Hexagonal lattice with circular holes and **b.** its reciprocal space. The reciprocal lattice positions **G** are indicated by the black dots. **c.** 2D and **d.** 3D band structures of an AlN/air photonic crystal with a hexagonal lattice of circular holes and 10% FF, calculated using the 2D PWE method.

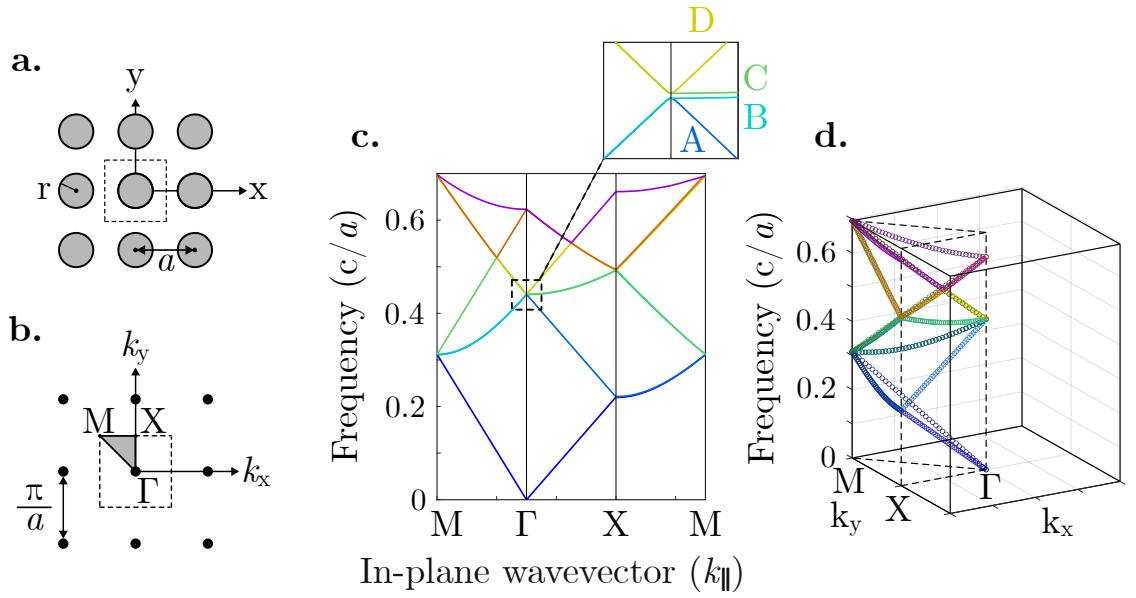


Figure 3.6: **a.** Square lattice with circular holes and **b.** its reciprocal space. The reciprocal lattice positions **G** are indicated by the black dots. **c.** 2D and **d.** 3D band structures of an AlN/air photonic crystal with a square lattice of circular holes and 10% FF, calculated using the 2D PWE method.

increases, indicating that the power outcoupled, therefore, the slope efficiency decreases. Ultimately, it would approach zero as the size becomes

infinitely large. In the case of the square lattice (Figure 3.7b), the A and B modes are antisymmetric, therefore non-leaky and do not outcouple in an infinite photonic crystal, whereas the C and D modes are not antisymmetric and exhibit radiation losses [150].

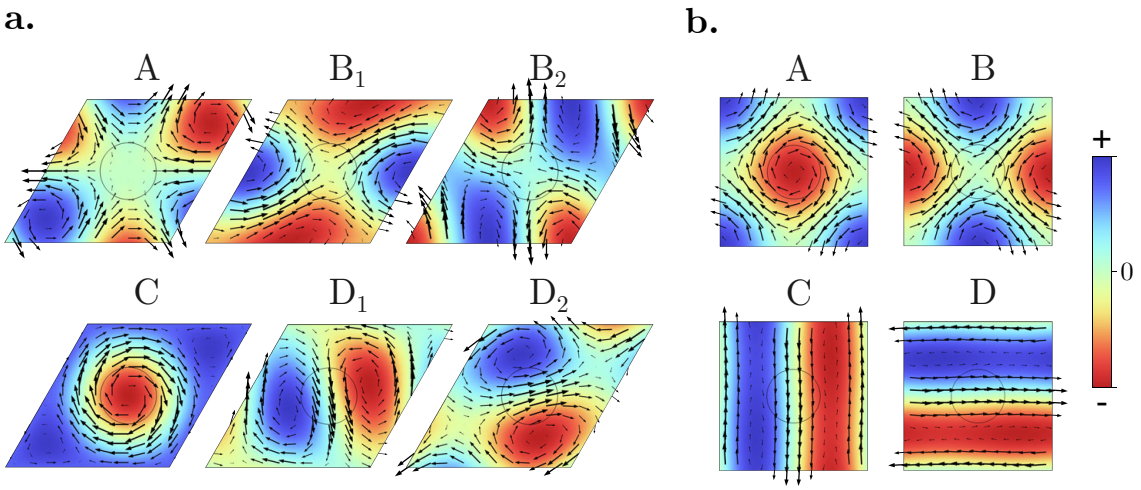


Figure 3.7: Out-of-plane magnetic field distributions (colors) and the in-plane electric field vectors (arrows) of the band-edge modes of an infinite photonic crystal with **a.** a hexagonal ($FF = 10\%$) and **b.** a square lattice ($FF = 10\%$) of circular holes.

3.2.3 Coupling mechanisms

In a 2D photonic crystal with reciprocal lattice basis vectors $\mathbf{K}_1$ and $\mathbf{K}_2$, coupling occurs if the following two conditions are satisfied

$$\boldsymbol{k_d} = \boldsymbol{k_i} + m\mathbf{K}_1 + n\mathbf{K}_2, \qquad m, n \in \mathbb{Z}, \tag{3.13}$$

$$\boldsymbol{\omega_d} = \boldsymbol{\omega_i}. \tag{3.14}$$

Here, $\boldsymbol{k_d}$ and $\boldsymbol{k_i}$ represent the diffracted and incident wave vectors, respectively, while $\boldsymbol{\omega_d}$ and $\boldsymbol{\omega_i}$ denote the frequencies of the diffracted and incident waves.

In conventional 1D DFBs, coupling occurs only along a single axis due to the 1D periodicity and 1D propagation, resulting in the coupling of forward- and backward-propagating waves along the same axis [151]. 2D photonic crystals support coupling in multiple directions due to their 2D periodicity. In hexagonal lattices, coupling can occur at 60°, 120°,

180° and normal to the surface (Figure 3.8). The 60° ($\boldsymbol{k_d} = \boldsymbol{k_i} + \mathbf{K}_2$ and $\boldsymbol{k_d} = \boldsymbol{k_i} + \mathbf{K}_1 - \mathbf{K}_2$) and 120° ($\boldsymbol{k_d} = \boldsymbol{k_i} + \mathbf{K}_1 + \mathbf{K}_2$ and $\boldsymbol{k_d} = \boldsymbol{k_i} + 2\mathbf{K}_1 - \mathbf{K}_2$) cases result in 2D oscillations, thereby generating 2D standing fields. The 180° case corresponds to coupling along the same axis as the incident wave, as in 1D DFBs. This leads to 1D oscillations, which could prevent the formation of a 2D standing wave.

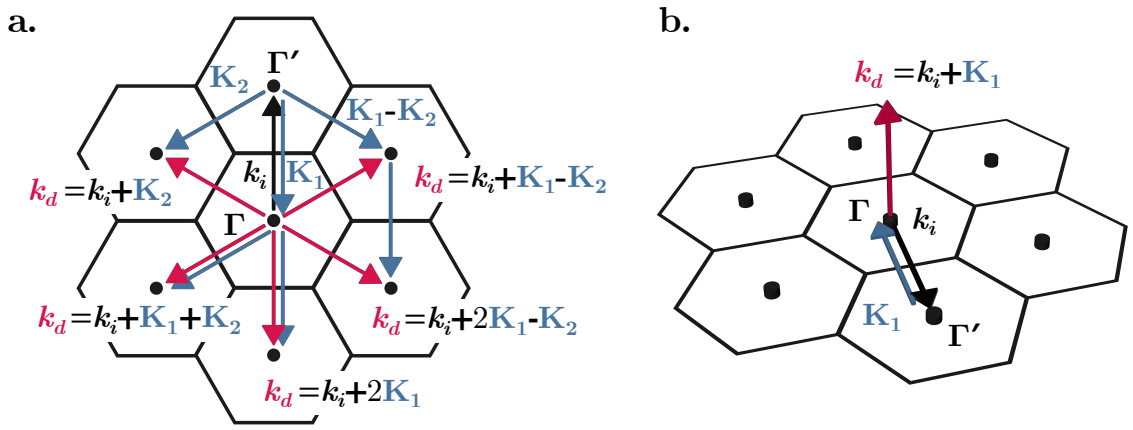


Figure 3.8: Vector diagram of **(a)** in-plane (60°, 120°, 180°) and **(b)** out-of-plane coupling in hexagonal lattice photonic crystals.

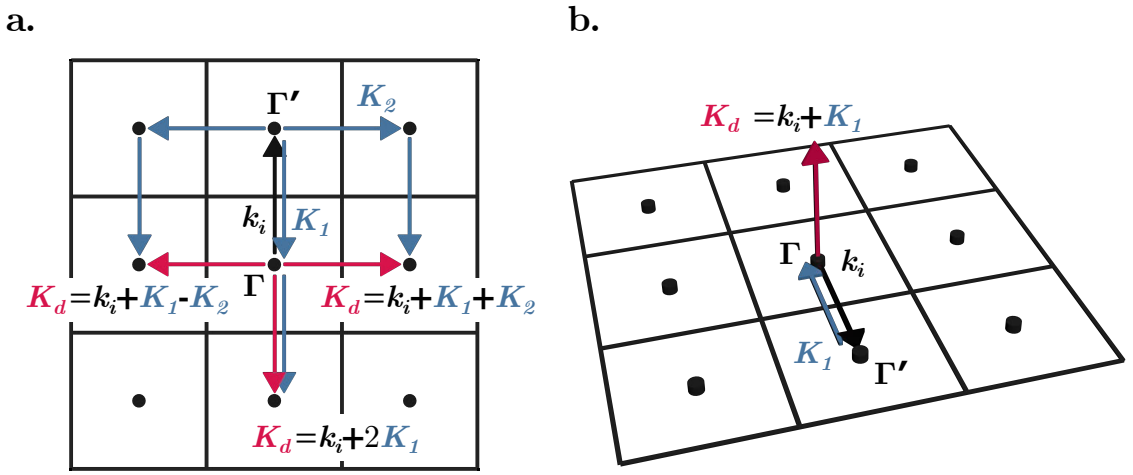


Figure 3.9: Vector diagram of **(a)** in-plane (90°, 180°) and **(b)** out-of-plane couplings in square lattice photonic crystals.

In square lattices, coupling occurs in 90° ($\boldsymbol{k_d} = \boldsymbol{k_i} + \mathbf{K}_1 - \mathbf{K}_2$ and $\boldsymbol{k_d} = \boldsymbol{k_i} + \mathbf{K}_1 + \mathbf{K}_2$) and 180°($\boldsymbol{k_d} = \boldsymbol{k_i} + 2\mathbf{K}_1$) (Figure 3.9). 90° coupling is responsible for 2D fields whereas 180° leads to 1D oscillations. The 90°

coupling forms a 2D standing wave, while the 180° case is similar to the 180° case in hexagonal lattices and 1D DFBs. If coupling predominantly occurs at 180°, in both square and hexagonal lattices, the photonic crystal behaves as a 1D DFB [65, 152], which leads to a highly divergent emission [79]. In that case, mode competition may arise between waves oscillating in different crystallographic directions, leading to multimode lasing [153]. In PCSELs, 2D oscillations are desired because they lead to a 2D standing field and low-divergence emission.

To better understand whether a device will show dominant 1D or 2D lasing, it can be helpful to have a closer look at the coupling constants, which quantify the strength of Bragg scattering and the rate of energy transfer between the modes [154]. For a hexagonal lattice, they can be derived from the frequencies of the band-edge modes at the Γ-point using the equations given in [155]

$$\kappa_1 = \frac{2(-\omega_A - \omega_B + \omega_C + \omega_D)}{\omega_A + 2\omega_B + \omega_C + 2\omega_D}\,\beta_0, \tag{3.15}$$

$$\kappa_2 = \frac{2(-\omega_A + \omega_B - \omega_C + \omega_D)}{\omega_A + 2\omega_B + \omega_C + 2\omega_D}\,\beta_0, \tag{3.16}$$

$$\kappa_3 = \frac{\omega_A - 2\omega_B - \omega_C + 2\omega_D}{\omega_A + 2\omega_B + \omega_C + 2\omega_D}\,\beta_0, \tag{3.17}$$

where $\beta_0 = 4\pi/\sqrt{3}a$, and ω_A, ω_B, ω_C and ω_D are the frequencies of the band-edge modes. ω_B and ω_D represent the frequencies of the degenerate modes B_1-B_2 and D_1-D_2, respectively. The κ_1 and κ_2 are the coupling constants representing the waves that couple at 60° and 120°, i.e., responsible for 2D oscillations. κ_3 is the coupling constant that represents counter-propagating waves, i.e., 180 degree coupling, that are responsible for 1D oscillations.

Figure 3.10 shows the calculated band-edge frequencies using the 2D PWE and the calculated coupling constants calculated using Eq. 3.15–3.17. The PCSEL used in the simulation has (a = 140 nm, d_{AlN} = 100 nm, t_{PC} = 70 nm) and the permittivities were estimated using Eq. 3.11 and 3.12. For low FFs (<10%), the 1D and 2D coupling constants have similar values and increase up to 10% FF. This indicates competition between 1D and 2D coupling for the low FF regime. At approximately 10% FF, the 1D coupling constant κ_3 reaches its maximum value while the 2D coupling constants continue to increase.

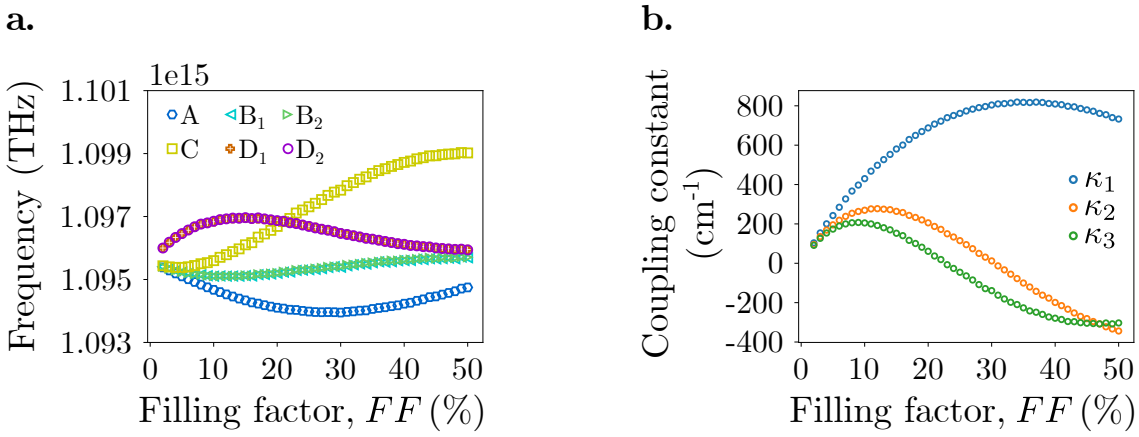


Figure 3.10: a. Calculated band-edge frequencies at the Γ-point for a PCSEL with a hexagonal lattice (a = 140 nm, d_{AlN} = 100 nm, t_{PC} = 70 nm) as a function of FF using the 2D PWE and **b.** coupling constants of the same PCSEL as a function of FF, derived from the band-edge frequencies.

Chapter 4

Optically Pumped UV-C Photonic-Crystal Surface-Emitting Lasers

4.1 Regrowth-free Approach

The fabrication method is a regrowth-free approach that eliminates the need for a complex regrowth step that affects the final photonic crystal dimensions and simplifies the overall process. In addition, if any gain peak variation occurs across the wafer, the lattice constant of the photonic crystal can be precisely matched to the gain peak since the etching is done after the QWs are grown. However, this also makes the QWs vulnerable to deep, harsh etching. If the photonic crystal is etched too deep, it can cause plasma-induced damage to the QWs and introduce non-radiative recombination centers [156–158]. Such damage may degrade the PL emission of the QWs, reduce device performance or even prevent lasing.

In contrast, in regrown PCSELs, the photonic crystal is etched prior to the growth of the active layers. A key advantage of regrown PCSELs is that, since the active layer is not present during etching, it doesn't pose the risk of plasma-induced damage to the QWs. However, in these devices, the gain spectrum of the active layers must be matched to the lattice constant. If the gain spectrum varies across the wafer and does not match the lattice constant, the threshold current or pump power density may increase.

4.1.1 Fabrication

In this thesis, two different epitaxial materials are used, both sharing the same design except for the top AlN cladding thickness, which is 100 nm for one and 320 nm for the other. The epitaxial layer stacks of the optically pumped UV-C PCSELs were grown on high-temperature-annealed AlN on a sapphire substrate by metal-organic chemical vapour deposition [159, 160]. Atomic force microscope (AFM) measurements were performed over 25 × 25 μm^2 and 5 × 5 μm^2 areas on the as-grown surface of the epitaxial material with a 320 nm cladding, as shown in Figure 4.1. The root mean square (RMS) roughness was measured to be 2.2 nm over a 25 × 25 μm^2 area. The mean peak-to-valley height (R_z) was 6.5 nm. While RMS roughness provides a statistical measure of the surface morphology, R_z is especially important since the photonic crystal is etched directly into the top cladding layer. When the peak-to-valley height is high, the photonic crystal may have different distances to the optical mode across the device. Depending on the origin and location of non-uniformities within the layers, they may induce variations in Γ_{PC} across the photonic crystal area.

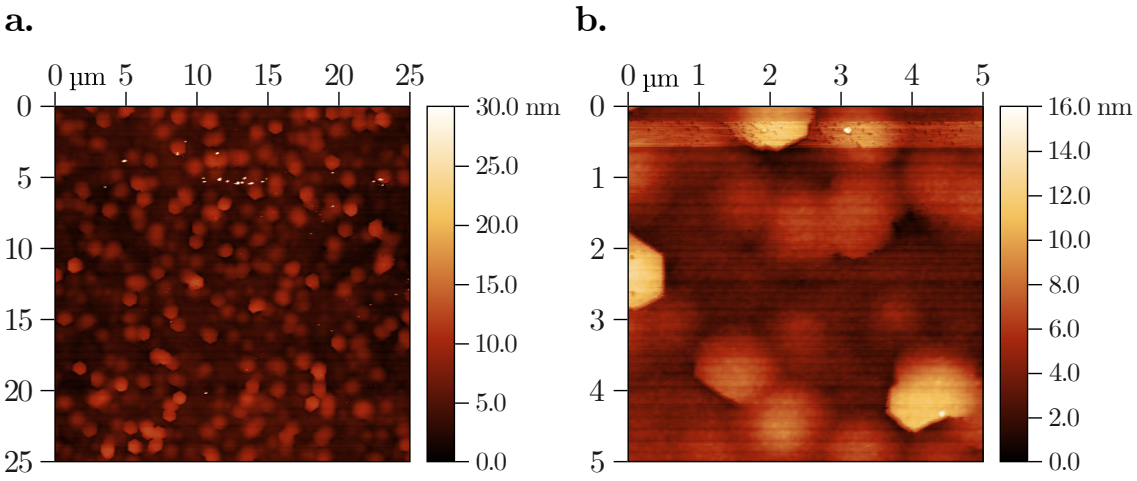


Figure 4.1: Atomic force microscopy measurements showing the surface morphology of the as-grown material over scan areas of **a.** 25μm^2 and **b.** 5μm^2.

The process flow is illustrated in Figure 4.2. Fabrication begins with a 3-minute acetone/isopropanol (IPA) cleaning, followed by a 1-minute dip in buffered oxide etchant (BOE). Photonic crystal patterns were defined by electron-beam lithography using an 80-nm-thick e-beam resist, hydrogen silsesquioxane (HSQ). HSQ is a high-resolution negative

resist that converts to SiO_x when exposed to e-beam or thermally annealed [161,162]. It exhibits high dry-etching resistance. After the lithography step, the resist was developed using a NaCl/NaOH developer for 2 minutes. Although the salty developer requires higher doses in the e-beam exposure, it provides superior resolution compared to tetramethylammonium hydroxide (TMAH)-based developers [163]. Using the resist as a hard mask, the photonic crystals were directly transferred into the top AlN cladding layer by Cl_2/Ar dry etching (Cl_2: 30 sccm, Ar: 15 sccm, ICP power: 300 W, RIE power: 38 W, pressure: 2 mTorr) down to different depths (i.e., different values of t_{etch}). After photonic crystal etching, the remaining resist was removed with BOE.

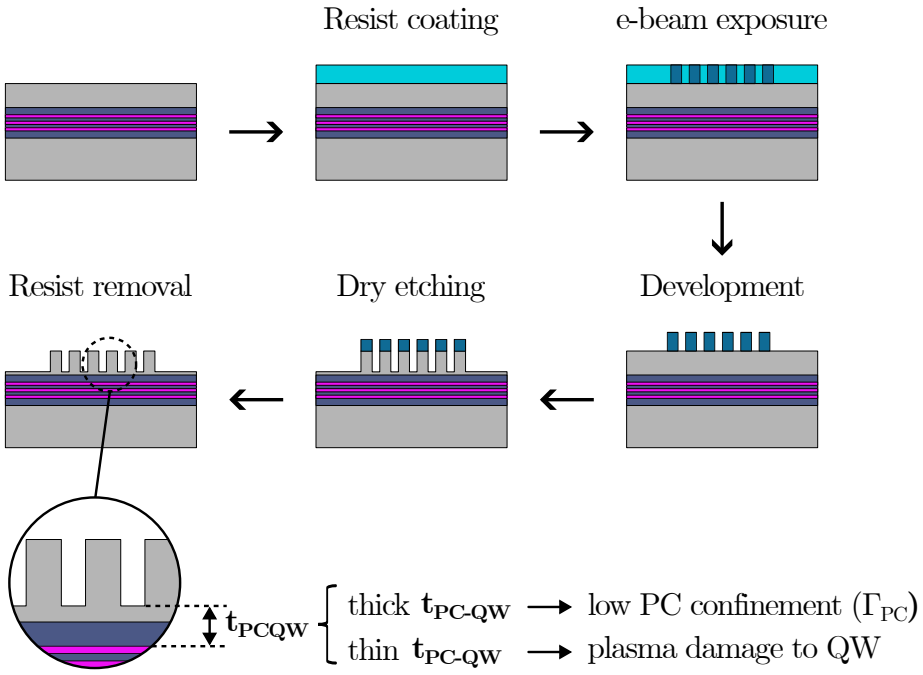


Figure 4.2: Process flow for optically pumped UV-C PCSELs.

4.1.2 Optical confinement

In the regrowth-free approach, the etch depth is important because it directly affects Γ_{PC} and Γ_{QW}. Shallow photonic crystal etching results in a low Γ_{PC} and, consequently, a poor photonic crystal overlap. A poor overlap leads to an increased threshold [164].

Figure 4.3 shows Γ_{PC} and Γ_{QW} as a function of photonic crystal depth for different values of FF, calculated using Eq. 3.1 and Eq. 3.2, for a 320-nm-thick top cladding. For a fixed depth of 300 nm, Γ_{PC} is

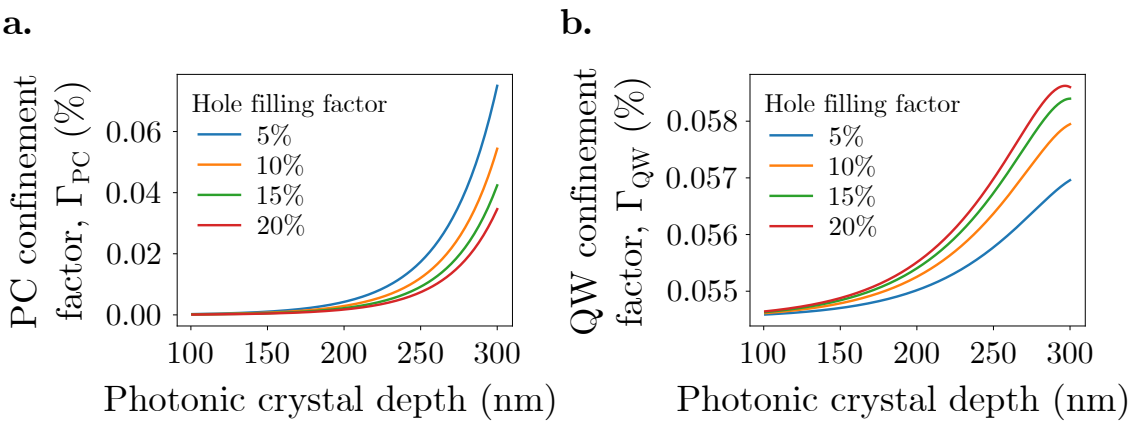


Figure 4.3: **a.** Γ_{PC} and **b.** Γ_{QW} for PCSELs with different values of FF as a function of photonic crystal depth, for a 320-nm-thick top cladding.

increasing with decreasing FF, for example Γ_{PC} is 7.5% for a 5% FF, and 3.5% for a 20%. This is due to the decrease in the effective refractive index for larger FFs, which essentially pushes the optical mode down and causes poorer photonic crystal overlap. Γ_{PC} increases with increasing photonic crystal depth for all values of FF, since an increasing etch depth places the photonic crystal closer to the field intensity in the waveguide. For a photonic crystal depth of 200 nm, which leaves a distance of 150 nm between the bottom of the photonic crystal hole and the first QW, Γ_{PC} is ~0.4% for $FF = 5\%$. Therefore, it is essential to have sufficient photonic crystal depth to not suffer from poor confinement and an increased threshold. Γ_{QW}, on the other hand, is less sensitive to photonic crystal depth. When the depth is 300 nm and the $FF = 20\%$, it reaches a maximum value of 5.9%. The lowest Γ_{QW} is 5.5% when $FF = 5\%$ and the depth is 100 nm, which is the shallowest depth explored here.

4.2 Optically Pumped UV-C PCSEL Characterization

Figures 4.4a and 4.4b show the top-view SEM images of two PCSELs with hexagonal and square lattices after photonic crystal etching and resist removal. Among the fabricated PCSELs, these two specific devices will hereafter be referred to as H-PCSEL and S-PCSEL, respectively. Both devices have a photonic crystal mesa diameter of 120 μm. The lattice constants are 138 nm for H-PCSEL and 120 nm for S-PCSEL.

The photonic crystal hole diameters at the top are 98 nm and 83 nm for the H-PCSEL and the S-PCSEL, respectively. Different hole sizes were intentionally fabricated with the aim of obtaining similar FF values for both PCSELs. The etching depth t_{etch} measured using the step height outside the photonic crystal region is 361 nm. Although the holes were designed to be circular, they became slightly hexagonal after etching. This can be explained by the Cl_2 plasma etch rate dependency on the crystallographic orientation in AlN, which has previously been reported when etching GaN [165].

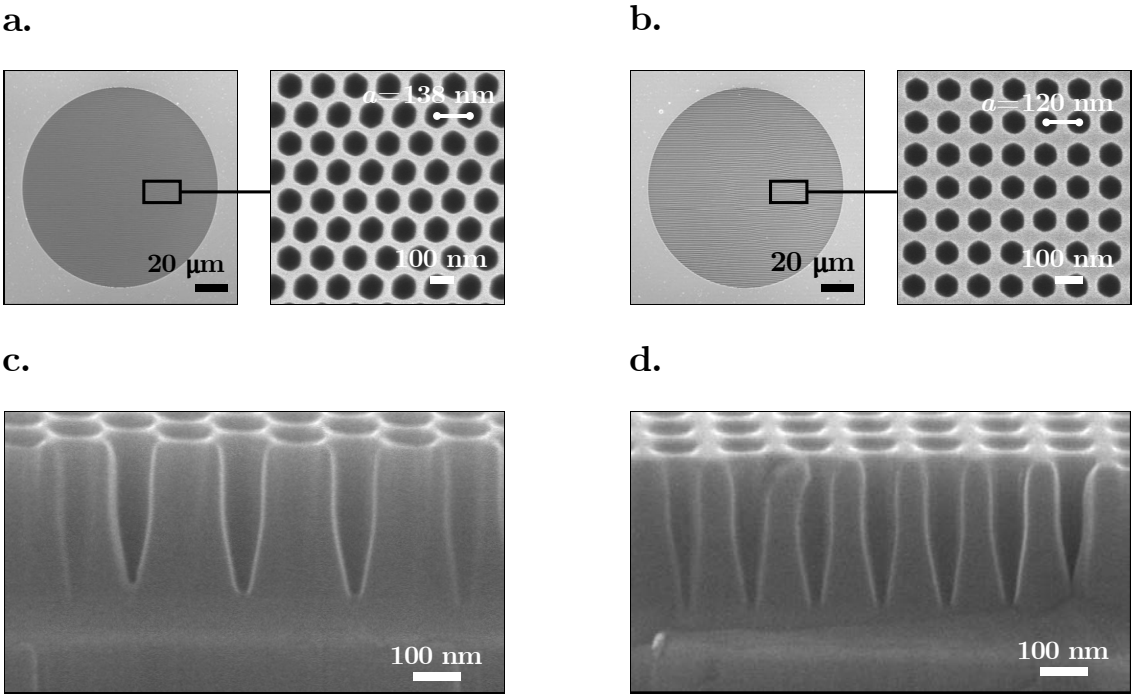


Figure 4.4: Top-view SEM images of PCSELs with **a.** a hexagonal (H-PCSEL, a = 138 nm) **b.** a square lattice (S-PCSEL, a = 120 nm). **c.**, **d.** Representative cross-sectional SEM images showing the photonic crystal etch profiles, obtained from a hexagonal and a square lattice PCSEL etched under similar conditions.

Figures 4.4c and 4.4d show representative cross-sectional SEM images that were obtained from different PCSELs etched under similar conditions. t_{etch} was measured to be 324 nm, which yielded a t_{PC} of 290 nm. In the cross-section views, the photonic crystals have steep sidewalls approximately in the top 150 nm and gradually taper toward the bottom, narrowing to ∼20 nm. This tapered profile yields a depth-dependent FF in the vertical direction, making it difficult to define a single value. All

the stated FF values represent the FF at the top of the photonic crystal, even though the effective FF at the bottom of the photonic crystal is smaller.

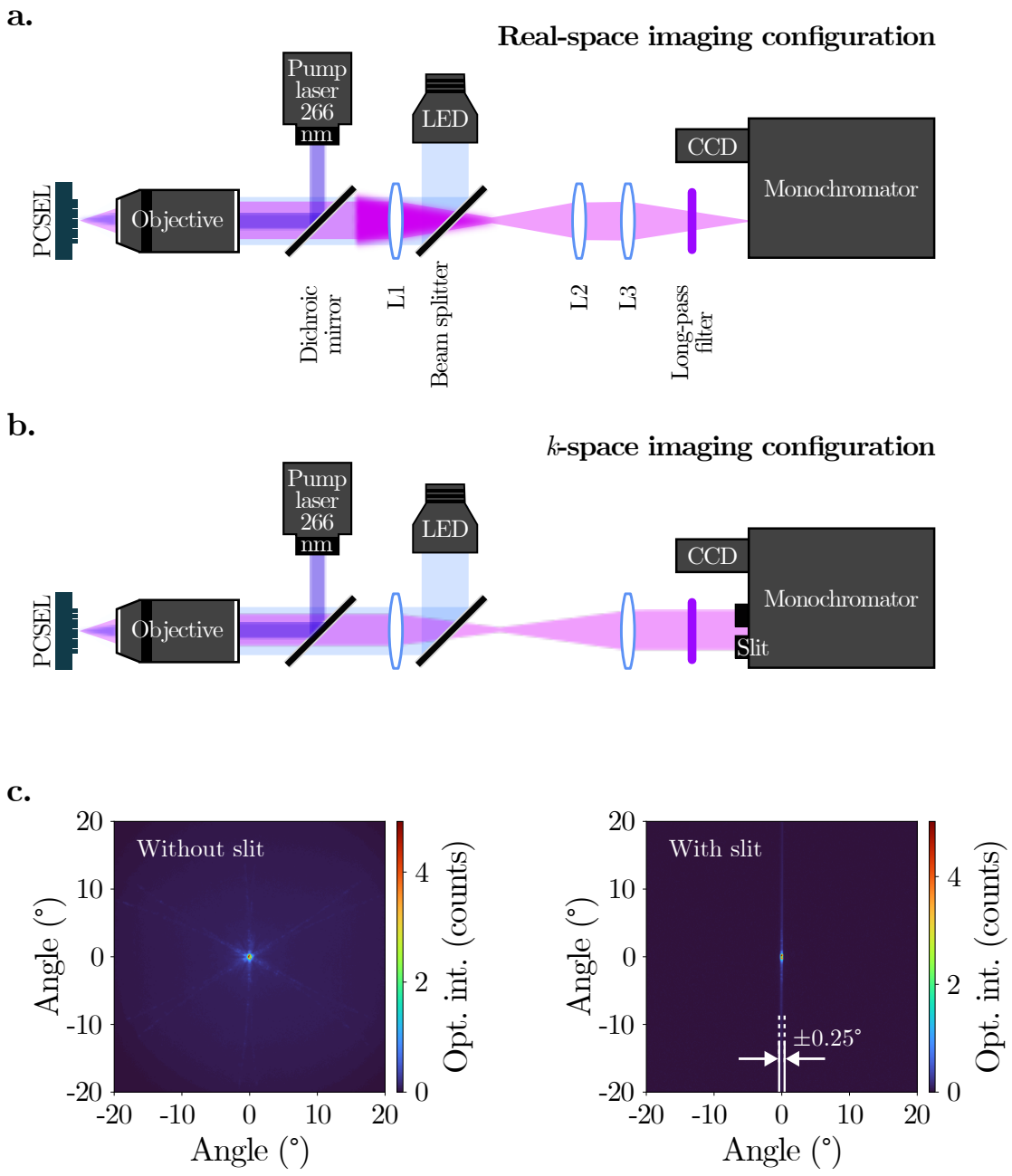


Figure 4.5: Illustration of the experimental setup configurations for **a.** real-space (near field) and **b.** k-space (far field, band structure) measurements. **c.** Example of two far-field measurements obtained with and without using the slit at the entrance of the spectrometer.

The PCSELs were pumped optically from the photonic crystal side with a 266-nm pulsed frequency-quadrupled Nd:YAG laser (repetition rate: 100 Hz, pulse width: 0.55 ns) at room temperature. The characterizations were performed using an imaging spectrometer (Princeton Instruments SpectraPro HRS-750). The experimental setup is illustrated in Figure 4.5. Two main configurations were used in the setup: i) real-space and ii) k-space measurement configurations. Figure 4.5a depicts the real-space imaging configuration. To capture the k-space information, which corresponds to the far-field emission pattern because a lens naturally performs a spatial Fourier transform, mapping propagation angles to spatial positions at its back focal plane, the lens L2 was removed, as shown in Figure 4.5b, which allowed imaging the Fourier plane on the spectrometer entrance. All the light within the numerical aperture (NA = 0.39) was collected with an objective (Thorlabs LMU-20X-UVB) and imaged onto a CCD. The pump beam reflected by the sample was filtered by the long-pass filter before entering the spectrometer. For the band structure measurements, the k-space configuration was used with a slit at the entrance of the spectrometer that allowed only the light within $\pm 0.25^\circ$ to pass (Figure 4.5c). The light is then resolved into wavelengths by a grating. The LED was used to visually locate the PCSELs and to ensure that the pump beam is aligned with the device area.

4.3 Proof of Lasing

4.3.1 Input vs. output intensity

The PCSELs were optically pumped over a range of pump power densities with a slightly elliptical pump beam spot size of 304 $\times$ 237 μm^2 at full-width half-maximum (FWHM). Figure 4.6 shows the output intensity as a function of pump power density. The output intensity is integrated over $\pm$120 pm around the lasing peaks. Both PCSELs exhibit similar lasing thresholds, 5.1 MW/cm^2 for the H-PCSEL and 5.4 MW/cm^2 for the S-PCSEL. It is worth noting that the pump wavelength is absorbed only by the QWs, whereas the barriers are transparent. Electron-hole pairs are generated only in the QWs; therefore, the barriers do not contribute through diffusion.

A portion of the pump beam is reflected by the photonic crystal. Figure 4.7 shows the reflectance of PCSELs with two different FFs (d_{AlN}: 100 nm, t_{etch}: 70 nm) measured using white light reflectance spectroscopy. At the pump wavelength of 266 nm, the reflectivity is 17%

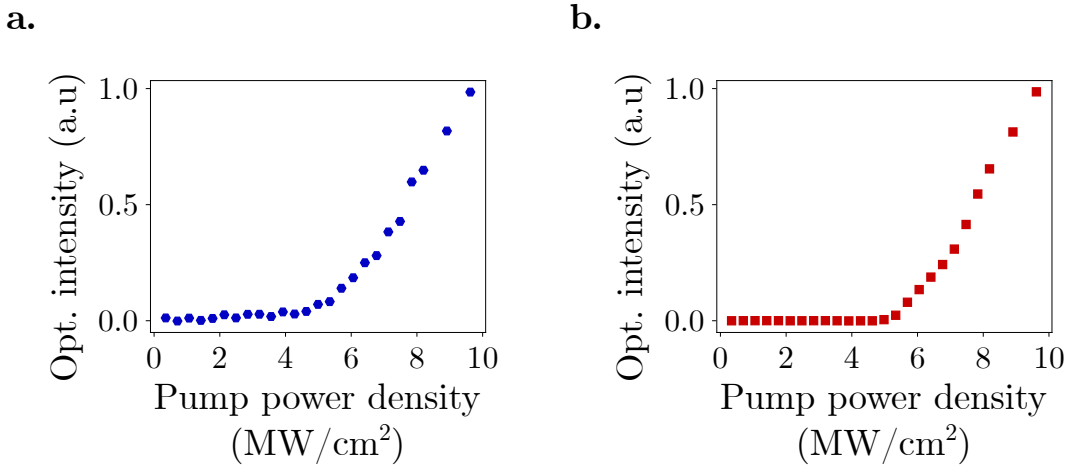


Figure 4.6: Output intensity as a function of pump power density for **a.** the H-PCSEL and **b.** the S-PCSEL.

for 18% FF and 20% for 13% FF. These values are comparable to the reflection from a planar AlN surface, which is approximately 15%, calculated using $((n_{AlN}-1)/(n_{AlN}+1))^2$. Thus, the effect of the reflection by different photonic crystals on pump power reaching the QWs is minimal.

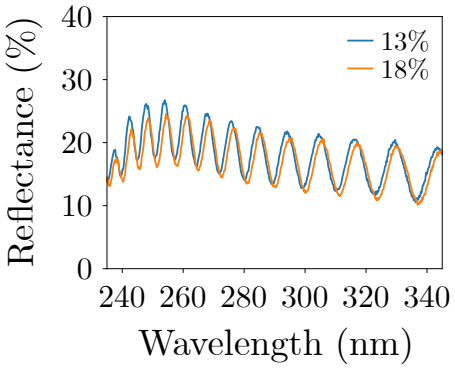


Figure 4.7: Measured reflectance of PCSELs with a hexagonal lattice (a = 140 nm, $FF = 13\%, 18\%$).

4.3.2 Photonic band structure and spectrum

When pumped below threshold, the PCSELs show distinct bands as seen in the simulation. Figure 4.8a shows the measured band structure of the H-PCSEL at 0.7 × threshold. The six band-edge modes are clearly visible

along the Γ-J and Γ-X directions. Here, the emission angle can also be translated into the in-plane wave vector $k_{\parallel}$ using $k_{\parallel} = \frac{2\pi n}{\lambda_0} \sin(\theta)$. At the Γ-point, the two uppermost modes (D_1, D_2) have higher intensities at the Γ-point compared to the other band-edge modes since they exhibit higher vertical radiation losses, i.e., higher α_{ver}, as explained in Section 3.2.2. The A mode, on the other hand, has lower vertical losses; therefore, it has a weaker intensity. In the square lattice, the four bands are visible along the Γ-X and Γ-M directions. Similarly, the uppermost D mode band has a higher intensity compared to the others, while the A mode is weaker.

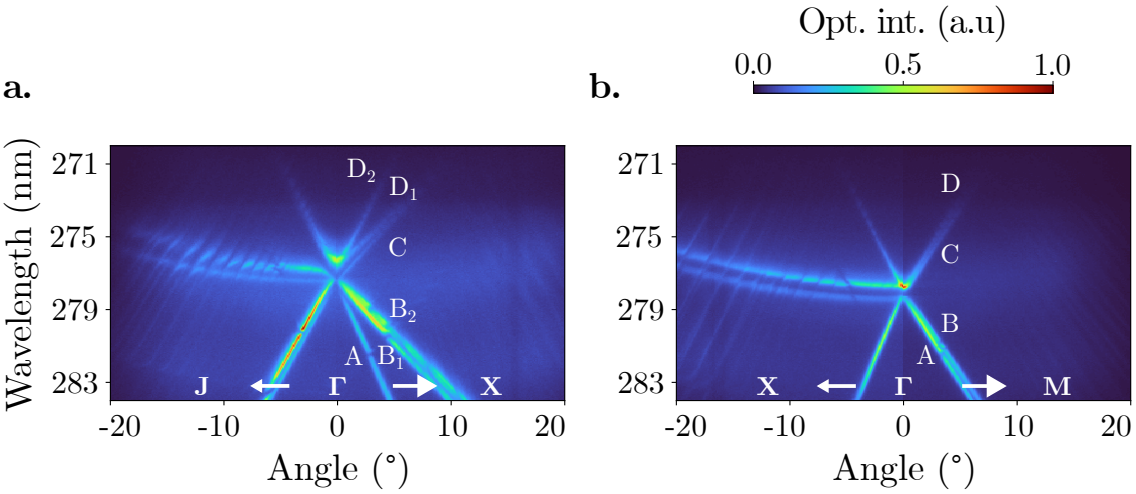


Figure 4.8: Below-threshold band structure of **a.** the H-PCSEL along the Γ–J and Γ–X directions and **b.** the S-PCSEL along the Γ–X and Γ–M directions, measured at ∼0.7 × threshold.

Both PCSELs exhibit dark lines in their band structures. In the H-PCSEL case, it is mainly along the Γ-J direction, while in the S-PCSEL case, it is along the Γ-X direction. These dark lines are attributed to higher-order vertical modes arising from the sapphire substrate and the thick AlN cladding [166]. The vertical structure supports multiple vertical modes due to the cladding and substrate, each of which creates its own band structure. This manifests as anti-crossing points in the band structure and the group velocity vanishes at these points. If sufficient gain is achieved, lasing may occur at the anti-crossing points.

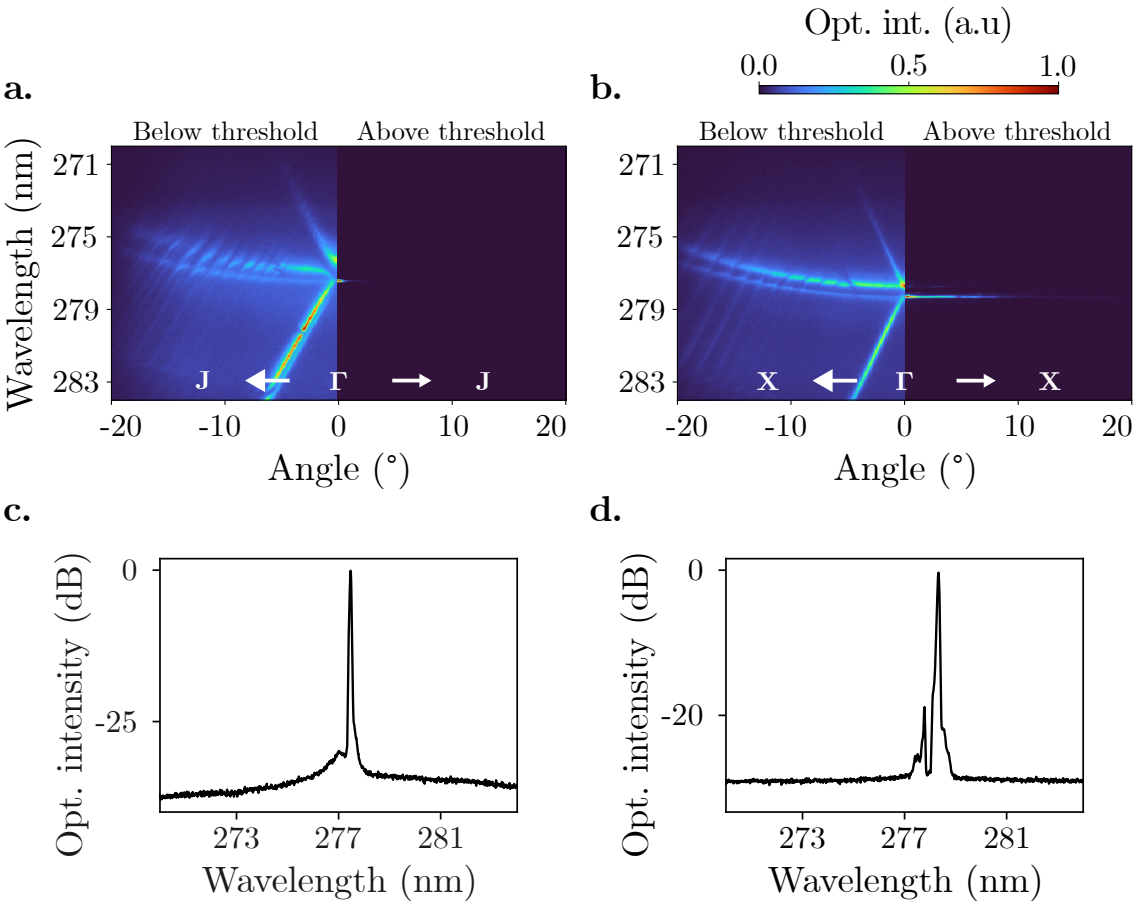


Figure 4.9: Measured band structures of **a.** the H-PCSEL and **b.** the S-PCSEL. The left panels show below-threshold (∼0.7 ×threshold) and the right panels show above-threshold (∼2 ×threshold) band structures. Emission spectra at ∼2 ×threshold for **c.** the H-PCSEL and **d.** the S-PCSEL.

When pumped above threshold, both PCSELs show non-dispersive lasing peaks. Figures 4.9a and 4.9b show the below- and above-threshold band structure measurements of the H-PCSEL and the S-PCSEL, along the Γ-J and Γ-X directions. The left-hand side of both figures shows below-threshold measurements and the right-hand side of the figures shows above-threshold measurements. For the H-PCSEL, the lasing peak appears close to the B_1, B_2 and C modes. In the S-PCSEL case, lasing occurs close to the A and B modes and has a much higher beam divergence. However, identifying the lasing mode is challenging because the band-edge modes at the Γ-point are spectrally close, making it difficult to resolve individual modes. Corresponding spectra (∼2 × threshold) of both devices are given in Figures 4.9c and 4.9d. The H-PCSEL ex-

hibits a single lasing peak at 277.5 nm with a linewidth of 91 pm. The S-PCSEL, on the other hand, exhibits multiple lasing peaks, indicating multimode lasing. The strongest lasing peak is positioned at 278.3 nm with a linewidth of 93 pm.

4.3.3 Near-field and far-field emission patterns

Figure 4.10 shows the near-field patterns of the H-PCSEL and the S-PCSEL measured at ∼2 × threshold, respectively. The H-PCSEL shows stronger outcoupling near the center of the photonic crystal area. However, in an infinite photonic crystal, the modes are symmetry-protected due to the symmetry of circular holes therefore do not radiate. At finite sizes, the edges of the photonic crystal break the symmetry of the field distribution, allowing the modes to radiate vertically. Therefore, the radiation rate increases toward the edge of the photonic crystal [150]. The observed stronger central outcoupling in the H-PCSEL may therefore be caused by non-uniformities introduced by epitaxial growth and/or fabrication, which break the symmetry and enable outcoupling. In the S-PCSEL case, the outcoupling seems strongest near the edge of the photonic crystal.

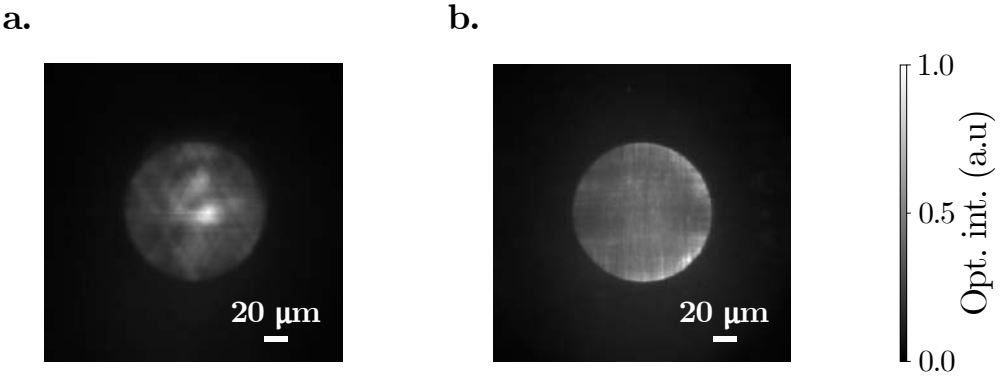


Figure 4.10: Near-field images of **a.** the H-PCSEL and **b.** the S-PCSEL measured at ∼2 × threshold.

Figure 4.11 shows the far-field emission patterns of the H-PCSEL and the S-PCSEL measured below threshold (0.7 ×) and above threshold (∼2 ×). Below threshold, both devices exhibit highly divergent emissions (Figures 4.11a and 4.11b). However, unlike conventional LEDs, which typically have a Lambertian emission profile, the emission from PCSELs is still modulated by the photonic crystal. This can yield higher direc-

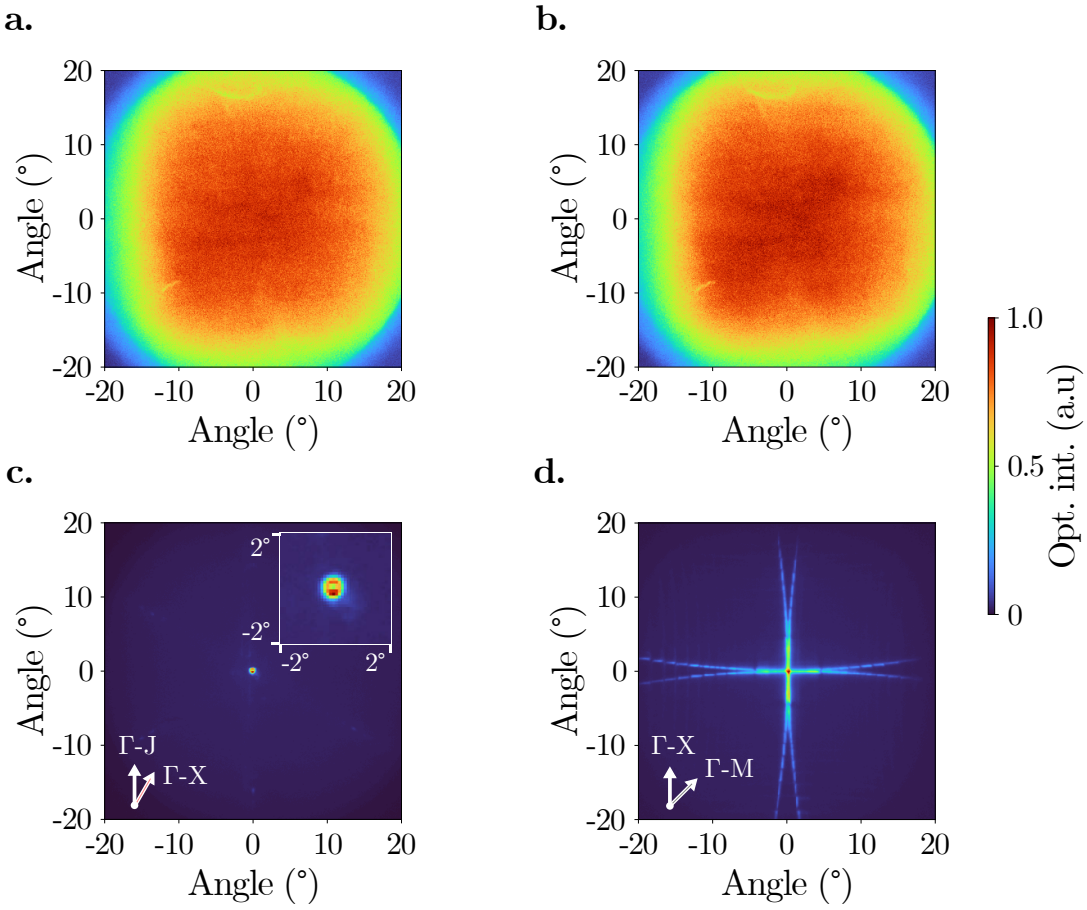


Figure 4.11: Far-field emission patterns of PCSELs: below threshold (∼0.7 ×) for **a.** the H-PCSEL, **b.** the S-PCSEL and above threshold (∼2 ×) for **c.** the H-PCSEL, **d.** the S-PCSEL.

tionality in PCSELs than in LEDs, even in the spontaneous emission regime [167].

When pumped above threshold (∼2 ×), the H-PCSEL exhibits a doughnut-shaped emission pattern with a divergence angle of less than 1°. This is because of the circular holes that result in destructive interference along the normal for modes A, B_1, B_2, and C. [125, 168]. When the symmetry is broken, it results in a single Gaussian-like emission pattern [169]. The far-field emission pattern of the S-PCSEL, on the other hand, is highly divergent, extending up to 20° in the Γ-X directions. This highly divergent emission indicates poor 2D coupling and strong 1D coupling. Thus, the 2D square lattice is acting as a 1D grating. Other fabricated PCSELs with square lattices showed similar patterns. Therefore, the following chapters and Paper A-C focus on hexagonal lattices,

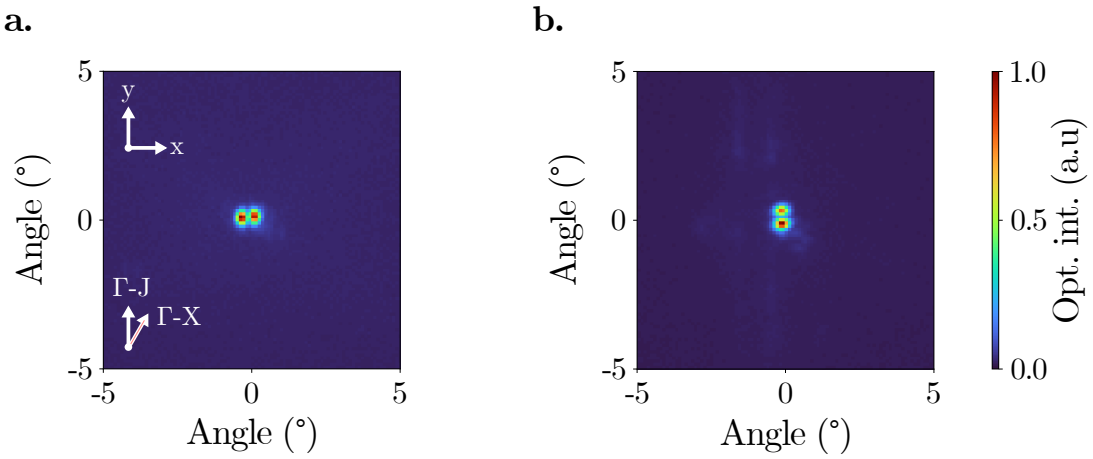


Figure 4.12: Polarization-resolved far-field emission patterns at ∼2 × threshold of the H-PCSEL: **a.** Γ-X-polarized and **b.** Γ-J-polarized.

which are better suited to achieving 2D lasing with the desired emission properties, such as a circularly symmetric beam with low divergence.

The identification of the lasing mode is challenging due to the narrow spectral spacing and broad emission of the band-edge modes at the Γ-point, which prevents them from being distinguished by wavelength alone. Each band-edge mode produces a distinct polarization-resolved far-field pattern with different numbers of intensity lobes aligned in different photonic crystal orientations, which are investigated in more detail in Paper B. To identify the lasing mode of the H-PCSEL, we performed polarization-resolved far-field measurements. Figure 4.12 shows the measured polarizations above threshold (∼2 ×) along the Γ-J and Γ-X directions. The polarizer was oriented in the x- and y-directions, which correspond to the Γ-X and Γ-J directions, respectively. The polarization measurements indicate lasing in the B_1 mode, whose orientation matches the polarization characteristics of hexagonal-lattice PCSELs, as discussed in Paper B.

4.4 Influence of Photonic Crystal Design Parameters

To understand how PCSELs work and optimize their performance, it is essential to understand how design parameters affect their characteristics. This section focuses on the influence of the etch depth, lattice

constant and FF on the band structure and lasing performance of UV-C PCSELs.

4.4.1 Effect of etch depth and lattice constant

To effectively utilize the gain that can be obtained from the QWs, the resonant wavelength must be aligned with the gain peak of the QWs. Optimizing the detuning between the optical mode and the gain peak enhances the modal gain and consequently lowers the threshold [50]. This is particularly challenging for III-nitride-based PCSELs, where the emission blue-shifts due to the QCSE at low current densities and due to the band filling at high current densities [170], driven by the high threshold carrier densities typical of Al-rich AlGaN-based laser diodes [28, 29, 36].

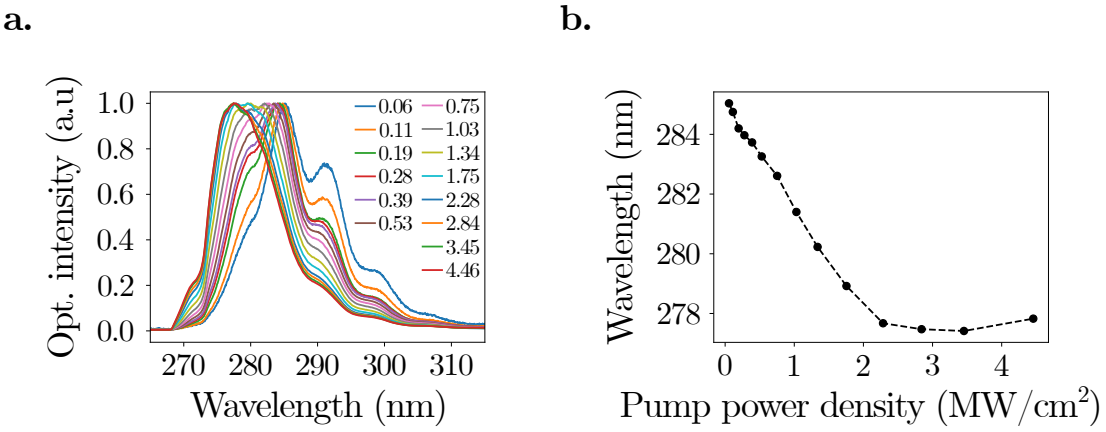


Figure 4.13: **a.** PL emission spectra of the QWs of the as-grown material measured at different pump power densities and **b.** the PL peak wavelengths as a function of pump power density.

Figure 4.13a shows the measured PL spectra of the QWs of the as-grown material at different pump power densities. At 60 kW/cm^2, the PL peak is located at 285.1 nm with a FWHM of approximately 13 nm. The peak wavelength shifts from 285.1 nm at 60 kW/cm^2 to 277.6 nm at ∼2.3 MW/cm^2 (Figure 4.13b), i.e. blue-shifts with increasing pump power density. Beyond this point, further increasing the pump power density does not affect the peak wavelength. The total blueshift within the used pump power density range is 7.5 nm. For detuning, the important PL is at the pump power densities close to the threshold. In threshold ranges (5–6 MW/cm^2) observed in the optically pumped PC-

SELs investigated in this thesis, the QCSE has already been screened and the PL does not shift. However, for devices with lower threshold, the shift might be important for detuning.

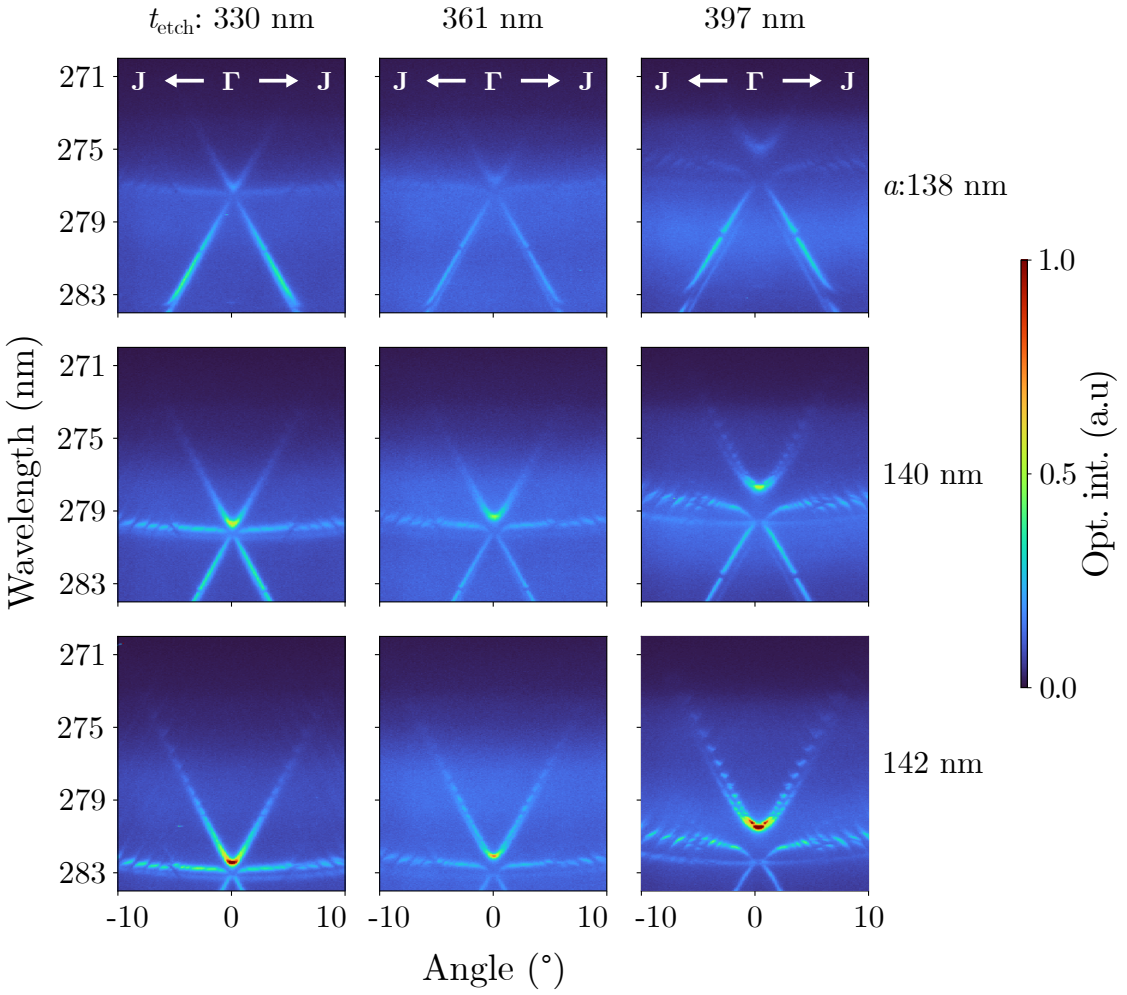


Figure 4.14: The measured band structure below threshold for PCSELs with lattice constants of 138 nm, 140 nm and 142 nm for t_{etch} values of 330 nm, 361 nm, and 397 nm.

In PCSELs, the resonant wavelength is mainly determined by the lattice constant. Figure 4.14 summarizes the below-threshold band structure of 9 PCSELs with lattice constants of 138 nm, 140 nm and 142 nm for t_{etch} values of 330 nm, 361 nm, and 397 nm, measured at 0.5 × threshold. The device with t_{etch} = 361 nm and a = 138 nm corresponds to the H-PCSEL, described earlier. All PCSELs have similar hole diameters around 98–102 nm. The bands red-shift as the lattice constant increases. The shift is approximately 1.5 nm for every nm change in the

lattice constant. Considering that the PL FWHM is about 10 nm and the gain bandwidth at the loss level of the laser is very likely even narrower, the choice of lattice constant in PCSELs is thus important. When the resonance wavelength determined by the lattice constant deviates from the gain peak, the lasing threshold can increase substantially [Paper B].

Another important design parameter is the photonic crystal hole depth. Band splitting increases as t_{etch} (and therefore t_{PC}) increases. This may be beneficial for single-mode operation as it widens modal spacing. Furthermore, the depth also influences the lasing mode selection. Figure 4.15a shows the measured band structure along the Γ-J direction below and at ∼2 × threshold for the PCSEL with t_{etch} = 397 nm and a = 138 nm shown in Figure 4.14. The PCSEL exhibits two lasing peaks in the band structure. The weaker one is at 276.8 nm near the B_1 mode and the stronger one is at 277.6 nm in the A mode. This is in contrast to the H-PCSEL discussed in Sections 4.2 and 4.3, which has the same lattice constant and hole diameter but a shallower etch depth, where only a single lasing peak was observed in the B_1 mode. Similar lasing mode switching between band-edge modes for different photonic crystal etch depths has been reported in double square-lattice PCSELs [171]. One possible explanation for lasing in the A mode is that the deeper etching increases the effective hole size that the optical mode interacts with. Figure 4.15a shows the far-field emission pattern measured at ∼2 × threshold. The PCSEL displays a highly divergent pattern with branches in the Γ-J direction extending >10°. Similar patterns have been reported previously when lasing occurs in the A mode [Paper A, 172].

4.4.2 Effect of filling factor

The FF of the photonic crystal in PCSELs strongly influences coupling and mode selection, as discussed in more detail in Paper A. Figure 4.16 presents top-view SEM images of two fabricated PCSELs with FF values of 10% and 24%. The PCSELs were fabricated using the epitaxial material with d_{AlN} = 100 nm and an etch depth (t_{etch}) of 70 nm. A thin top AlN cladding layer (100 nm instead of 320 nm) and shallow photonic crystal etching enable precise control of the FF.

Figures 4.17a and 4.17c display the band structure measurements below and above threshold for two different fill factors, respectively. For FF = 10%, the lasing mode is close to the B_1, B_2 and C modes, whereas for FF = 24%, the lasing mode appears in the A mode. The different FFs

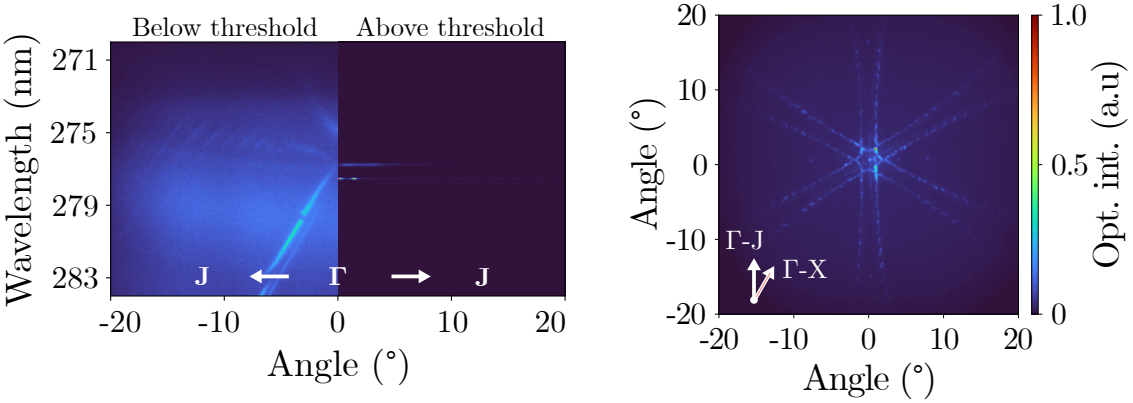


Figure 4.15: a. Below- and above-threshold (∼2 ×) band structure measurements of PCSEL (t_{etch} = 397 nm, a = 138 nm) along the Γ-J direction and **b.** far-field emission pattern (∼2 × threshold).

also result in distinct far-field emission patterns. Both devices display divergent emissions with three dual branches in the Γ-J directions (Figure 4.17b and 4.17d). However, in the 10% FF case, the dual branches are closer together in angle compared to the 24% FF case. This emission pattern resembles that of the S-PCSEL (see Figure 4.11d), where two orthogonal dual branches appear due to the four-fold symmetry. In addition, in the other investigated PCSELs with similar FF ∼10%, some devices displayed only one of the three branches, and some displayed two of the three branches. This indicates dominant 1D coupling for the low FF regime and mode competition between the oscillations in different Γ-J directions [Paper A]. In the 24% FF case, the far-field emission pattern is identical to that of the deeply etched photonic crystals in Figure 4.15b,

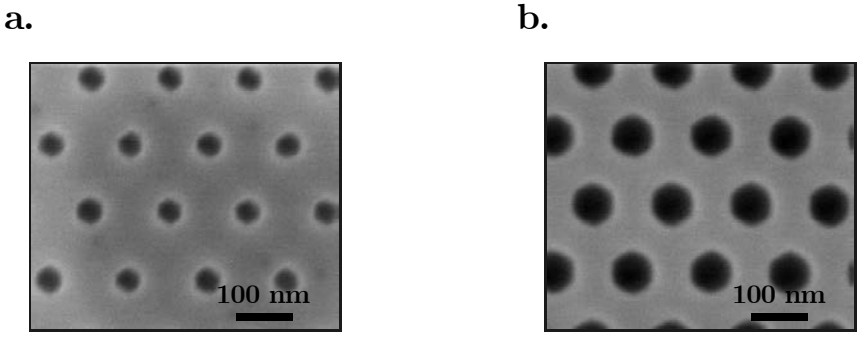


Figure 4.16: Top-view SEM images of PCSELs with **a.** 10% FF and **b.** 24% FF.

where the lasing is observed in the A mode. The lasing in the A-mode at 24% FF can be explained by its decreasing lateral losses with increasing FF, combined with its low vertical losses [Paper A]. At the same time, the vertical losses of other band-edge modes increase with FF, making them less favorable. The increase in the 2D coupling constants (κ_1 and κ_2) can further promote this (Figure 3.10b).

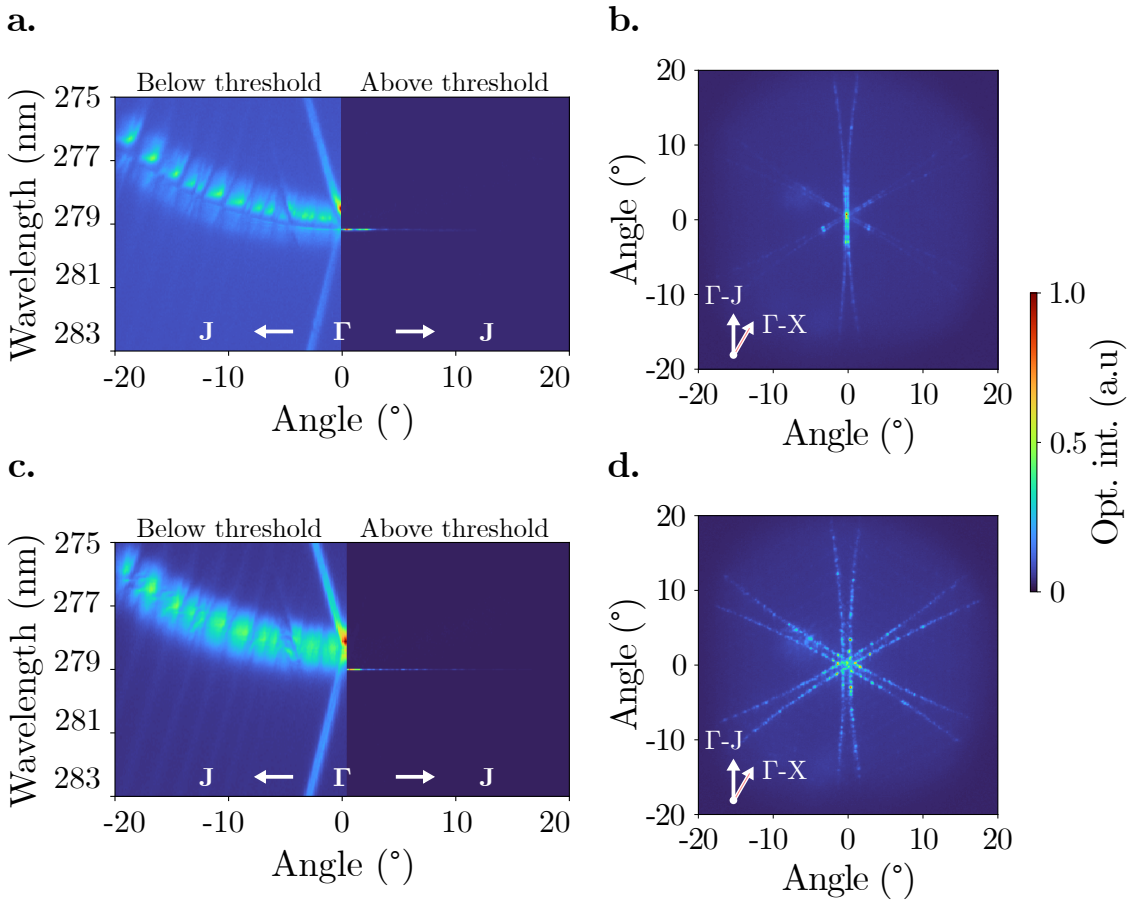


Figure 4.17: Below- and above-threshold (∼2 ×) band structure measurements of PCSELs (d_{AlN}=100 nm, t_{etch}=70 nm, a=140 nm) with **a.** 10% FF and **c.** 24% FF along the Γ-J direction. Far-field emission patterns for **b.** 10% FF and **d.** 24% FF.

Although the coupling constant simulations support 2D oscillation dominance, they don't provide sufficient information for low FF (∼10%) regimes. To confirm the 1D oscillation domination for the PCSELs with low FFs, we fabricated two orthogonal 1D gratings with a periodicity of 120 nm and a duty cycle of 55%, as shown in Figure 4.18a and 4.18b. Figures 4.18c and 4.18d show the far-field emission pattern of the

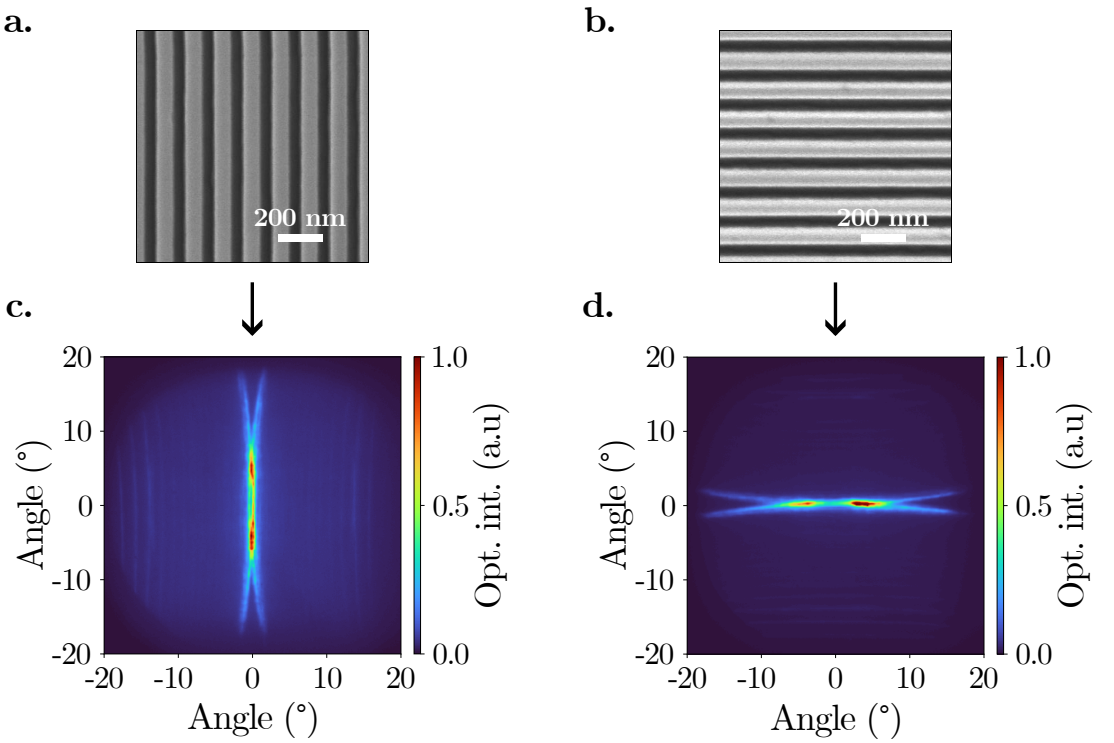


Figure 4.18: **a.**, **c.** SEM images and **b.**, **d.** above threshold far-field emission patterns of two orthogonal 1D gratings with a periodicity of 120 nm.

1D gratings above threshold. Each grating produces a highly divergent emission pattern that extends to higher angles in the direction orthogonal to its grating vector. In the direction parallel to the grating vector, the divergence angle is ∼1°. This is because the grating only allows a discrete k vector along its periodicity, while in other directions it is unrestricted, which results in emission over a broader range of angles. The far fields for the 1D gratings are identical to that of the PCSEL shown in Figure 4.17b, except that the PCSEL produces three patterns due to its six-fold symmetry of the hexagonal lattice used. This suggests that the 2D photonic crystal acts as a 1D grating for low FFs and therefore produces patterns similar to 1D gratings.

Chapter 5

Towards Electrically-Driven UV-C Photonic-Crystal Surface-Emitting Lasers

We have demonstrated the first UV-C PCSELs under optical pumping at room temperature. As with most semiconductor lasers, the ultimate goal is to achieve lasing under current injection. This goal, however, is challenging due to fabrication difficulties, small feature sizes required due to the short operating wavelengths and current material limitations. These constraints make it necessary to use a different design and fabrication approach for UV-C PCSELs compared to long-wavelength PCSELs.

5.1 Challenges for Electrically Driven UV-C PCSELs

Most PCSELs operating at longer wavelengths (e.g., visible and infrared) utilize the regrowth approach, in which the photonic crystal is first etched, and subsequent layers including the active region with QWs are then grown. This is generally enabled by optimized growth conditions, low band gaps, and mature materials technology, resulting in high electrical conductivity and low dislocation density. In contrast, regrowth of Al-rich AlGaN has been challenging and may result in defect formation and cracking [173–175].

UV-C devices require Al-rich (>60% Al) AlGaN for optical transparency and are typically grown on AlN templates on sapphire or on bulk

AlN substrates. Both substrate options are currently non-conductive, which requires placing the p- and n-contacts on the same side. In contrast, GaAs- or InP-based PCSELs use thick, conductive substrates [122, 176] that allow a bottom-side contact, which leads to a better current distribution through current spreading in the substrate.

In AlGaN devices, the substrate can be removed using methods such as laser lift-off [177,178], water lift-off [179,180] and electrochemical etching [40, 181]. Removing the substrate provides access to the electrically conductive n-layer, which would allow the contacts to be placed on the N-polar side and allow for a more vertical current injection and thereby potentially improve current spreading. However, removing the substrate may cause the released membrane to bow due to relaxation of the strain in the material. The effect of this bowing on PCSEL performance at the UV-C wavelengths is currently unclear. In addition, even with substrate removal, the current still needs to be spread in a thin Al-rich layer and both sides cannot be fully metalized, as this would prevent surface emission. A potential solution would be to employ metal finger contacts on the N-polar side, which can improve current distribution and still allow surface emission. Sputtering a conductive AlGaN layer [182] onto the released membrane to increase its thickness, combined with N-polar contacts, would further enhance current spreading. In addition, substrate removal opens up another possibility: the photonic crystal could be etched directly on the exposed N-polar surface of the released membrane. However, etching the photonic crystal on the n-side exposes a different crystal polarity. This introduces different dry-etching characteristics, surface properties and fabrication challenges.

In the regrowth-free approach we employed, the p-side is fully metalized and the n-contact is placed in the surrounding area next to the device. This design serves two purposes: i) improved current distribution on the p-side, where the conductivity is significantly lower compared to the n-side; ii) eliminating the need for substrate removal. To achieve decent photonic crystal confinement, the holes need to be sufficiently close to the optical mode, i.e., to the waveguide core. On the other hand, the p-metal layer on top of the photonic crystal must be far enough away from the mode to not cause too high optical absorption losses. Therefore, the photonic crystal holes must be etched deep enough, i.e., to the waveguide core. On the other hand, the p-metal layer on top of the photonic crystal must be far enough away from the mode to not cause too high optical absorption losses. Thus, the photonic crystal holes must

be etched deep enough. Care must be taken such that the metal, when deposited, does not go too deep into the photonic crystal holes, since this will increase optical absorption. One solution is to fill the holes with a dielectric material, which would prevent the metal from reaching into the holes. This approach, however, requires an etch-back step to allow a metal contact to be placed on the p-surface. In addition, since dielectric materials have a higher refractive index than vacuum/air, the optical mode may extend further toward the metal contact if the holes are filled with a dielectric. This might be helpful for a higher Γ_{PC}, but may increase absorption losses due to the mode getting closer to the metal. Therefore, an even deeper photonic crystal etching may be required unless the dielectric only closes the holes without completely filling them, thus leaving a small air hole at the bottom of the hole. Alternatively, tilted metal evaporation can be used to prevent metal deposition into the holes.

In terms of electrical characteristics, the p- and n-sides present different difficulties. On the p-side, in addition to the decrease in the current injection area and the resulting increase in series resistance, the photonic crystal etching may induce damage to the p-side and degrade the conductivity, leading to an additional voltage drop or even non-conductive material. On the n-side, placing the contact around the device area means that the current needs to be spread in a thin n-doped epitaxial layer, which will result in nonuniform current distribution across the device area if the device area is large.

5.2 Etch-Induced Damage to p-Side Conductivity

So far, electrically driven AlGaN-based EELs at UV-C wavelengths have been demonstrated only with a DPD layer. A limited number of studies focusing on UV-C devices with a DPD layer have been conducted so far and the effects of etching a photonic crystal into a DPD layer have not been explored. To investigate how much the electrical characteristics are affected by etching into a DPD on the p-side, we fabricated UV-C LEDs with and without photonic crystals etched into the DPD.

5.2.1 Device structure and fabrication

The epitaxial layers were grown on a double-growth-annealing (DGA) AlN/sapphire template. Table 5.1 shows the epitaxial layers used to investigate the effect of etch-induced damage to the p-side, and Figure 5.1 shows the process flow to fabricate electrically driven structures with and without a photonic crystal etched into the DPD.

Table 5.1: Epitaxial layers showing composition (x), thickness (d), and description.

Layer	x (%)	d (nm)	Description
GaN:Mg	0	50	Cap
$Al_xGa_{1-x}N \rightarrow GaN$	$80 \rightarrow 0$	5	Transition
$AlN \rightarrow Al_xGa_{1-x}N$	$100 \rightarrow 80$	320	DPD
AlN	100	2	Electron blocking layer
$Al_xGa_{1-x}N$	63	50	Last barrier
$Al_xGa_{1-x}N$	50	4.5	QW
$Al_xGa_{1-x}N$:Si	63	5	Barrier
$Al_xGa_{1-x}N$	50	4.5	QW
$Al_xGa_{1-x}N$:Si	63	50	First barrier
$Al_xGa_{1-x}N$:Si	76	800	n-side current-spreading layer
$Al_xGa_{1-x}N$	76	100	Buffer
$AlN \rightarrow Al_xGa_{1-x}N$	$100 \rightarrow 76$	25	Buffer transition
AlN	100	400	Smooth buffer
DGA AlN/sapphire	–	–	–

The process flow starts with dry etching of the epitaxial layers to a depth of approximately 600 nm using a $Cl_2/SiCl_4/N_2$ plasma to access the n-doped layer for the n-contact. Following the etching, the sample was dipped in BOE for 1 minute to remove surface oxides. Immediately after the BOE dip, the sample was transferred to the e-beam evaporator chamber for n-metal deposition. An n-metal stack consisting of V/Al/Ni/Au with thicknesses of 15/90/20/30 nm was deposited. The n-contacts were annealed at 900°C for 1 minute in N_2 ambient. For the photonic crystal etching, we used a different approach compared to the optically pumped UV-C PCSEL fabrication. Here, a ∼90-nm-thick SiO_2 layer was first deposited by sputtering. A positive e-beam resist ARP was spun onto the sample and baked for 5 minutes at 180°C. To increase the adhesion of the resist to SiO_2, the sample was coated with an adhesion promoter, hexamethyldisilazane (HMDS), prior to resist spinning.

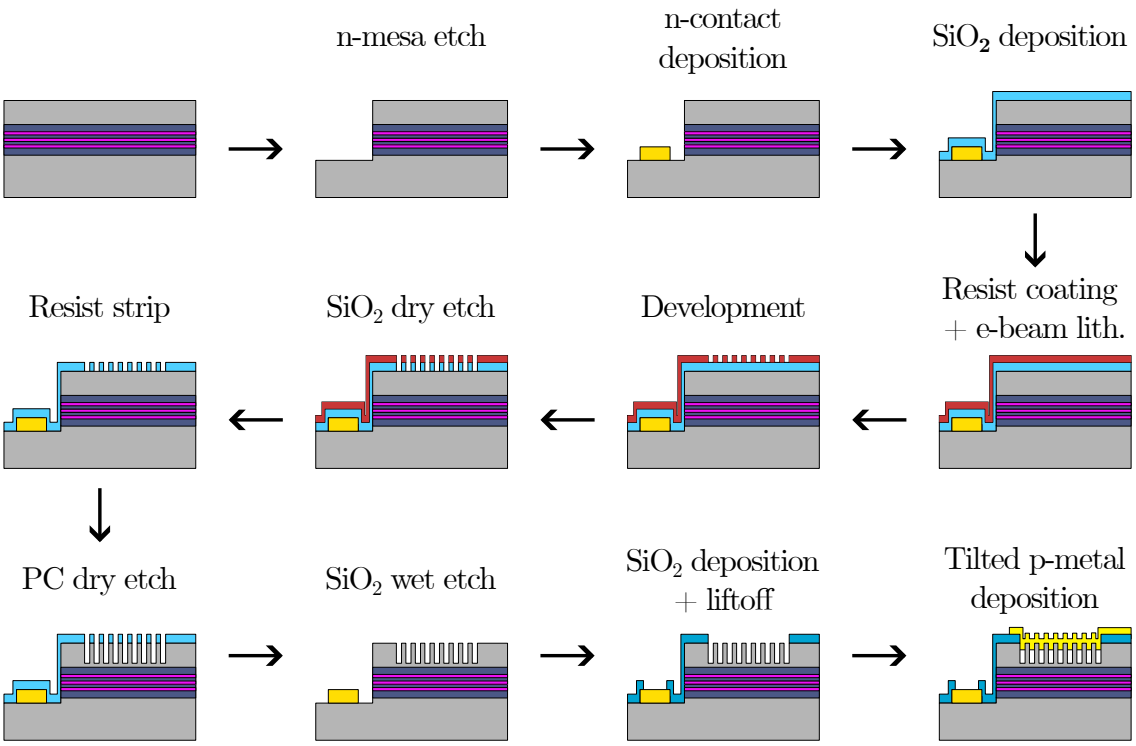


Figure 5.1: Process flow of electrically driven UV-C LEDs with photonic crystals.

In the last step of resist coating, a conductive polymer, Espacer, was spin-coated to prevent charging during e-beam exposure. A hexagonal lattice of circular holes with hole diameters 64 nm and 95 nm, lattice constants of 125 nm, 250 nm, 500 nm and 1000 nm, and device diameters of 40 μm, 100 μm and 200 μm were exposed using electron-beam lithography. The values of these parameters are summarized in Table 5.2. After the exposure, the Espacer layer was removed by dipping in deionized water for 20 seconds. The resist was then developed for 90 seconds in n-amyl acetate. After the development, the photonic crystal patterns were transferred into the SiO_2 layer by dry etching using CH_4/CHF_3 plasma. The photonic crystal patterns in the SiO_2 layer were subsequently transferred into the epitaxial material using Cl_2/Ar plasma etching to a depth of about 250 nm using the same conditions as for the optically pumped UV-C PCSEL photonic crystal etching step. The remaining SiO_2 was removed with BOE. For passivation, another 100-nm-thick SiO_2 layer was deposited by e-beam evaporation. The p-contact areas were opened by lift-off. Opening the contact area by lift-off rather than selective wet

or dry etching of SiO_2 ensured no SiO_2 was left in the holes. Finally, a p-metal stack consisting of 30-nm-thick Ni and 300-nm-thick Au was deposited at a 45° angle using e-beam evaporation. The sample was rotated at 5 rpm during the deposition. The tilted evaporation was performed to prevent the metal from going too deep into the holes. The p-contacts were annealed at 500°C for 5 minutes. An optical microscope image of the final devices after p-contact annealing is shown in Figure 5.2.

Table 5.2: Parameter values for the fabricated UV-C LEDs with a hexagonal lattice. Hole diameters correspond to the diameter of the fabricated circular air holes at the top of the photonic crystal after etching.

Parameter	Values
Device diameter, L (μm)	40, 100, 200
Lattice constant, a (nm)	125, 250, 500, 1000
Hole diameter, ϕ (nm)	64, 95

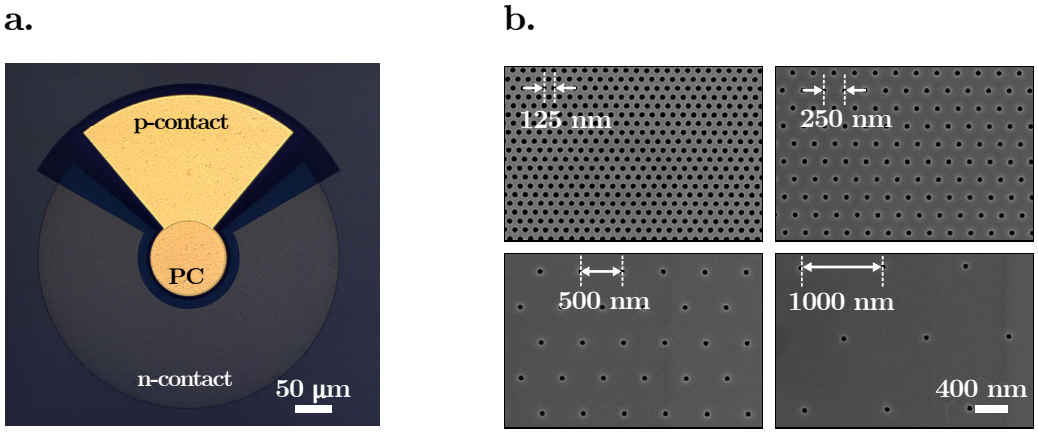


Figure 5.2: **a.** Optical microscope image of an electrically driven UV-C LED with a photonic crystal after fabrication. **b.** Top-view SEM images of photonic crystals with lattice constants of 125 nm, 250 nm, 500 nm and 1000 nm.

5.2.2 Characterization

Figure 5.3 summarizes the CW JV curves measured at room temperature. The JV characteristics are similar for the LEDs with/without a photonic crystal when a is equal to 500 nm or 1000 nm, regardless of hole diameter or device size, since the comparison is based on current density rather than total current. Note that the LEDs with a photonic

crystal having a lattice constant of $a = 125$ nm and a hole diameter of $\phi = 95$ nm could not be successfully processed because the lithography step failed and the patterns were not properly transferred. The voltage range is 8–10 V at a current density of 20 A/cm^2. For such large lattice constants, the FF is only between 0.3% and 3.2%. For these small values of FF, the photonic crystal etching does not significantly affect the p-layer conductivity, and the operating voltage does not change. When a is reduced to 250 nm, the operating voltage of the photonic crystal LEDs is still similar to that of the reference LEDs for a hole diameter of $\phi = 64$ nm ($FF = 6\%$). However, when $\phi = 95$ nm (corresponding to an FF of 13%), the operating voltage increases by approximately 0.6 V at a current density of 20 A/cm^2. For $a = 125$ nm ($FF = 24\%$), the operating voltage increases even more, by about 2.2 V at the same current density. These results indicate that small lattice constants (i.e., small a) and large air holes (i.e., large FF) increase the series resistance of the p-side.

Considering the lattice constant range required for UV-C wavelengths (a<140 nm) and an FF of approximately 10% for sufficient 2D coupling, electrically driven UV-C PCSELs are expected to experience a voltage penalty due to increased series resistance. In addition, etching deeper holes to achieve a higher Γ_{PC} may further increase series resistance and the operating voltage. This is just an initial study on the plasma-induced damage on DPD layers, and more experiments are needed to understand how the resistance and operating voltage are affected by the decreased cross-sectional area, degradation in the DPD due to plasma damage, such as trap formation, sidewall damage, depletion regions, local polarization field and hole density changes.

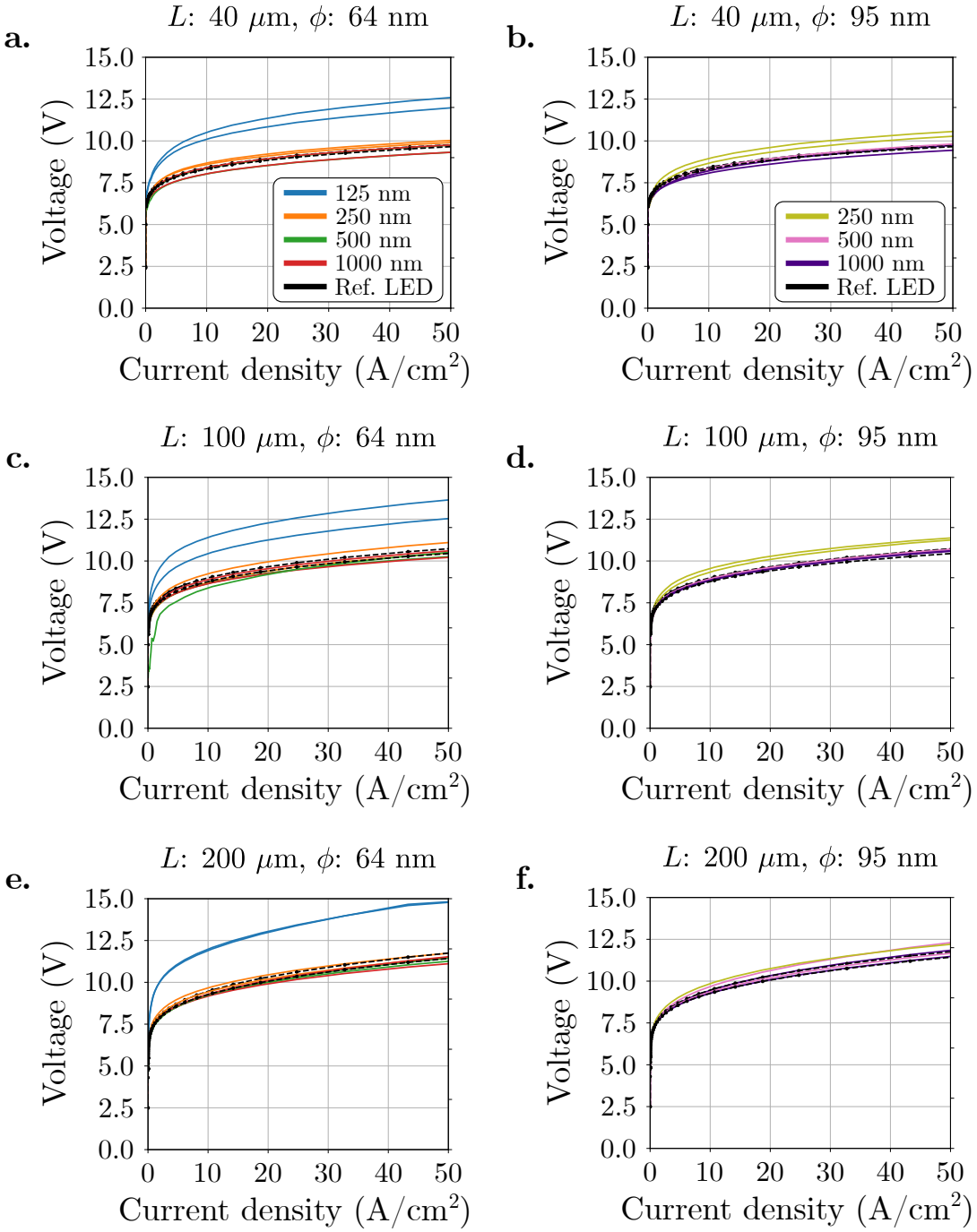


Figure 5.3: CW JV curves of UV-C LEDs with photonic crystal diameters of 40 μm (**a.** $\phi = 64$ nm, **b.** $\phi = 95$ nm), 100 μm (**c.** $\phi = 64$ nm, **d.** $\phi = 95$ nm) and 200 μm (**e.** $\phi = 64$ nm, **f.** $\phi = 95$ nm) measured at room temperature. Black curves show the reference LEDs without a photonic crystal.

5.3 Lateral Current Spreading on n-Side

5.3.1 Ring-shaped geometry to reduce current spreading distance

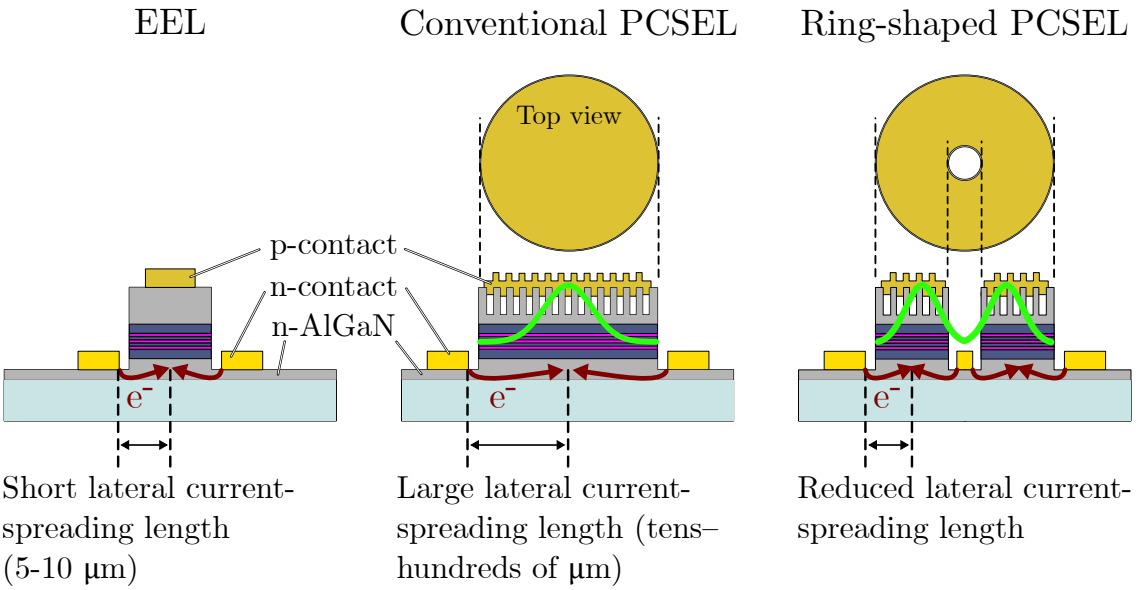


Figure 5.4: Comparison of lateral current spreading distances in an EEL (left), a conventional PCSEL (middle) and a ring-shaped PCSEL (right). The green curves indicate the representative intensity envelope of the expected lasing mode.

Figure 5.4 illustrates the comparison of the lateral current spreading distance in EELs and conventional PCSELs. In EELs, the lateral current spreading distance is on the order of 5–10 μm [36], whereas in PCSELs, it can range from tens to hundreds of micrometers due to the large lateral extension of the device (which is needed to reduce lateral optical losses). Current UV-C laser technology mostly relies on non-conductive substrates. Without a thick conductive substrate, the injected current must be distributed laterally in the epitaxial layers across the device area. On the n-side, AlGaN with an Al content above 60% can typically be grown only to a limited thickness before cracking or defect formation occurs [173], which limits the achievable conductivity and increases resistance. This high resistance can lead to a nonuniform current distribution across the device, which in turn can result in a nonuniform gain profile and variations in refractive index. These can increase the lasing

threshold and potentially promote higher-order modes [139, 183].

To address these challenges, we introduce a ring-shaped PCSEL geometry [Paper C], in which a circular area is removed from the center to accommodate an additional contact (see Figure 5.4). The ring-shaped approach reduces lateral current spreading distance by 50% and thereby offers improved current uniformity.

The ring-shaped PCSEL concept is based on the assumption of a mode that has zero intensity in the center of the device and thus is not affected by an etched hole placed there. The W-mode is one such mode; see the green curve in Figure 5.4 (right) that has been predicted in PCSELs [147], which is a combination of the B_1 and B_2 modes of an infinitely large PCSEL. The other band-edge modes (A, B_1, B_2, C, D_1, and D_2) exhibit a Gaussian-like intensity envelope, with maximum intensity in the center of the PCSEL and will thus be strongly affected by an etched hole in the center. We test this approach experimentally and validate its feasibility using optically pumped ring-shaped PCSELs

5.3.2 Device structure and fabrication

The ring-shaped PCSELs were fabricated using the same epitaxial material as used for the H-PCSEL and the S-PCSEL shown in Chapter 4. Fabrication started with the definition of the ring-shaped circular mesas in HSQ by electron-beam lithography, followed by resist development with the salty developer. The areas in the central region and outside the mesas were then dry-etched to a depth of 315 nm using Cl_2/Ar plasma under the same etching conditions as previously used for optically pumped PCSELs. Following this etching, the remaining HSQ was removed with BOE. A hexagonal lattice of circular holes (a = 138 nm) was patterned on the circular mesas with a new layer of HSQ using electron-beam lithography. After development, the photonic crystals were dry-etched into the mesas to a depth of ∼285 nm. In the photonic crystal etching step, the areas in the center and outside the mesas were also etched, resulting in a total mesa height of approximately 600 nm. This depth ensures that the inner etched area reaches the bottom cladding, which is needed to electrically contact this region in future electrically driven PCSELs.

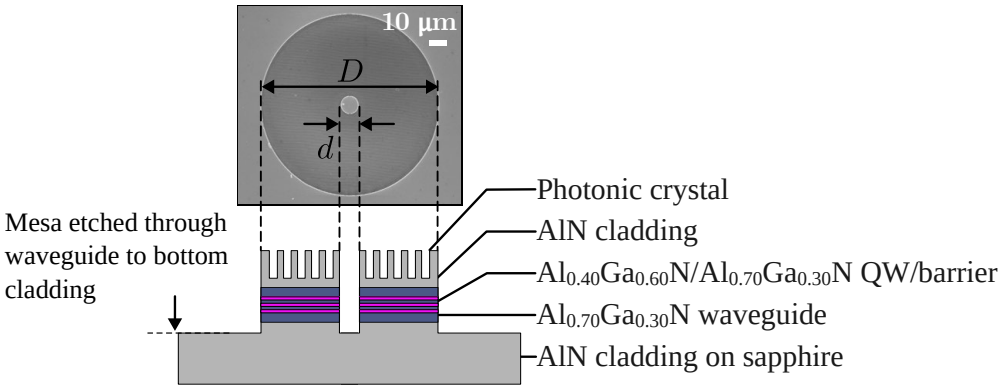


Figure 5.5: Schematic of optically pumped ring-shaped UV-C PCSELs with an outer diameter D and an inner diameter d. The top-view SEM image shows a ring-shaped PCSEL with $D = 100$ μm and $d = 0.1D$.

The ring-shaped PCSELs have an outer diameter D and an inner diameter d, which is defined as a fixed fraction of the outer diameter D (e.g., $d = 0.1D$). When $d = 0$, it represents a conventional PCSEL where the inner area is not etched. Figure 5.5 shows the schematic of the ring-shaped PCSELs and the top-view SEM image of a ring-shaped PCSEL ($D = 100$ μm, $d = 0.1D$) after the photonic crystal etching and resist removal.

5.3.3 Characterization

The ring-shaped PCSELs were optically pumped at room temperature with a pump beam spot size of 176 × 118 μm^2 at FWHM. Figure 5.6 shows the output intensity as a function of pump power density for 100-μm conventional PCSELs ($d = 0$) and ring-shaped PCSELs with $d = 0$, $0.05D$, $0.10D$, $0.20D$ and $0.30D$. The conventional PCSEL exhibits a lasing threshold around 5 MW/cm^2. For the ring-shaped PCSELs with $d = 0.05D$ the threshold is slightly higher, about 5.5 MW/cm^2. However, when $d = 0.10D$, the threshold is again about ∼5 MW/cm^2. This suggests that up to $d = 0.10D$, the presence of the etched area does not significantly affect the threshold, indicating that ring-shaped PCSELs with certain inner hole sizes do not suffer from optical losses due to the etched area. When $d = 0.20D$, the threshold increases to 8 MW/cm^2, and when $d = 0.30D$, the threshold is ∼11 MW/cm^2, which is more than twice the threshold observed in the conventional PCSEL, indicating a rapid increase in threshold with increasing inner diameter d.

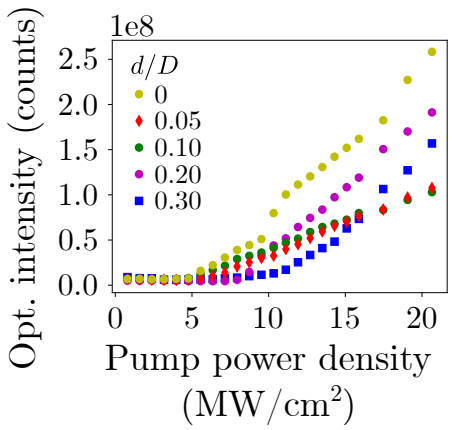


Figure 5.6: Output intensity as a function of pump power density for ring-shaped PCSELs with $D = 100$ μm and different inner diameters d.

In terms of optical performance, the ring-shaped PCSEL exhibits low divergence angles $<1°$, as shown in Paper C. Therefore, the ring-shaped geometry offers an alternative design choice for future electrically driven UV-C PCSELs since it reduces the lateral current spreading distance by about 50%.

Chapter 6

Summary and Outlook

In this thesis, we have demonstrated the first UV-C PCSELs operating at room temperature under pulsed optical pumping. The fabrication relies on a regrowth-free method where the photonic crystals with hexagonal and square lattices are directly etched into the top cladding layer. This approach is compatible with the epitaxial structures used in existing UV-C EELs.

The photonic crystal design parameters, such as filling factor, lattice constant and etch depth, influence the lasing mode, mode-gain overlap and 1D-2D coupling strength, and therefore the overall device performance. Optimization of these parameters is critical, as non-optimal values can lead to highly divergent far-field emission or a higher lasing threshold. Paper A provides a detailed investigation of the effect of filling factor and identifies the lasing mode by estimating vertical and lateral losses, and Paper B studies the effects of photonic crystal size and lattice constant, aiming to achieve low-threshold operation while maintaining low divergence angles, which will be essential in electrically driven devices. Here, we also introduce a more sophisticated method to identify the lasing mode, namely polarization-resolved far-field measurements.

Although the regrowth-free approach is directly applicable to an EEL structure, several challenges must be addressed on the path toward electrical injection. Al-rich AlGaN materials have low electrical conductivity, and etching a photonic crystal into the top cladding further degrades the electrical properties of the p-side, where current UV-C EELs employ a DPD layer. The etching process introduces a voltage penalty that increases with decreasing lattice constant, and deeper etching to achieve better photonic crystal confinement may worsen this problem. More

work is required to develop designs and etch processes that minimize the etch-induced damage.

In addition, currently available substrates are non-conductive, meaning the n-contact needs to be placed on the epitaxial side of the wafer on an area that is etched down to access the n-AlGaN layer. Paper C addresses this issue by introducing a ring-shaped PCSEL concept, where a central area is etched to reduce the current spreading distance by about 50%. However, this may limit the scalability of single-mode devices, as the ring-shaped PCSEL relies on modes with an annular intensity envelope, which may not offer the same flexibility. For example, state-of-the-art PCSELs in the blue and infrared regions use a square double lattice to engineer coupling strength, enhance modal discrimination, and therefore allow scaling the device size. It is currently an open question whether the ring-shaped PCSEL concept would allow such strategies.

An alternative solution that avoids compromising the flexibility to tailor the lattice is to remove the substrate. Accessing the backside of the device with this method enables a contact geometry with fingers reaching the device center to improve current uniformity, as is done in large-area GaAs-PCSELs. This would help with the current uniformity without etching a hole in the center as in the ring-shaped approach. Another possibility to reduce resistivity and improve current uniformity is to use a thicker current-spreading layer, though this is currently strain-limited in doped Al-rich AlGaN. An electrically conductive and UV-C-transparent substrate would bypass these challenges, as it has in other material systems, such as GaAs and InP. Addressing the electrical and architectural bottlenecks will be essential for future electrically driven UV-C PCSELs.

Chapter 7

Summary of Papers

Paper A

Deep-UV photonic crystal surface-emitting lasers,
Laser & Photonics Reviews, 20, e00271, 2026.

In this paper, we demonstrate the first deep-UV photonic crystal surface-emitting lasers operating under pulsed optical pumping at room temperature. We analyzed the effect of the filling factor and showed that it affects the lasing mode selection and the far field emission pattern. Low filling factors (10%) resulted in lasing through 1D oscillations, whereas large filling factors (22%) yielded a high 2D coupling rate but a lasing mode that is highly divergent ($>10°$). Filling factors about 15% resulted in 2D coupling and a doughnut-shaped emission pattern with a divergence angle of $<1°$. We also estimated the lateral and vertical losses using the k-space-weighted loss estimation method.

My contributions: I designed the photonic crystals, prepared the layout, developed the process to fabricate the photonic crystals, and fabricated the PCSELs in the cleanroom. I performed the characterization of all PCSELs and analyzed the data. I wrote most of the manuscript and relevant parts of the supplementary information, and incorporated feedback from the co-authors.

Paper B

Influence of photonic crystal size and lattice constant on the lasing performance of UV-C PCSELs,
ACS Photonics, accepted for publication, 2026.

UV-C PCSELs with photonic crystals etched deep enough for future electrically driven devices are demonstrated. How the lasing characteristics in optically pumped devices depend on design parameters, such as the photonic crystal lattice constant and photonic crystal size, is investigated through experiments and simulations. It is shown that the PCSELs are very sensitive to the lattice constant, where only a narrow range from 137 to 140 nm results in low-threshold devices. Also, the PCSEL size influences the threshold, which increases drastically for PCSELs $<$70 μm. Finally, the origin of high-angle lasing modes and how they can be suppressed by a small PCSEL size is explained. For a device size around 70–90 μm in diameter, both a low-divergence far-field emission and a relatively low threshold can be achieved. Our findings provide a deeper understanding of UV-C PCSELs and pave the way for the development of future electrically driven high-power light sources.

My contributions: I designed the photonic crystals, prepared the layout and fabricated the PCSELs, and characterized the photonic crystal. I performed all PCSEL characterization, including measuring thresholds, band structures and polarization-resolved far-fields. I wrote the manuscript and the relevant parts of the supplementary information, and implemented the feedback from the co-authors.

Paper C

Ring-shaped UV-C photonic-crystal surface-emitting lasers, submitted.

A big challenge in the realization of electrically injected PCSELs is the low electrical conductivity of Al-rich III-nitride materials that limits the current spreading in laterally large-sized PCSELs. Decreasing the current spreading distance without degrading the optical properties is essential for electrically injected lasers. Here, we introduce the ring-shaped PCSEL concept, where a circular area is etched away in the center to provide additional contact area and reduce the lateral current-spreading distance by ∼50%. The ring-shaped PCSELs rely on optical modes with an annular intensity profile. Therefore, they do not experience much increased optical losses due to the etched area. We investigate lasing characteristics for different inner and outer photonic crystal diameters under optical pumping to validate this ring-PCSEL concept. Modal losses, and thereby threshold, increase with decreasing outer diameter and increasing inner diameter of the photonic crystal. For outer photonic crystal diameters larger than 80 μm and inner photonic crystal diameters smaller than 20% of the outer diameter ($<$ 16 μm), the ring-shaped PCSELs exhibit divergence angles below 1° and thresholds comparable to conventional disk-shaped PCSELs. The ring-shaped PCSELs thus offer a geometry that can reduce current spreading distance by ∼50% and pave the way for future electrically driven UV-C PCSELs.

My contributions: I prepared the device layout, fabricated the devices and performed the characterization. I drafted the manuscript and the relevant parts of the supplementary information, and implemented the feedback from the co-authors.

References

[1] E. Richard, O. Coddington, G. Kopp, and P. Pilewskie, "TSIS SIM level 3 solar spectral irradiance 12-hour means v14," NASA Goddard Space Flight Center, 2025.

[2] D. E. Brash, "Sunlight and the onset of skin cancer," *Trends in Genetics*, vol. 13, no. 10, pp. 410–414, 1997.

[3] W. Kowalski, *Ultraviolet Germicidal Irradiation Handbook: UVGI for Air and Surface Disinfection*. Berlin, Germany: Springer Berlin, Heidelberg, 2009, edition 1.

[4] M. Kneissl and J. Rass, *III-Nitride Ultraviolet Emitters: Technology and Applications*. Springer Cham, 2016.

[5] N. G. Reed, "The history of ultraviolet germicidal irradiation for air disinfection," *Public Health Reports*, vol. 125, no. 1, pp. 15–27, 2010.

[6] Y.-S. Wu, A. I. Osman, M. Hosny, A. M. Elgarahy, A. S. Eltaweil, D. W. Rooney, Z. Chen, N. S. Rahim, M. Sekar, S. C. B. Gopinath, N. N. I. Mat Rani, K. Batumalaie, and P.-S. Yap, "The toxicity of mercury and its chemical compounds: molecular mechanisms and environmental and human health implications: a comprehensive review," *ACS Omega*, vol. 9, no. 5, pp. 5100–5126, 2024.

[7] T.-C. Hsu, Y.-T. Teng, Y.-W. Yeh, X. Fan, K.-H. Chu, S.-H. Lin, K.-K. Yeh, P.-T. Lee, Y. Lin, Z. Chen, T. Wu, and H.-C. Kuo, "Perspectives on UVC LED: its progress and application," *Photonics*, vol. 8, no. 6, p. 196, 2021.

[8] M. Rubin, N. Newman, J. S. Chan, T. C. Fu, and J. T. Ross, "P-type gallium nitride by reactive ion-beam molecular beam epitaxy

with ion implantation, diffusion, or coevaporation of Mg," *Applied Physics Letters*, vol. 64, no. 1, pp. 64–66, 1994.

[9] H. Amano, M. Kito, K. Hiramatsu, and I. Akasaki, "P-type conduction in Mg-doped GaN treated with low-energy electron beam irradiation (LEEBI)," *Japanese Journal of Applied Physics*, vol. 28, no. 12, pp. L2112–L2114, 1989.

[10] S. Nakamura, T. Mukai, and M. Senoh, "Candela-class high-brightness InGaN/AlGaN double-heterostructure blue-light-emitting diodes," *Applied Physics Letters*, vol. 64, no. 13, pp. 1687–1689, 1994.

[11] C. Zhang, K. Jiang, X. Sun, and D. Li, "Recent progress on AlGaN-based deep ultraviolet light-emitting diodes below 250 nm," *Crystals*, vol. 12, no. 12, p. 1812, 2022.

[12] J. Lang, F. Xu, J. Wang, L. Zhang, X. Fang, Z. Zhang, X. Guo, C. Ji, C. Ji, F. Tan, Y. Wu, X. Yang, X. Kang, Z. Qin, N. Tang, X. Wang, W. Ge, and B. Shen, "Progress in performance of AlGaN-based ultraviolet light-emitting diodes," *Advanced Electronic Materials*, vol. 11, p. 2300840, 2025.

[13] H. Morkoç, *Handbook of Nitride Semiconductors and Devices, Materials Properties, Physics and Growth.* Wiley-VCH, 2009.

[14] H. Amano, R. Collazo, C. De Santi, S. Einfeldt, M. Funato, J. Glaab, S. Hagedorn, A. Hirano, H. Hirayama, and R. Ishii, "The 2020 UV emitter roadmap," *Journal of Physics D: Applied Physics*, vol. 53, no. 50, p. 503001, 2020.

[15] M. Kneissl, "Experimental nanophysics and photonics," https://www.tu.berlin/en/originagkneissl/research, accessed: 2026-02-22.

[16] Y. Taniyasu, M. Kasu, and T. Makimoto, "An aluminium nitride light-emitting diode with a wavelength of 210 nanometres," *Nature*, vol. 441, pp. 325–328, 2006.

[17] T. Bhattarai, A. Ebong, and M. Y. A. Raja, "A review of light-emitting diodes and ultraviolet light-emitting diodes and their applications," *Photonics*, vol. 11, no. 6, p. 491, 2024.

[18] E. Sharma, R. Rathi, J. Misharwal, B. Sinhmar, S. Kumari, J. Dalal, and A. Kumar, "Evolution in lithography techniques: microlithography to nanolithography," *Nanomaterials*, vol. 12, no. 16, p. 2754, 2022.

[19] H. Mizoguchi, T. Oga, K. Kakizaki, J. Fujimoto, and B. Fechner, "Excimer lasers for lithography and annealing," in *Handbook of Laser Micro- and Nano-Engineering*, K. Sugioka, Ed. Springer, Cham, 2021.

[20] A. Pidro, A. Biščević, M. A. Pjano, I. Mravičić, N. Bejdić, and M. Bohač, "Excimer lasers in refractive surgery," *Acta Informatica Medica*, vol. 27, no. 4, pp. 278–283, 2019.

[21] K. Sugioka, Ed., *Handbook of Laser Micro- and Nano-Engineering*. Springer, 2020.

[22] N. Ahmed, S. Darwish, and A. M. Alahmari, "Laser ablation and laser-hybrid ablation processes: a review," *Materials and Manufacturing Processes*, vol. 31, no. 9, pp. 1121–1142, 2016.

[23] M. Kneissl, A. Knorr, S. Reitzenstein, and A. Hoffmann, *Semiconductor Nanophotonics: Materials, Models, and Devices*. Springer Cham, 2020.

[24] Q. Lin, G. Wang, C. Liu, S. Sanyal, S. Mukhopadhyay, M. Dwyer, M. Seitz, T. Earles, N. Tansu, J. Zhang, L. Mawst, S. S. Pasayat, and C. Gupta, "Demonstration of watt-level 375 nm short-cavity laser diode with etched facets," *IEEE Photonics Technology Letters*, vol. 36, no. 11, pp. 741–744, 2024.

[25] X. Sun, J. Liu, X. Zhan, Y. Huang, C. Chu, Q. Xu, Y. Zhang, Z. Zhang, Q. Sun, and H. Yang, "Watt-class 368 nm UVA light-emitting diode grown on Si with a polarization-doped electron blocking layer," *Optics Express*, vol. 34, no. 4, pp. 6941–6947, 2026.

[26] R. Kirste, B. Sarkar, P. Reddy, Q. Guo, R. Collazo, and Z. Sitar, "Status of the growth and fabrication of AlGaN-based UV laser diodes for near and mid-UV wavelength," *Journal of Materials Research*, vol. 36, no. 23, pp. 4638–4656, 2021.

[27] Nichia Corporation, "NDU4116 laser diode," https://led-ld.nichia.co.jp/en/product/ndu4116, accessed: 2026-02-24, 2026.

[28] K. Sato, S. Yasue, K. Yamada, S. Tanaka, T. Omori, S. Ishizuka, S. Teramura, Y. Ogino, S. Iwayama, H. Miyake, M. Iwaya, T. Takeuchi, S. Kamiyama, and I. Akasaki, "Room-temperature operation of AlGaN ultraviolet-B laser diode at 298 nm on lattice-relaxed $Al_{0.6}Ga_{0.4}N$/AlN/sapphire," *Applied Physics Express*, vol. 13, no. 3, p. 031004, 2020.

[29] R. Miyake, T. Saito, S. Karino, Y. Sasaki, S. Maruyama, S. Kamiya, R. Watanabe, S. Kato, N. Kitta, Y. Miyamoto, R. Kobayashi, K. Kitagawa, T. Tanikawa, S. Iwayama, H. Miyake, K. Naniwae, Y. Jin, M. Toramaru, T. Matsumoto, Y. Shimazaki, H. Torii, T. Takeuchi, S. Kamiyama, and M. Iwaya, "Room-temperature continuous-wave lasing at 318 nm on a relaxed AlGaN template grown on a sapphire substrate," *Applied Physics Letters*, vol. 128, no. 2, p. 023502, 2026.

[30] H. Yu, S. Mondal, R. Shen, M. T. Hasan, D. He, J. Liu, S. Yang, M. He, O. Alkhazragi, D. Wang, M. Kira, P. Deotare, D. Liang, and Z. Mi, "Electrically pumped AlGaN edge-emitting UV-B laser diodes grown by molecular beam epitaxy," *Applied Physics Letters*, vol. 128, no. 14, p. 143501, 2026.

[31] Z. Zhang, M. Kushimoto, T. Sakai, N. Sugiyama, L. J. Schowalter, C. Sasaoka, and H. Amano, "A 271.8 nm deep-ultraviolet laser diode for room temperature operation," *Applied Physics Express*, vol. 12, no. 12, p. 124003, 2019.

[32] K. Xu and J. Huang, *Growth and Application of AlN Single Crystal*. Singapore: Springer Singapore, 2025, edition 1.

[33] J. Simon, V. Protasenko, C. Lian, H. Xing, and D. Jena, "Polarization-induced hole doping in wide-band-gap uniaxial semiconductor heterostructures," *Science*, vol. 327, no. 5961, pp. 60–64, 2010.

[34] P. Pampili and P. J. Parbrook, "Doping of III-nitride materials," *Materials Science in Semiconductor Processing*, vol. 62, pp. 180–191, 2017.

[35] C.-Z. Zhao, T. Wei, L.-Y. Chen, S.-S. Wang, and J. Wang, "The activation energy for Mg acceptor in $Al_xGa_{1-x}N$ alloys in the whole composition range," *Superlattices and Microstructures*, vol. 109, pp. 758–762, 2017.

[36] Z. Zhang, M. Kushimoto, A. Yoshikawa, K. Aoto, L. J. Schowalter, C. Sasaoka, and H. Amano, "Continuous-wave lasing of AlGaN-based ultraviolet laser diode at 274.8 nm by current injection," *Applied Physics Express*, vol. 15, no. 4, p. 041007, 2022.

[37] Z. Zhang, M. Kushimoto, A. Yoshikawa, K. Aoto, C. Sasaoka, L. J. Schowalter, and H. Amano, "Key temperature-dependent characteristics of AlGaN-based UV-C laser diode and demonstration of room-temperature continuous-wave lasing," *Applied Physics Letters*, vol. 121, no. 22, p. 222103, 2022.

[38] ULTEC Inc., "Deep UV laser diode," https://ultec.co.jp, accessed: 2026-02-22, 2026.

[39] Z.-J. Zou, B. An, Y.-K. Wang, Y. Mei, Y.-C. Wang, L.-L. Ma, L.-Y. Ying, F. Liang, J. Yang, D.-G. Zhao, and B.-P. Zhang, "GaN-based ultraviolet vertical-cavity surface-emitting lasers operating under room-temperature continuous-wave current injection," *Applied Physics Letters*, vol. 128, no. 25, p. 253501, 2026.

[40] F. Hjort, J. Enslin, M. Cobet, M. A. Bergmann, J. Gustavsson, T. Kolbe, A. Knauer, F. Nippert, I. Häusler, M. R. Wagner, T. Wernicke, M. Kneissl, and Å. Haglund, "A 310 nm optically pumped AlGaN vertical-cavity surface-emitting laser," *ACS Photonics*, vol. 8, no. 1, pp. 135–141, 2021.

[41] E. Torres, J. Ciers, N. Rebelo, F. Hjort, M. A. Bergmann, S. Graupeter, J. Enslin, G. Cardinalli, T. Wernicke, M. Kneissl, and Å. Haglund, "Ultraviolet-C vertical-cavity surface-emitting lasers with precise cavity length control," *Laser & Photonics Reviews*, vol. 19, no. 13, p. 2402203, 2025.

[42] Z. Zheng, Y. Mei, H. Long, J. Hoo, S. Guo, and Q. Li, "AlGaN-based deep-ultraviolet vertical-cavity surface-emitting laser," *IEEE Electron Device Letters*, vol. 42, no. 3, pp. 375–378, 2021.

[43] E. Torres, J. Ciers, M. A. Bergmann, J. Höpfner, S. Graupeter, M. Grigoletto, M. Guttmann, T. Kolbe, T. Wernicke, M. Kneissl, and Å. Haglund, "Ultraviolet-B resonant-cavity light-emitting diodes with tunnel junctions and dielectric mirrors," *ACS Photonics*, vol. 11, no. 8, pp. 2923–2929, 2024.

[44] T. Moudakir, F. Genty, M. Kunzer, P. Börner, T. Passow, S. Suresh, G. Patriarche, K. Köhler, W. Pletschen, J. Wagner, and A. Ougazzaden, "Design, fabrication, and characterization of near-milliwatt-power RCLEDs emitting at 390 nm," *IEEE Photonics Journal*, vol. 5, no. 6, 2013.

[45] A. Franke, M. P. Hoffmann, R. Kirste, M. Bobea, J. Tweedie, F. Kaess, M. Gerhold, R. Collazo, and Z. Sitar, "High reflectivity III-nitride UV-C distributed bragg reflectors for vertical-cavity emitting lasers," *Journal of Applied Physics*, vol. 120, no. 13, 2016.

[46] T. Akagi, Y. Kozuka, K. Ikeyama, S. Iwayama, M. Kuramoto, T. Saito, T. Tanaka, T. Takeuchi, S. Kamiyama, and M. Iwaya, "High-quality AlInN/GaN distributed bragg reflectors grown by metalorganic vapor phase epitaxy," *Applied Physics Express*, vol. 13, no. 12, 2020.

[47] C.-J. Wu, C.-Y. Kuo, C.-J. Wang, W.-E. Chang, C.-L. Tsai, C.-F. Lin, and J. Han, "Deep-UV porous AlGaN distributed bragg reflectors for deep-ultraviolet light-emitting diodes and laser diodes," *ACS Applied Nano Materials*, vol. 3, no. 1, pp. 399–402, 2020.

[48] Y. Bao, W. Lu, M. Wang, C. Liu, D.-P. Han, Z. Bi, J. Li, K. Huang, J. Kang, S. Kamiyama, and R. Zhang, "Fabrication and characterization of porous AlGaN distributed bragg reflectors with excellent thermal stability at high temperature," *ACS Applied Electronic Materials*, vol. 7, no. 10, pp. 4628–4638, 2025.

[49] Z. Zheng, Y. Wang, J. Hoo, S. Guo, Y. Mei, H. Long, L. Ying, Z. Zheng, and B. Zhang, "High-quality AlGaN epitaxial structures and realization of UV-C vertical-cavity surface-emitting lasers," *Science China Materials*, vol. 66, pp. 1978–1988, 2023.

[50] G. Cardinali, F. Hjort, N. Prokop, J. Enslin, M. Cobet, M. A. Bergmann, J. Gustavsson, J. Ciers, I. Häusler, T. Kolbe, T. Wernicke, Å. Haglund, and M. Kneissl, "Low-threshold AlGaN-based UVB VCSELs enabled by post-growth cavity detuning," *Applied Physics Letters*, vol. 121, no. 10, p. 103501, 2022.

[51] T.-C. Lu, C.-C. Kao, H.-C. Kuo, G.-S. Huang, and S.-C. Wang, "CW lasing of current-injection blue GaN-based vertical-cavity surface-emitting laser," *Applied Physics Letters*, vol. 92, no. 14, 2008.

[52] G. Cosendey, A. Castiglia, G. Rossbach, J.-F. Carlin, and N. Grandjean, "Blue monolithic AlInN-based vertical-cavity surface-emitting laser diode on free-standing GaN substrate," *Applied Physics Letters*, vol. 101, no. 15, 2012.

[53] K. Kobayashi, T. Nishikawa, R. Watanabe, T. Takeuchi, S. Kamiyama, M. Iwaya, and T. Kamei, "In situ center-wavelength control of AlInN/GaN distributed bragg reflectors with in situ reflectivity-spectra measurements," *Physica Status Solidi B*, vol. 261, no. 11, 2024.

[54] M. Sarkar, F. Adams, S. A. Dar, J. Penn, Y. Ji, A. Gundimeda, T. Zhu, C. Liu, H. Hirshy, F. C.-P. Massabuau, T. O'Hanlon, M. J. Kappers, S. Ghosh, G. Kusch, and R. A. Oliver, "Sub-surface imaging of porous GaN distributed bragg reflectors via backscattered electrons," *Microscopy and Microanalysis*, vol. 30, no. 2, pp. 208–225, 2024.

[55] J. Park, J.-H. Kang, and S.-W. Ryu, "High diffuse reflectivity of nanoporous GaN distributed bragg reflector formed by electrochemical etching," *Applied Physics Express*, vol. 6, no. 7, 2013.

[56] C. Zhang, R. ElAfandy, and J. Han, "Distributed bragg reflectors for GaN-based vertical-cavity surface-emitting lasers," *Applied Sciences*, vol. 9, no. 8, 2019.

[57] L. Persson, G. Cardinali, J. Ciers, and Å. Haglund, "Improving thermal resistance in III-nitride blue and UV vertical-cavity surface-emitting lasers," *Optics Express*, vol. 33, no. 16, pp. 34 242–34 254, 2025.

[58] S. Noda, M. Yoshida, T. Inoue, M. De Zoysa, K. Ishizaki, and R. Sakata, "Photonic-crystal surface-emitting lasers," *Nature Reviews Electrical Engineering*, vol. 1, pp. 802–814, 2024.

[59] M. Pan, C. Gautam, Y. Chen, T. Rotter, G. Balakrishnan, and W. Zhou, "Recent advances in photonic-crystal surface-emitting lasers," *IEEE Journal of Selected Topics in Quantum Electronics*, vol. 31, no. 2, 2024.

[60] H. Huang, C. Yang, H. Li, and Z. Zhang, "Unveiling the potential of photonic-crystal surface-emitting lasers: a concise review," *Semiconductor Science and Technology*, vol. 40, no. 4, 2025.

[61] W. Zhou and M. Pan, "The future of photonic-crystal surface-emitting lasers," *Applied Physics Letters*, vol. 123, no. 14, 2023.

[62] S. Noda, T. Inoue, M. Yoshida, J. Gelleta, M. De Zoysa, and K. Ishizaki, "High-power and high-beam-quality photonic-crystal surface-emitting lasers: a tutorial," *Advances in Optics and Photonics*, vol. 15, no. 4, pp. 977–1032, 2023.

[63] T.-C. Lu, S.-W. Chen, T.-T. Kao, and T.-W. Liu, "Characteristics of GaN-based photonic-crystal surface-emitting lasers," *Applied Physics Letters*, vol. 93, no. 11, 2008.

[64] H. Matsubara, S. Yoshimoto, H. Saito, Y. Jianglin, Y. Tanaka, and S. Noda, "GaN photonic-crystal surface-emitting laser at blue-violet wavelengths," *Science*, vol. 319, no. 5862, pp. 445–447, 2008.

[65] S. Kawashima, T. Kawashima, Y. Nagatomo, Y. Hori, H. Iwase, T. Uchida, K. Hoshino, A. Numata, and M. Uchida, "GaN-based surface-emitting laser with two-dimensional photonic-crystal acting as distributed-feedback grating and optical cladding," *Applied Physics Letters*, vol. 97, no. 25, 2010.

[66] D.-U. Kim, S. Kim, J. Lee, S.-R. Jeon, and H. Jeon, "Free-standing GaN-based photonic-crystal band-edge laser," *IEEE Photonics Technology Letters*, vol. 23, no. 20, pp. 1454–1456, 2011.

[67] T.-T. Wu, P.-H. Weng, Y.-J. Hou, and T.-C. Lu, "GaN-based photonic-crystal surface-emitting lasers with central defects," *Applied Physics Letters*, vol. 99, no. 22, 2011.

[68] Y.-H. Ra and C.-R. Lee, "Ultracompact display pixels: tunnel-junction nanowire photonic-crystal laser," *Nano Energy*, vol. 84, 2021.

[69] K. Emoto, T. Koizumi, M. Hirose, M. Jutori, T. Inoue, K. Ishizaki, M. De Zoysa, H. Togawa, and S. Noda, "Wide-bandgap GaN-based watt-class photonic-crystal lasers," *Communications Materials*, vol. 3, 2022.

[70] M. F. Vafadar and S. Zhao, "Ultralow threshold surface-emitting ultraviolet lasers with semiconductor nanowires," *Scientific Reports*, vol. 13, 2023.

[71] N. Taguchi, A. Iwai, M. Noguchi, H. Takahashi, A. Michiue, M. De Zoysa, T. Inoue, K. Ishizaki, and S. Noda, "Green-wavelength GaN-based photonic-crystal surface-emitting lasers," *Applied Physics Express*, vol. 17, no. 1, 2024.

[72] W.-H. Hsieh, K.-B. Hong, C.-H. Lin, C.-Y. Yang, T.-C. Lu, and C.-Y. Huang, "Impact of air-hole geometry on the performance of InGaN/GaN photonic-crystal surface-emitting lasers," *IEEE Journal of Selected Topics in Quantum Electronics*, vol. 32, no. 6: Special Issue on Advances in VCSELs and PCSELs, pp. 1–6, 2026.

[73] T. Xu, M. Feng, X. Sun, R. Xi, X. Li, S. Zhang, Q. Sun, X. Yu, K. Xiong, and H. Yang, "Room-temperature electrically injected GaN-based photonic-crystal surface-emitting lasers," *Journal of Semiconductors*, vol. 46, no. 9, 2025.

[74] T.-Y. Ku, C.-H. Wang, M.-C. Hsieh, and G. Lin, "AlGaInP-based visible-red photonic-crystal surface-emitting lasers without regrowth," *IEEE Journal of Quantum Electronics*, vol. 59, no. 6, 2023.

[75] Z. Sun, B. Zhou, Y. Zheng, Y. Miao, X. Yu, T. Xu, J. Wang, M. Ling, X. Wang, S. Xia, Z. Liu, Z. Li, P. Wen, W. Liu, K. Xiong, J. Liu, H. Wang, and H. Yang, "Regrowth-free blue GaN-based photonic crystal surface-emitting lasers with triangular air holes," *Applied Physics Letters*, vol. 128, no. 24, p. 243310, 2026.

[76] T. Xu, M. Feng, R. Xi, X. Yu, J. Wang, K. Xiong, P. Chen, X. Zhang, Z. Guo, X. Li, S. Zhang, Q. Sun, J. Liu, Z. Liu, Z. Li, and H. Yang, "3.2 w GaN-based photonic-crystal surface-emitting laser," *Laser & Photonics Reviews*, vol. n/a, no. n/a, p. e71621.

[77] H.-Y. Lu, S.-C. Tian, C.-Z. Tong, L.-J. Wang, J.-M. Rong, C.-Y. Liu, H. Wang, S.-L. Shu, and L.-J. Wang, "Extracting more light for vertical emission: high power continuous wave operation of 1.3-μm quantum-dot photonic-crystal surface-emitting laser based on a flat band," *Light: Science & Applications*, vol. 8, 2019.

[78] C.-J. Chang, L.-R. Chen, Y.-J. Wu, C.-C. Tseng, K.-B. Hong, and H.-C. Kuo, "High power short-wavelength infrared photonic-crystal surface-emitting lasers," *Journal of Lightwave Technology*, vol. 42, no. 15, pp. 5262–5268, 2024.

[79] Z. Wang, X. Liu, P. Wang, H. Lu, B. Meng, W. Zhang, L. Wang, Y. Wang, and C. Tong, "Continuous-wave operation of 1550 nm low-threshold triple-lattice photonic-crystal surface-emitting lasers," *Light: Science & Applications*, vol. 13, 2024.

[80] Z.-L. Li, Y.-C. Kang, G. Lin, and C.-P. Lee, "Mid-infrared photonic-crystal surface-emitting lasers with InGaAs/GaAsSb 'w'-type quantum wells grown on InP substrate," *Photonics*, vol. 5, no. 4, p. 32, 2018.

[81] L. Shterengas, G. Kipshidze, A. Stein, W. J. Lee, R. Liu, and G. Belenky, "Photonic crystal surface-emitting GaSb-based type-i quantum-well diode lasers," *IEEE Journal of Selected Topics in Quantum Electronics*, vol. 31, p. 1500807, 2024.

[82] P. Wang, Z. Wang, Y. Yu, X. Liu, H. Lu, B. Meng, L. Wang, Y. Wang, and C. Tong, "Room temperature CW operation of 1.3 μm quantum dot triple-lattice photonic crystal surface-emitting lasers with buried structure," *Optics Express*, vol. 33, no. 13, pp. 27 429–27 437, 2025.

[83] Z. Liao, Y. Wang, Y. Ma, Y. Dai, H. Ji, Y. Chen, J. Chen, Y. Lin, and W. Zheng, "Quantum cascade photonic crystal surface-emitting laser with lateral coupling cavity at 9.4 μm," *IEEE Photonics Technology Letters*, vol. 38, no. 4, pp. 247–250, 2026.

[84] B. H. Le, X. Liu, N. H. Tran, S. Zhao, and Z. Mi, "An electrically injected AlGaN nanowire defect-free photonic crystal ultraviolet laser," *Optics Express*, vol. 27, no. 4, pp. 5843–5850, 2019.

[85] Q. Xia, H. Xia, and A. L. Ruoff, "Pressure-induced rocksalt phase of aluminum nitride: a metastable structure at ambient condition," *Journal of Applied Physics*, vol. 73, no. 12, pp. 8198–8200, 1993.

[86] P. Perlin, C. Jauberthie-Carillon, J. P. Itie, A. San Miguel, I. Grzegory, and A. Polian, "Raman scattering and x-ray absorption spectroscopy in gallium nitride under high pressure," *Physical Review B*, vol. 45, pp. 83–89, 1992.

[87] M. Ueno, M. Yoshida, A. Onodera, O. Shimomura, and K. Takemura, "Stability of the wurtzite-type structure under high pressure: GaN and InN," *Physical Review B*, vol. 49, pp. 14–21, 1994.

[88] F. Bernardini, V. Fiorentini, and D. Vanderbilt, "Spontaneous polarization and piezoelectric constants of III-V nitrides," *Physical Review B*, vol. 56, pp. R10 024–R10 027, 1997.

[89] I. Vurgaftman and J. R. Meyer, "Band parameters for nitrogen-containing semiconductors," *Journal of Applied Physics*, vol. 94, no. 6, pp. 3675–3696, 2003.

[90] Q. Yan, P. Rinke, A. Janotti, M. Scheffler, and C. G. Van de Walle, "Effects of strain on the band structure of group-iii nitrides," *Physical Review B*, vol. 90, p. 125118, 2014.

[91] C. Kisielowski, J. Krüger, S. Ruvimov, T. Suski, J. W. Ager, E. Jones, Z. Liliental-Weber, M. Rubin, E. R. Weber, M. D. Bremser, and R. F. Davis, "Strain-related phenomena in GaN thin films," *Physical Review B*, vol. 54, pp. 17 745–17 753, 1996.

[92] P. Perlin, L. Mattos, N. A. Shapiro, J. Kruger, W. S. Wong, T. Sands, N. W. Cheung, and E. R. Weber, "Reduction of the energy gap pressure coefficient of GaN due to the constraining presence of the sapphire substrate," *Journal of Applied Physics*, vol. 85, no. 4, pp. 2385–2389, 1999.

[93] D. Brunner, H. Angerer, E. Bustarret, F. Freudenberg, R. Höpler, R. Dimitrov, O. Ambacher, and M. Stutzmann, "Optical constants of epitaxial AlGaN films and their temperature dependence," *Journal of Applied Physics*, vol. 82, no. 10, pp. 5090–5096, 1997.

[94] N. Nepal, J. Li, M. L. Nakarmi, J. Y. Lin, and H. X. Jiang, "Temperature and compositional dependence of the energy band gap of AlGaN alloys," *Applied Physics Letters*, vol. 87, no. 24, p. 242104, 2005.

[95] C. Reich, M. Guttmann, M. Feneberg, T. Wernicke, F. Mehnke, C. Kuhn, J. Rass, M. Lapeyrade, S. Einfeldt, A. Knauer, V. Kueller, M. Weyers, R. Goldhahn, and M. Kneissl, "Strongly transverse-electric-polarized emission from deep ultraviolet AlGaN quantum well light emitting diodes," *Applied Physics Letters*, vol. 107, no. 14, p. 142101, 2015.

[96] S. L. Chuang and C. S. Chang, "k·p method for strained wurtzite semiconductors," *Physical Review B*, vol. 54, pp. 2491–2504, 1996.

[97] I. Vurgaftman, J. R. Meyer, and L. R. Ram-Mohan, "Band parameters for III–V compound semiconductors and their alloys," *Journal of Applied Physics*, vol. 89, no. 11, pp. 5815–5875, 2001.

[98] L. Coldren, S. Corzine, and M. Mashanovitch, *Diode Lasers and Photonic Integrated Circuits*. John Wiley & Sons, Ltd, 2012.

[99] M. Leroux, N. Grandjean, M. Laügt, J. Massies, B. Gil, P. Lefebvre, and P. Bigenwald, "Quantum confined stark effect due to built-in internal polarization fields in (Al,Ga)N/GaN quantum wells," *Physical Review B*, vol. 58, pp. R13 371–R13 374, 1998.

[100] R. Langer, J. Simon, V. Ortiz, N. T. Pelekanos, A. Barski, R. André, and M. Godlewski, "Giant electric fields in unstrained GaN single quantum wells," *Applied Physics Letters*, vol. 74, no. 25, pp. 3827–3829, 1999.

[101] T. Takeuchi, S. Sota, M. Katsuragawa, M. Komori, H. Takeuchi, H. Amano, and I. Akasaki, "Quantum-confined stark effect due to piezoelectric fields in GaInN strained quantum wells," *Japanese Journal of Applied Physics*, vol. 36, no. 4B, pp. L382–L385, 1997.

[102] A. Kafar, S. Stanczyk, S. Grzanka, K. Pieniak, T. Suski, and P. Perlin, "Screening of quantum-confined stark effect in nitride laser diodes and superluminescent diodes," *Applied Physics Express*, vol. 12, no. 4, p. 044001, 2019.

[103] T. Deguchi, A. Shikanai, K. Torii, T. Sota, S. Chichibu, and S. Nakamura, "Luminescence spectra from InGaN multiquantum wells heavily doped with Si," *Applied Physics Letters*, vol. 72, no. 25, pp. 3329–3331, 1998.

[104] S.-H. Park and S.-L. Chuang, "Spontaneous polarization effects in wurtzite GaN/AlGaN quantum wells and comparison with experiment," *Applied Physics Letters*, vol. 76, no. 15, pp. 1981–1983, 2000.

[105] G. Cardinali, S. Kölle, A. Schulz, N. Susilo, D. Hauer Vidal, M. Guttmann, M. A. Blonski, F. Römer, B. Witzigmann, F. Nippert, M. R. Wagner, T. Wernicke, and M. Kneissl, "Gain characteristics of optically pumped UVC lasers with wide AlGaN single-quantum-well active regions," *physica status solidi (a)*, vol. 221, no. 21, p. 2400067, 2024.

[106] M. Hajdel, M. Chlipała, M. Siekacz, H. Turski, P. Wolny, K. Nowakowski-Szkudlarek, A. Feduniewicz-Żmuda, C. Skierbiszewski, and G. Muziol, "Dependence of InGaN quantum well thickness on the nature of optical transitions in LEDs," *Materials*, vol. 15, no. 1, 2022.

[107] S.-H. Park, "Crystal orientation effects on electronic properties of wurtzite InGaN/GaN quantum wells," *Journal of Applied Physics*, vol. 91, no. 12, pp. 9904–9908, 2002.

[108] M. Monavarian, A. Rashidi, and D. Feezell, "A decade of nonpolar and semipolar III-nitrides: a review of successes and challenges," *physica status solidi (a)*, vol. 216, no. 1, p. 1800628, 2019.

[109] T. Zhu and R. A. Oliver, "Unintentional doping in GaN," *Physical Chemistry Chemical Physics*, vol. 14, pp. 9558–9573, 2012.

[110] M. A. Zambrano-Serrano, C. A. Hernández, O. de Melo, M. Behar, S. Gallardo-Hernández, Y. L. Casallas-Moreno, A. Ponce, A. Hernandez-Robles, D. Bahena-Uribe, C. M. Yee-Rendón, and M. López-López, "Effects of heavy Si doping on the structural and optical properties of n-GaN/AlN/Si(111) heterostructures," *Materials Research Express*, vol. 9, no. 6, p. 065903, 2022.

[111] L. T. Romano, C. G. Van de Walle, I. Ager, J. W., W. Götz, and R. S. Kern, "Effect of Si doping on strain, cracking, and microstructure in GaN thin films grown by metalorganic chemical vapor deposition," *Journal of Applied Physics*, vol. 87, no. 11, pp. 7745–7752, 2000.

[112] S. Huang, M. Ikeda, F. Zhang, M. Zhang, J. Zhu, S. Zhang, and J. Liu, "Achievable hole concentration at room temperature as a function of Mg concentration for MOCVD-grown p-GaN after sufficient annealing," *Journal of Semiconductors*, vol. 45, no. 8, p. 082501, 2024.

[113] K. B. Nam, M. L. Nakarmi, J. Li, J. Y. Lin, and H. X. Jiang, "Mg acceptor level in AlN probed by deep ultraviolet photoluminescence," *Applied Physics Letters*, vol. 83, no. 5, pp. 878–880, 2003.

[114] M. Grigoletto, J. Höpfner, M. Schilling, T. Ehlermann, L. Zeiler, P. Sonka, L. Sulmoni, T. Wernicke, and M. Kneissl, "Low resistance

distributed polarization doped p-AlGaN layer for 265 nm LEDs operating at very high current densities," *Semiconductor Science and Technology*, vol. 41, no. 2, p. 025019, 2026.

[115] J. Wang, F. Xu, L. Zhang, J. Lang, X. Fang, Z. Zhang, X. Guo, C. Ji, C. Ji, F. Tan, X. Yang, X. Kang, Z. Qin, N. Tang, X. Wang, W. Ge, and B. Shen, "Progress in efficient doping of Al-rich AlGaN," *Journal of Semiconductors*, vol. 45, no. 2, p. 021501, 2024.

[116] K. Nagata, H. Makino, T. Yamamoto, K. Kataoka, T. Narita, and Y. Saito, "Low resistivity of highly Si-doped n-type $al_{0.62}ga_{0.38}n$ layer by suppressing self-compensation," *Applied Physics Express*, vol. 13, no. 2, p. 025504, 2020.

[117] W. Walukiewicz, R. Jones, S. Li, K. Yu, J. Ager, E. Haller, H. Lu, and W. Schaff, "Dopants and defects in InN and InGaN alloys," *Journal of Crystal Growth*, vol. 288, no. 2, pp. 278–282, 2006.

[118] W. Walukiewicz, "Intrinsic limitations to the doping of wide-gap semiconductors," *Physica B: Condensed Matter*, vol. 302-303, pp. 123–134, 2001.

[119] R. E. Jones, K. M. Yu, S. X. Li, W. Walukiewicz, J. W. Ager, E. E. Haller, H. Lu, and W. J. Schaff, "Evidence for p-type doping of InN," *Physical Review Letters*, vol. 96, p. 125505, 2006.

[120] M. Meier, A. Mekis, A. Dodabalapur, A. Timko, R. E. Slusher, J. D. Joannopoulos, and O. Nalamasu, "Laser action from two-dimensional distributed feedback in photonic crystals," *Applied Physics Letters*, vol. 74, no. 1, pp. 7–9, 1999.

[121] M. Imada, S. Noda, A. Chutinan, T. Tokuda, M. Murata, and G. Sasaki, "Coherent two-dimensional lasing action in surface-emitting laser with triangular-lattice photonic crystal structure," *Applied Physics Letters*, vol. 75, no. 3, pp. 316–318, 1999.

[122] K. Hirose, Y. Liang, Y. Kurosaka, A. Watanabe, T. Sugiyama, and S. Noda, "Watt-class high-power, high-beam-quality photonic-crystal lasers," *Nature Photonics*, vol. 8, p. 406–411, 2014.

[123] K. Koshelev, S. Lepeshov, M. Liu, A. Bogdanov, and Y. Kivshar, "Asymmetric metasurfaces with high-Q resonances governed by bound states in the continuum," *Physical Review Letters*, vol. 121, p. 193903, 2018.

[124] T.-T. Wu, C.-C. Chen, and T.-C. Lu, "Effects of lattice types on GaN-based photonic crystal surface-emitting lasers," *IEEE Journal of Selected Topics in Quantum Electronics*, vol. 21, no. 1, pp. 426–431, 2015.

[125] Z. Wang, P. Wang, H. Lu, B. Meng, Y. Wang, C. Tong, and L. Wang, "Symmetry criterion and far-field control of photonic-crystal surface-emitting lasers," *Applied Sciences*, vol. 12, no. 20, 2022.

[126] Q. Liu, M. Meng, S. Ma, and M. Feng, "Design of double-lattice GaN-PCSEL based on triangular and circular holes," *Optics Express*, vol. 31, no. 26, pp. 43 615–43 629, 2023.

[127] B. King, H. Wenzel, E. Kuhn, M. Radziunas, and P. Crump, "Design of very-large area photonic crystal surface emitting lasers with an all-semiconductor photonic crystal," *Optics Express*, vol. 32, no. 25, pp. 44 945–44 957, 2024.

[128] M. Yoshida, M. De Zoysa, K. Ishizaki, Y. Tanaka, M. Kawasaki, R. Hatsuda, B. Song, J. Gelleta, and S. Noda, "Double-lattice photonic-crystal resonators enabling high-brightness semiconductor lasers with symmetric narrow-divergence beams," *Nature Materials*, vol. 18, p. pages121–128, 2019.

[129] R. Contractor, W. Noh, W. Redjem, W. Qarony, E. Martin, S. Dhuey, A. Schwartzberg, and B. Kanté, "Scalable single-mode surface-emitting laser via open-dirac singularities," *Nature*, vol. 608, pp. 692–697, 2022.

[130] R. J. E. Taylor, D. T. D. Childs, P. Ivanov, B. J. Stevens, N. Babazadeh, A. J. Crombie, G. Ternent, S. Thoms, H. Zhou, and R. A. Hogg, "Electronic control of coherence in a two-dimensional array of photonic crystal surface emitting lasers," *Scientific Reports*, vol. 5, p. 13203, 2015.

[131] C.-J. Chang, L.-R. Chen, K.-B. Hong, W.-C. Weng, B.-H. Chuang, H.-C. Kuo, and T.-C. Lu, "A simple nethod to build high power PCSEL array with isolation pattern design," *Crystals*, vol. 12, no. 10, 2022.

[132] B. C. King, K. J. Rae, A. F. McKenzie, A. Boldin, D. Kim, N. D. Gerrard, G. Li, K. Nishi, K. Takemasa, M. Sugawara, R. J. E.

Taylor, D. T. D. Childs, and R. A. Hogg, "Coherent power scaling in photonic crystal surface emitting laser arrays," *AIP Advances*, vol. 11, no. 1, p. 015017, 2021.

[133] S. Katsuno, M. Yoshida, T. Inoue, M. De Zoysa, R. Hatsuda, K. Ishizaki, and S. Noda, "Design and experimental demonstration of photonic-crystal lasers with multijunction active layers," *Applied Physics Express*, vol. 17, no. 12, p. 122004, 2024.

[134] Y. Kurosaka, S. Iwahashi, Y. Liang, K. Sakai, E. Miyai, W. Kunishi, D. Ohnishi, and S. Noda, "On-chip beam-steering photonic-crystal lasers," *Nature Photonics*, vol. 4, pp. 447–450, 2010.

[135] Y. Kurosaka, K. Hirose, T. Sugiyama, Y. Takiguchi, and Y. Nomoto, "Phase-modulating lasers toward on-chip integration," *Scientific Reports*, vol. 6, 2016.

[136] K. Hirose, Y. Takiguchi, T. Sugiyama, Y. Nomoto, S. Uenoyama, and Y. Kurosaka, "Removal of surface-normal spot beam from on-chip 2D beam pattern projecting lasers," *Optics Express*, vol. 26, no. 23, pp. 29 854–29 866, 2018.

[137] R. Morita, T. Inoue, M. Yoshida, K. Enoki, M. D. Zoysa, K. Ishizaki, and S. Noda, "Demonstration of high-power photonic-crystal surface-emitting lasers with 1-kHz-class intrinsic linewidths," *Optica*, vol. 11, no. 3, pp. 333–339, 2024.

[138] T. Inoue, M. Yoshida, J. Gelleta, K. Izumi, K. Yoshida, K. Ishizaki, M. De Zoysa, and S. Noda, "General recipe to realize photonic-crystal surface-emitting lasers with 100-W-to-1-kW single-mode operation," *Nature Communications*, vol. 13, p. 3274, 2022.

[139] M. Yoshida, S. Katsuno, T. Inoue, J. Gelleta, K. Izumi, M. De Zoysa, K. Ishizaki, and S. Noda, "High-brightness scalable continuous-wave single-mode photonic-crystal laser," *Nature*, vol. 618, pp. 727–732, 2023.

[140] T. G. Mackay and A. Lakhtakia, *The transfer-matrix method in electromagnetics and optics.* Springer Cham, 2020, edition 1.

[141] J. D. Joannopoulos, S. G. Johnson, J. N. Winn, and R. D. Meade, *Photonic Crystals: Molding the Flow of Light*, 2nd ed. Princeton, NJ: Princeton University Press, 2008.

[142] E. Yablonovitch, "Inhibited spontaneous emission in solid-state physics and electronics," *Physical Review Letters*, vol. 58, pp. 2059–2062, 1987.

[143] S. G. Johnson and J. D. Joannopoulos, "Block-iterative frequency-domain methods for Maxwell's equations in a planewave basis," *Optics Express*, vol. 8, no. 3, pp. 173–190, 2001.

[144] M. Imada, A. Chutinan, S. Noda, and M. Mochizuki, "Multidirectionally distributed feedback photonic crystal lasers," *Physical Review B*, vol. 65, p. 195306, 2002.

[145] L. Nevou, "Light Photonic Crystal 2D," https://github.com/LaurentNevou/Light_PhotonicCrystal_2D, accessed: 2026-05-24, 2026.

[146] *COMSOL Multiphysics® v. 6.2*, COMSOL AB, Stockholm, Sweden, 2026.

[147] Y. Liang, C. Peng, K. Ishizaki, S. Iwahashi, K. Sakai, Y. Tanaka, K. Kitamura, and S. Noda, "Three-dimensional coupled-wave analysis for triangular-lattice photonic-crystal surface-emitting lasers with transverse-electric polarization," *Optics Express*, vol. 21, no. 1, pp. 565–580, 2013.

[148] L. Persson, M. Riedel, Å. Haglund, and U. T. Schwarz, "Finite-size effects in photonic-crystal surface-emitting lasers: critical discussion of different approximations," *Optics Express*, vol. 33, no. 25, pp. 53 098–53 116, 2025.

[149] Q. Zhang, M. Lü, J. Hu, Q. Dai, R. Zhu, X. Xu, and C. Zhang, "Size scaling law for radiation losses of modes in photonic crystal surface emitting devices," *Optics Express*, vol. 34, no. 12, pp. 22 773–22 784, 2026.

[150] Y. Liang, C. Peng, K. Sakai, S. Iwahashi, and S. Noda, "Three-dimensional coupled-wave analysis for square-lattice photonic crystal surface emitting lasers with transverse-electric polarization: finite-size effects," *Optics Express*, vol. 20, no. 14, pp. 15 945–15 961, 2012.

[151] W. Streifer, D. Scifres, and R. Burnham, "Coupled wave analysis of DFB and DBR lasers," *IEEE Journal of Quantum Electronics*, vol. 13, no. 4, pp. 134–141, 1977.

[152] G. Heliotis, R. Xia, D. D. C. Bradley, G. A. Turnbull, I. D. W. Samuel, P. Andrew, and W. L. Barnes, "Two-dimensional distributed feedback lasers using a broadband, red polyfluorene gain medium," *Journal of Applied Physics*, vol. 96, no. 12, pp. 6959–6965, 2004.

[153] D. Apaydın, H. Andersson, L. Uhlig, S. Graupeter, J. Ciers, G. Cardinali, E. Strandberg, T. Wernicke, M. Kneissl, U. T. Schwarz, P. Tassin, and Å. Haglund, "Deep-UV photonic-crystal surface-emitting lasers," *Laser & Photonics Reviews*, vol. 20, no. 6, p. e00271, 2026.

[154] H. Kogelnik and C. V. Shank, "Coupled-Wave theory of distributed feedback lasers," *Journal of Applied Physics*, vol. 43, no. 5, pp. 2327–2335, 1972.

[155] K. Sakai, J. Yue, and S. Noda, "Coupled-wave model for triangular-lattice photonic crystal with transverse electric polarization," *Optics Express*, vol. 16, no. 9, pp. 6033–6040, 2008.

[156] S. Izumi, M. Minami, M. Kamada, T. Tatsumi, A. A. Yamaguchi, K. Ishikawa, M. Hori, and S. Tomiya, "Photoluminescence study of plasma-induced damage of GaInN single quantum well," *Japanese Journal of Applied Physics*, vol. 52, no. 8S, p. 08JL09, 2013.

[157] M. Minami, S. Tomiya, K. Ishikawa, R. Matsumoto, S. Chen, M. Fukasawa, F. Uesawa, M. Sekine, M. Hori, and T. Tatsumi, "Analysis of GaN damage induced by $Cl_2/SiCl_4/Ar$ plasma," *Japanese Journal of Applied Physics*, vol. 50, no. 8S1, p. 08JE03, 2011.

[158] J. G. Nedy, N. G. Young, K. M. Kelchner, Y. Hu, R. M. Farrell, S. Nakamura, S. P. DenBaars, C. Weisbuch, and J. S. Speck, "Low damage dry etch for III-nitride light emitters," *Semiconductor Science and Technology*, vol. 30, no. 8, p. 085019, 2015.

[159] S. Hagedorn, S. Walde, A. Knauer, N. Susilo, D. Pacak, L. Cancellara, C. Netzel, A. Mogilatenko, C. Hartmann, T. Wernicke, M. Kneissl, and M. Weyers, "Status and prospects of AlN templates on sapphire for ultraviolet light-emitting diodes," *physica status solidi (a)*, vol. 217, no. 14, p. 1901022, 2020.

[160] H. Miyake, C.-H. Lin, K. Tokoro, and K. Hiramatsu, "Preparation of high-quality AlN on sapphire by high-temperature face-to-face annealing," *Journal of Crystal Growth*, vol. 456, pp. 155–159, 2016, proceeding of the 9th International Workshop on Bulk Nitride Semiconductors.

[161] Y. K. Siew, G. Sarkar, X. Hu, J. Hui, A. See, and C. T. Chua, "Thermal curing of hydrogen silsesquioxane," *Journal of The Electrochemical Society*, vol. 147, no. 1, p. 335, 2000.

[162] A. E. Grigorescu and C. W. Hagen, "Resists for sub-20-nm electron beam lithography with a focus on HSQ: state of the art," *Nanotechnology*, vol. 20, no. 29, p. 292001, 2009.

[163] J. K. W. Yang and K. K. Berggren, "Using high-contrast salty development of hydrogen silsesquioxane for sub-10-nm half-pitch lithography," *Journal of Vacuum Science & Technology B: Microelectronics and Nanometer Structures Processing, Measurement, and Phenomena*, vol. 25, no. 6, pp. 2025–2029, 2007.

[164] Z.-L. Li, S.-C. Lin, G. Lin, H.-W. Cheng, K.-W. Sun, and C.-P. Lee, "Effect of etching depth on threshold characteristics of GaSb-based middle infrared photonic-crystal surface-emitting lasers," *Micromachines*, vol. 10, no. 3, 2019.

[165] L. Jaloustre, V. Ackermann, S. Sales De Mello, S. Labau, C. Petit-Etienne, and E. Pargon, "Preferential crystal orientation etching of GaN nanopillars in Cl_2 plasma," *Materials Science in Semiconductor Processing*, vol. 165, p. 107654, 2023.

[166] M. Riedel, L. Persson, D. Apaydın, Å. Haglund, and U. T. Schwarz, "Modeling photonic-crystal surface-emitting lasers with guided mode expansion: Finite-size effects and higher order modes," *Optica Open Preprint*, 2026, available at https://preprints.opticaopen.org/s/b151b7c1c5e88a0a9b10.

[167] K. McGroddy, A. David, E. Matioli, M. Iza, S. Nakamura, S. DenBaars, J. S. Speck, C. Weisbuch, and E. L. Hu, "Directional emission control and increased light extraction in GaN photonic crystal light emitting diodes," *Applied Physics Letters*, vol. 93, no. 10, p. 103502, 2008.

[168] S. Iwahashi, Y. Kurosaka, K. Sakai, K. Kitamura, N. Takayama, and S. Noda, "Higher-order vector beams produced by photonic-crystal lasers," *Optics Express*, vol. 19, no. 13, pp. 11 963–11 968, 2011.

[169] E. Miyai, K. Sakai, T. Okano, W. Kunishi, D. Ohnishi, and S. Noda, "Lasers producing tailored beams," *Nature*, vol. 441, p. 946, 2006.

[170] L. Wang, C. Lu, J. Lu, L. Liu, N. Liu, Y. Chen, Y. Zhang, E. Gu, and X. Hu, "Influence of carrier screening and band filling effects on efficiency droop of InGaN light emitting diodes," *Optics Express*, vol. 19, no. 15, pp. 14 182–14 187, 2011.

[171] B. Lang, P. D. Sewell, A. Vukovic, K. Boylan, S. Rihani, D. Moodie, R. Spalding, N. Hattasan, and G. Berry, "Mode switching in photonic crystal surface emitting lasers with back reflectors and holes of varying depths," *Optics Express*, vol. 33, no. 17, pp. 35 257–35 269, 2025.

[172] Y. Kurosaka, K. Hirose, A. Watanabe, T. Sugiyama, Y. Liang, and S. Noda, "Effects of non-lasing band in two-dimensional photonic-crystal lasers clarified using omnidirectional band structure," *Optics Express*, vol. 20, no. 19, pp. 21 773–21 783, 2012.

[173] J. Grandusky, J. Smart, M. Mendrick, L. Schowalter, K. Chen, and E. Schubert, "Pseudomorphic growth of thick n-type $Al_xGa_{1-x}N$ layers on low-defect-density bulk aln substrates for UV LED applications," *Journal of Crystal Growth*, vol. 311, no. 10, pp. 2864–2866, 2009.

[174] A. Allerman, M. Crawford, S. Lee, and B. Clark, "Low dislocation density AlGaN epilayers by epitaxial overgrowth of patterned templates," *Journal of Crystal Growth*, vol. 388, pp. 76–82, 2014.

[175] S. M. Singh, V. Z. Zubialevich, and P. J. Parbrook, "Surface morphology evolution of AlGaN microhoneycomb structures during epitaxial overgrowth," *physica status solidi (b)*, vol. 261, no. 3, p. 2300471, 2024.

[176] Y. Itoh, T. Aoki, K. Fujii, H. Yoshinaga, N. Fujiwara, K. Takada, M. Ogasawara, Y. Sawada, H. Yagi, M. Yanagisawa, M. Yoshida,

T. Inoue, M. D. Zoysa, K. Ishizaki, and S. Noda, "High-power and high-efficiency operation of 1.3 µm-wavelength InP-based photonic-crystal surface-emitting lasers with metal reflector," *Optics Express*, vol. 32, no. 7, pp. 12 520–12 527, 2024.

[177] K. Kawasaki, C. Koike, Y. Aoyagi, and M. Takeuchi, "Vertical AlGaN deep ultraviolet light emitting diode emitting at 322nm fabricated by the laser lift-off technique," *Applied Physics Letters*, vol. 89, no. 26, p. 261114, 2006.

[178] K. Shojiki, M. Shimokawa, S. Iwayama, T. Omori, S. Teramura, A. Yamaguchi, M. Iwaya, T. Takeuchi, S. Kamiyama, and H. Miyake, "Centimeter-scale laser lift-off of an AlGaN UVB laser diode structure grown on nano-patterned AlN," *Applied Physics Express*, vol. 15, no. 5, p. 051004, 2022.

[179] E. Matsubara, R. Hasegawa, T. Nishibayashi, A. Yabutani, R. Yamada, Y. Imoto, R. Kondo, S. Iwayama, T. Takeuchi, S. Kamiyama, K. Shojiki, S. Kumagai, H. Miyake, and M. Iwaya, "A method for exfoliating AlGaN films from sapphire substrates using heated and pressurized water," *Applied Physics Express*, vol. 15, no. 11, p. 116502, 2022.

[180] T. Nishibayashi, R. Kondo, E. Matsubara, R. Yamada, R. Miyake, Y. Sasaki, Y. Imoto, S. Iwayama, T. Takeuchi, S. Kamiyama, H. Miyake, and M. Iwaya, "Fabrication of vertical algan-based ultraviolet-B laser diodes using a substrate exfoliation method with water," *physica status solidi (RRL) – Rapid Research Letters*, vol. 18, no. 11, p. 2300460, 2024.

[181] M. A. Bergmann, J. Enslin, M. Guttmann, L. Sulmoni, N. L. Ploch, F. Hjort, T. Kolbe, T. Wernicke, M. Kneissl, and Å. Haglund, "Increased light extraction of thin-film flip-chip UVB LEDs by surface texturing," *ACS Photonics*, vol. 10, no. 2, pp. 368–373, 2023.

[182] Y. Nishikawa, K. Ueno, A. Kobayashi, and H. Fujioka, "Preparation of degenerate n-type $Al_xGa_{1-x}N$ ($0 < x \leq 0.81$) with record low resistivity by pulsed sputtering deposition," *Applied Physics Letters*, vol. 122, no. 23, p. 232102, 2023.

[183] C. Gautam, M. Pan, S. Seth, T. J. Rotter, M. Zhou, B. J. Thompson, R. Gibson, S. Fan, G. Balakrishnan, and W. Zhou, "Mode

distribution impact on photonic crystal surface emitting laser performance," *APL Photonics*, vol. 9, no. 7, p. 076113, 2024.